学 位 論 文

Measurement of the Proton Structure Function F_2 at HERA

(HERA における陽子構造関数 F_2 の測定)

平成 5 年 12 月博士 (理学) 申請

東京大学大学院理学系研究科
物理学専攻

中尾　幹彦

Measurement of the Proton Structure Function F_2 at HERA

Mikihiko Nakao

Graduate School
University of Tokyo
7-3-1, Hongo, Bunkyo-ku, Tokyo 133 Japan

Contents

Abstract

New results of the proton structure function F_2 are obtained from $543\,\mathrm{nb}^{-1}$ of data collected with ZEUS at HERA. The measurement extends over a wide kinematic region from $8.5\,\mathrm{GeV}^2$ to $6280\,\mathrm{GeV}^2$ in Q^2 and from 2.3×10^{-4} to 0.24 in x. The results consistently improves the previous F_2 results by ZEUS[1] and H1[2], with the smaller errors, the finer binning and the extension of the kinematic range. In the small x region, F_2 increases steeply along with the decrease of x. However, F_2 shows slightly faster Q^2-evolution than available predictions at small x. The increase of F_2 at small x is compatible with the gluon distribution parametrized as $xg(x) \sim x^{-\lambda}$ with a value of λ between 0.3 and 0.5.

Contents

Chapter 1

Introduction

The *proton* is one of the basic building blocks of matter. The nucleus of the atom consists of the protons and neutrons, that carry almost entire mass of the atom, and the number of protons in the nucleus, which is called atomic number, determines the type of element. Measurement of the form factor shows that the proton is not point-like and that the size of the proton is about 10^{-15} m. The anomalous magnetic moment of the proton also indicates that the proton has an internal structure. Characteristics of the proton are originated in the internal structure of the proton, which therefore has to be revealed for understanding of matter.[3–5]

In general, inside of a very tiny "target" is studied by a scattering experiment, like the famous example of the Ratherford's experiment. In the case of the proton, the best probe to explore the structure has been the structureless leptons: electron, muon and neutrino. Up to now, surprisingly lots of characteristics of the proton have been discovered by measuring only the energy and angle distribution of the scattered lepton. The information on the final state of the target is not necessary, since the inelastic lepton-proton scattering process is described by two variables.

Usually, Lorenz invariant variables are constructed from the energy and angle for the description of scattering. A convenient choice is to use the absolute value of the 4-momentum transfer squared Q^2 and the momentum fraction x of the proton that contributed to scattering. The charged lepton-proton scattering process is predominantly a one-photon exchange process, and the true probe that "sees" the proton is the exchanged photon. The "transverse scale" of the exchanged photon is determined by $1/\sqrt{Q^2}$ because of the uncertainty principle. Since Q^2 is limited by the center-of-mass energy squared, a finer structure of the proton can be studied at higher energy. The differential cross section reflects not only the proton structure but

also the properties of the interaction process, and therefore the structure dependent factors are separated from such factors conventionally as the so-called structure functions. Kinematics of the lepton-proton scattering process and the structure functions are formalized in Chapter 2.

Historically, the proton structure has been explored by precision fixed-target experiments that inject lepton beams into stationary proton targets. When Q^2 is small ($\lesssim 0.01$ GeV^2), the exchanged photon cannot resolve the structure of the proton and is absorbed by the whole proton ($x = 1$), or in other words, the lepton is scattered elastically. The cross section of the elastic scattering process is still affected by the spatial extent of the proton, which is usually written down in terms of the scale (Q^2) dependent form factors. As Q^2 becomes larger, the lepton starts to excite the proton into resonance states such as Δ and then it is scattered inelastically. If Q^2 becomes much larger ($\gtrsim 1$ GeV^2), the *deep inelastic scattering* (DIS) process, in which the proton cannot hold the structure and breaks up into hadrons as shown in Fig. 1.1-(b), becomes dominant. The exchanged photon is interacting only with a fraction of the proton ($x < 1$) and the cross section is described in terms of the structure functions that depends on both x and Q^2.

In late 1960's, the electron-proton inelastic scattering experiments were carried out extensively at SLAC. They found that the structure function does not depend on Q^2 at large-Q^2[6]. This scaling behavior implies that there are free point-like spin-$\frac{1}{2}$ particles (partons) inside the proton as shown in Fig. 1.1-(c)[7]. This parton was found to be consistent with the *quark* that was introduced in order to explain the symmetries of the hadrons, and the *quark-parton model* (QPM), in which the proton consists of three quarks, was strongly supported. In order to make the QPM valid, the quarks had to be free only *asymptotically* since the free single quark had not been observed.

In 1970's, the gauge theory of the strong interaction—*quantum chromodynamics* (QCD) was proposed to explain the asymptotic free behavior of the quarks. QCD introduced the *gluon* as the gauge boson of the interaction. The momentum fraction of the proton that carried by the quarks was measured to be about half, and the remaining fraction is carried by the gluons. The scaling law was no longer valid in QCD, and deviation from the scaling law was observed by the high-energy muon beam experiment at Fermilab[8]. The structure function increases at small-x (< 0.2) and decreases at large-x (> 0.3) along with Q^2. The so-called scaling violation was explained by QCD as the $\log Q^2$-dependence of the structure function due to the *gluons* emission by quarks. The soft *sea quarks* that are pair-produced from the gluons contribute to the increase at small-x (Fig. 1.1-(d)), and the gluon emission contributes to the decrease of the hard quarks at large-x.
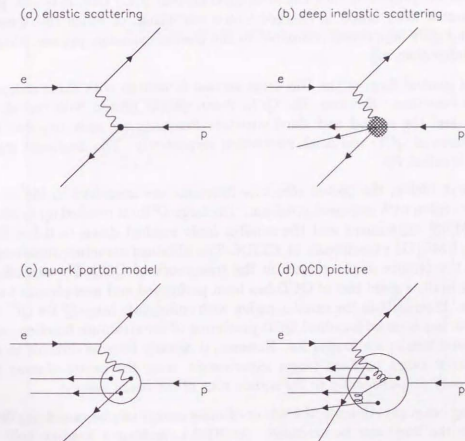
Figure 1.1: Schematic view of ep scattering at different resolution. Picture of the proton is magnified from (a) elastic scattering, (b) deep inelastic scattering, (c) quark parton model to (d) a QCD picture with sea quarks and gluons.

It also became possible to use neutrino beams to measure the structure functions, which is complementary information of the proton structure. In the neutrino scattering process the exchanged boson is the weak boson W or Z. In the case of Z-exchange, the final state lepton is also the neutrino and the process is called neutral current (NC) DIS; in the case of W-exchange, the final state lepton is a charged lepton and the process is then called charged current (CC) DIS. It is also possible to exchange a weak boson in charged lepton scattering, of which the Z-exchange process is highly suppressed compared to the photon exchange process when Q^2 is much smaller than m_Z^2.

The most general form of the DIS cross section is written with three independent structure functions. However, the QPM describes the proton with one structure function, and the second and third structure functions are only required by the modifications of QCD and weak interaction respectively. The dominant structure function is called F_2.

Throughout 1980's, the proton structure functions are measured in the extended kinematic region with increased precision. The large-Q^2 limit reached up to $260\,\mathrm{GeV}^2$ by BCDMS[9] experiment and the small-x limit reached down to 0.8×10^{-2} by EMC[10]/NMC[11] experiments at CERN. The obtained structure functions have provided the picture of the proton in the framework of QCD. By extending the kinematic limit, a good test of QCD has been performed and new physics has been looked for. Especially in the small-x region with sufficiently large-Q^2 for QCD to be valid, there has been no standard QCD prediction of the structure function, and the experimental results are longed for. However, it already became difficult to extend the kinematic range by fixed target experiments, since the center-of-mass energy increases only proportionally to the square root of the beam energy.

In colliding beam experiments, the center-of-mass energy can be raised significantly, and hence the limit can be extended. At HERA, making a head-on collision of $26.7\,\mathrm{GeV}$ electrons and $820\,\mathrm{GeV}$ protons, it became possible to measure the DIS process up to the region of about 100 times larger in Q^2 and $1/100$ times smaller in x. Fig. 1.2 shows the kinematic limit of HERA, in comparison with the regions of the previous fixed target experiments of SLAC with the electron beam and of BCDMS and NMC with the muon beam. HERA started operation in 1992 with two major detectors, ZEUS and H1, which have been taking data for two years. The first results of the structure function F_2 were already published by ZEUS[1] and H1[2], based on about $25\,\mathrm{nb}^{-1}$ data each. In the second year, about 20 times more data was acquired.

This thesis describes an updated measurement of the structure function F_2, based
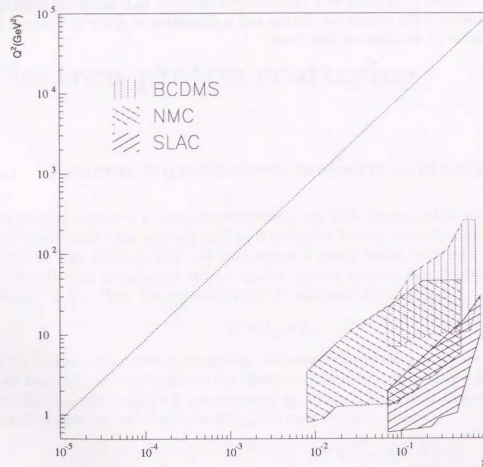
Figure 1.2: The kinematic regions of previous fixed target experiments (SLAC, BCDMS, NMC) and the kinematic limit (dotted line) at HERA with $26.7\,\mathrm{GeV}$ electron with $820\,\mathrm{GeV}$ proton.

4

5

on about $550\,\mathrm{nb^{-1}}$ data taken in the year 1993 with the ZEUS detector. The thesis is organized as follows. For the ground information of the theoretical and the experimental aspects, the DIS process is formalized in Chapter 2 and the ZEUS apparatus is described in Chapter 3. In Chapter 4 and Chapter 5 the data-taking of the experiment and the necessary Monte Carlo simulation are summarized. Kinematics reconstruction of the events is described in Chapter 6 and the final event selection is given in Chapter 7. In Chapter 8 the structure function F_2 is extracted from the data. In Chapter 9 the results are shown, and a discussion is given in Chapter 10. Finally Chapter 11 summarizes the thesis.

Chapter 2

Electron proton scattering

2.1 Neutral current deep inelastic scattering

The neutral current deep inelastic scattering (NC-DIS) process of an electron and a proton at initial 4-momenta k_μ and p_μ is generally formalized following the process shown in Fig. 2.1-(a)[4, 17].[†] By exchanging a gauge boson γ/Z with momentum q_μ, the electron is scattered and the proton breaks up into an inclusive final state denoted by X. Then, the momentum of the scattered electron k'_μ is

$$k'_\mu = k_\mu - q_\mu.$$

In the context of exploring the proton structure, the probe size to see the proton is as large as the wavelength or the inverse of the momentum of the gauge boson. Lorentz invariant variable is the square of q_μ, which is a negative definite quantity. Usually positively redefined quantity Q^2 is used for convenience.

$$Q^2 = -q^2 = -(k_\mu - k'_\mu)^2 = 2k' \cdot k - 2m_e^2 \simeq 2k' \cdot k \geq 0.$$

Implicitly m_e is neglected in the following text. Thus the probe can resolve the proton structure of $1/\sqrt{Q^2}$ in space-time scale. The center-of-mass energy squared s is given by

$$s = (k + p)^2 = 2k \cdot p + m_p^2$$

[†] All momenta are 4-momenta with $\mu = 0, 1, 2, 3 = t, X, Y, Z$ components. Spatial components are denoted by capital letters X, Y and Z in order to avoid the confusion with the kinematic variables x and y. Inner product of momenta is defined as $a \cdot b = a_\mu b^\mu = a_0 b_0 - a_1 b_1 - a_2 b_2 - a_3 b_3$, $a^2 = a \cdot a$. The light speed and the Planck's constant are set to unity ($c = \hbar = 1$) for the simplicity of equations.

Figure 2.1: (a) diagram for the inclusive neutral current deep inelastic process, (b) view with the quark-parton model.

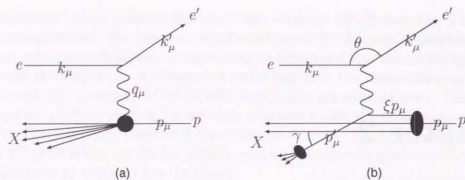where m_p is the proton mass. Then, $s - m_p^2$ is the kinematic limit of Q^2.

The proton receives the transferred momentum and breaks up into multiple hadrons. The invariant mass W of the hadron system is given by

$$W^2 = (p + q)^2 = m_p^2 + 2p \cdot q - Q^2.$$

Lorentz invariant variables are generally built from inner products of momenta, of which two of them are independent. For example $k \cdot q$, $k' \cdot p$ can be written in terms of q^2 and $p \cdot q$. Another commonly used Lorentz invariant variable ν is defined as

$$\nu \equiv \frac{p \cdot q}{m_p} = (W^2 + Q^2 - m_p^2)/2m_p,$$

which corresponds to the energy transfer by the exchanged boson in the proton rest frame. Therefore the NC-DIS process can be described in terms of two variables Q^2 and ν. It can be compared with the case of the elastic scattering process in which the proton stays unbroken, and then the process depends only one variable, say, Q^2, due to another constraint, $W^2 = m_p^2$.

Another choice of two independent invariant variables is to use the dimensionless Bjorken scaling variables x and y that are defined as

$$
\begin{aligned}
x &\equiv \frac{Q^2}{2p \cdot q} \\
y &\equiv \frac{p \cdot q}{p \cdot k}.
\end{aligned}
\tag{2.1}
$$

8

Both x and y are constrained in the ranges: $0 \le x \le 1$, $0 \le y \le 1$. There is a frequently used relation between these kinematic variables,

$$Q^2 = (s - m_p^2)xy \simeq sxy \tag{2.2}$$

where the approximation is for the case of $m_p^2 \ll s$. Since it is usually the case for the DIS experiments, this approximation is implicitly applied from now on. The proton structure functions are usually written down as functions of x and Q^2 or of x and y.

When the quark-parton model (QPM) is taken for the internal structure of the proton as Fig. 2.1-(b), the NC-DIS process can be described in terms of a superposition of electron-parton (quark) scattering sub-processes. By taking the most naive QPM the scattered parton is a free particle inside the proton, carrying no transverse momentum before scattering and making no interaction with the proton remnant after scattering. When the initial parton has a momentum fraction ξ or a momentum ξp_μ and the scattered parton has a momentum p'_μ, momentum conservation gives

$$k_\mu - k'_\mu = q_\mu = p'_\mu - \xi p_\mu.$$

Then, assuming that the parton is massless, ξ becomes

$$\xi = \frac{Q^2}{2p \cdot q} = x,$$

from the relation:

$$(p')^2 = (\xi p + q)^2 = (\xi p)^2 + 2\xi p \cdot q - Q^2 = 2\xi p \cdot q - Q^2 = 0.$$

Therefore the scaling variable x equals to the initial parton momentum fraction under the QPM.

2.2 Cross section and the structure functions

The differential cross section of the NC-DIS process of Fig. 2.1 is given by

$$\frac{d\sigma_{\rm NC}(e^{\mp}p)}{dx\, dQ^2} = \frac{4\pi\alpha^2}{xQ^4}\left[y^2 x F_1(x, Q^2) + (1 - y)F_2(x, Q^2) \pm (y - \frac{y^2}{2})x F_3(x, Q^2)\right] \tag{2.3}$$

in terms of dimensionless structure functions F_1, F_2 and F_3[5, 12]. This formula is derived from the product of a leptonic tensor $L_{\mu\nu}$ and a hadronic tensor $W_{\mu\nu}$ since:

$$d\sigma \propto L^{\mu\nu}W_{\mu\nu}. \tag{2.4}$$

9

The leptonic tensor is explicitly written down as

$$L_{\mu\nu} = 2[k_\mu k'_\nu + k'_\mu k_\nu - g_{\mu\nu} k \cdot k'] \tag{2.5}$$

for the pure photon exchange case and as

$$L_{\mu\nu} = 2[k_\mu k'_\nu + k'_\mu k_\nu - g_{\mu\nu} k \cdot k' + i\epsilon_{\mu\nu\rho\sigma} k^\rho k'^\sigma] \tag{2.6}$$

for the pure weak boson exchange case. Although the photon exchange and the weak boson exchange have different coupling constants, they can be absorbed in the structure functions in the hadronic tensor.

The generic form of the hadronic tensor is given by six different combinations of q_μ and p_μ, three of which remain as independent terms. The hadronic tensor is then written down as

$$W_{\mu\nu} = -\frac{F_1}{m_p}(g_{\mu\nu} - \frac{q_\mu q_\nu}{q^2}) + \frac{F_2}{m_p^2\nu}(p_\mu - \frac{p \cdot q}{q^2}q_\mu)(p_\nu - \frac{p \cdot q}{q^2}q_\nu) - \frac{F_3}{m_p\nu}i\epsilon_{\mu\nu\rho\sigma}p^\rho q^\sigma \tag{2.7}$$

in terms of three structure functions F_1, F_2 and F_3, that appear in Eq.2.3 as the result of the calculation of the tensor product of Eq.2.4.

When only the photon exchange is considered, parity conservation requires the tensors to be symmetric. From four symmetric combinations of p_μ and q_μ two of them remain as independent terms, and the asymmetric term with F_3, which is therefore called the weak structure function, vanishes. In fact it is a good approximation for the small-Q^2 NC-DIS ($Q^2 \ll m_Z^2$) since the propagator factor of the photon exchange $1/Q^4$ is much larger than that of the weak exchange $1/(m_Z^2 + Q^2)^2$ or that of the interference $1/Q^2(m_Z^2 + Q^2)$. Then the differential cross section is written down in terms of F_1 and F_2 only as

$$\frac{d\sigma_{\text{NC}}(e^\mp p)}{dx\, dQ^2} = \frac{4\pi\alpha^2}{xQ^4}\left[y^2 x F_1(x, Q^2) + (1 - y)F_2(x, Q^2)\right]. \tag{2.8}$$

These structure functions are related by the Callan-Gross relation[13]

$$2xF_1 = F_2 \tag{2.9}$$

in the naive QPM in which the proton consists of massless free spin-$\frac{1}{2}$ quarks that can only absorb the transversely polarized photon. In reality, the existence of the gluons makes it possible to absorb the longitudinally polarized photon, and therefore Eq.2.9 is not an exact relation. Deviation from Eq.2.9 is defined as the longitudinal structure function F_L by

$$F_L \equiv F_2 - 2xF_1. \tag{2.10}$$

The relative magnitude of F_L is suppressed by the coupling constant of the gluon radiation α_s, and it becomes largest in the small-x region where the gluon density becomes largest. Using F_L, the cross section formula Eq.2.3 is rewritten in terms of F_2, F_L and F_3 as

$$\frac{d\sigma_{\text{NC}}(e^\mp p)}{dx\, dQ^2} = \frac{2\pi\alpha^2}{xQ^4}\left[Y_+ F_2(x, Q^2) - y^2 F_L(x, Q^2) \pm Y_- x F_3(x, Q^2)\right], \tag{2.11}$$

where

$$Y_\pm = 1 \pm (1 - y)^2.$$

In Eq.2.11 the F_2 term is the dominant term.

The structure functions can be interpreted in terms of the parton densities inside the proton. In the QPM, the structure functions are given by the Q^2-independent quark densities $q_f(x)$ and anti-quark densities $\overline{q_f}(x)$ as

$$\begin{aligned}
2xF_1(x, Q^2) = F_2(x, Q^2) &= \sum_f \left[xq_f(x) + x\overline{q_f}(x)\right] A_f(Q^2) \\
xF_3(x, Q^2) &= \sum_f \left[xq_f(x) - x\overline{q_f}(x)\right] B_f(Q^2)
\end{aligned} \tag{2.12}$$

where the sum is over the all quark flavors ($f = d, u, s, c, b (, t)$). Flavor dependent coefficients A_f and B_f are complex of the coupling constants given by

$$\begin{aligned}
A_f(Q^2) &= e_f^2 - 2e_f v_e v_f P_Z + (v_e^2 + a_e^2)(v_f^2 + a_f^2)P_Z^2 \\
B_f(Q^2) &= -2e_f a_e a_f P_Z + 4v_e a_e v_f a_f P_Z^2
\end{aligned} \tag{2.13}$$

where P_Z is the ratio of the photon and Z-boson propagators

$$P_Z = \frac{Q^2}{Q^2 + M_Z^2} \tag{2.14}$$

and e_f is the electric charge ($e_e = -1$), $v_{e,f}$ and $a_{e,f}$ are the vector and axial-vector weak coupling constants of the electron and the quark defined as

$$\begin{aligned}
v_{e,f} &= [T_{e,f}^3 - 2e_{e,f}\sin^2\theta_W]/\sin 2\theta_W \\
a_{e,f} &= T_{e,f}^3/\sin 2\theta_W
\end{aligned} \tag{2.15}$$

by the third component of the weak isospin $T_{e,f}^3$ and the Weinberg angle θ_W.

Under the more realistic QCD-based model of the proton with the gluon radiation from the quark, most of the modifications from the QPM can be absorbed in the quark densities:

$$q_f(x) \rightarrow q_f(x, Q^2) = q_f(x) + \Delta q_f(x, Q^2). \tag{2.16}$$

10

11

In the term Δq_f, the $\log Q^2$-dependence from leading order QCD is included while the definitions of F_2 and F_3 stay unchanged from Eq.2.12 except for the replacement of $q_f(x) \rightarrow q_f(x, Q^2)$.

All the other corrections[5] can be included in F_L. The dominant component of F_L is derived from $\mathcal{O}(\alpha_s)$ QCD, which is given by

$$F_L^{\text{QCD}}(x, Q^2) = \frac{4\alpha_s(Q^2)}{3\pi} x^2 \int_x^1 \frac{dx'}{x'^3} F_2(x', Q^2) + \frac{2\alpha_s(Q^2)}{\pi} x^2 \int_x^1 \frac{dx'}{x'^3} (x' - x) g(x', Q^2),$$
(2.17)

where $g(x, Q^2)$ is the gluon density. The correction due to the non-zero target (proton) mass can be absorbed in F_L as

$$F_L^{\text{TM}}(x, Q^2) = 4 \frac{m_p^2}{Q^2} x^3 \int_x^1 \frac{dx'}{x'^2} F_2(x', Q^2) - 2 \frac{m_p^2}{Q^2} x^2 F_2(x, Q^2).$$
(2.18)

In addition, the $\mathcal{O}(1/Q^2)$ "higher twist" effect from the expansion of the structure function in a power series of $1/Q^2$, which is known to contribute to the cross section at small-Q^2, is parameterized as

$$F_L^{\text{HT}}(x, Q^2) = \frac{8\kappa^2}{Q^2} F_2(x, Q^2)$$
(2.19)

where $\kappa^2 \sim 0.03\,\text{GeV}^2$ is obtained[14] from SLAC data[15]. Combining all these, F_L is given by

$$F_L(x, Q^2) = F_L^{\text{QCD}}(x, Q^2) + F_L^{\text{TM}}(x, Q^2) + F_L^{\text{HT}}(x, Q^2).$$
(2.20)

2.3   Kinematics at HERA

In the HERA frame, the electron at the energy $E_e = 26.7\,\text{GeV}$ and the proton at $E_p = 820\,\text{GeV}$ make a head-on collision. Taking the proton direction as the $+Z$ direction, initial momenta of the electron and the proton are given by

$$\begin{aligned}
k_\mu &= (E_e, 0, 0, -E_e) \\
p_\mu &= (E_p, 0, 0, E_p).
\end{aligned}$$
(2.21)

In Eq.2.21, the proton mass m_p is neglected since $E_p \gg m_p$. The center-of-mass energy squared, s, becomes

$$s = (k + p)^2 \simeq 2k \cdot p = 4E_e E_p = 87576\,\text{GeV}^2.$$
(2.22)

The assumption of the QPM makes it simple to describe the kinematics of the final state. The energy and the scattering angle (the opening angle to the Z-axis) of the electron are taken to be E'_e and θ, and those of the scattered parton are taken to be E_h and γ. Setting the X-axis to the normal direction to the scattering plane, final state momenta of the electron and the parton k'_μ and p'_μ are written in terms of energies and angles:

$$\begin{aligned}
k'_\mu &= (E'_e, 0, k'_T, k'_Z) = (E'_e, 0, E'_e \sin\theta, E'_e \cos\theta) \\
p'_\mu &= (E_h, 0, p'_T, p'_Z) = (E_h, 0, E_h \sin\gamma, E_h \cos\gamma).
\end{aligned}$$
(2.23)

Kinematic variables x, y and Q^2 are defined using p_μ and q_μ, which is given by

$$q_\mu = k_\mu - k'_\mu = p'_\mu - \xi p_\mu.$$
(2.24)

Therefore, by measuring either the electron or the hadron final state, the kinematic variables can be derived. From the electron energy and angle, they are given by

$$\begin{aligned}
y_{\text{el}} &= 1 - \frac{E'_e}{2E_e}(1 - \cos\theta) \\
Q^2_{\text{el}} &= 2E_e E'_e (1 + \cos\theta) \\
x_{\text{el}} &= \frac{E_e}{E_p} \cdot \frac{E'_e(1 + \cos\theta)}{2E_e - E'_e(1 - \cos\theta)}.
\end{aligned}$$
(2.25)

This method is referred to as the "electron method." Similarly, from the parton energy and angle, the kinematic variables are given by

$$\begin{aligned}
y_{\text{had}} &= \frac{E_h(1 - \cos\gamma)}{2E_e} \\
Q^2_{\text{had}} &= \frac{(E_h \sin\gamma)^2}{1 - y_{\text{had}}} \\
x_{\text{had}} &= \frac{Q^2_{\text{had}}}{4E_e E_p y_{\text{had}}}.
\end{aligned}$$
(2.26)

Although the electron energy and the angle are measurable quantities by the calorimeter or other detectors, it is not true for the scattered parton, which turns into the current jet in the process of the hadronization to neutralize its own color charge. The proton remnant is usually observed as another jet, most of whose momentum escapes into the beampipe hole in the proton beam direction. Since it is not trivial to separate the current and remnant jets that may be connected with color force, the parton energy is not a clearly definable quantity.

12

13

Nevertheless, there is a substitution. Following two quantities

$$
\begin{aligned}
\delta_{\text{had}} &\equiv \sum_{\text{had}}(E_i - (p_Z)_i) \\
\left[\sum_{\text{had}}(p_T)_i\right]^2 &\equiv \left[\sum_{\text{had}}(p_X)_i + \sum_{\text{had}}(p_Y)_i\right]^2 ,
\end{aligned}
\tag{2.27}
$$

that are the sum of the energy minus longitudinal momentum and the vector sum of the transverse momentum over the particles of the hadron system, have little contribution from the remnant jet. They can be used as the two independent quantities rather than the energy and the angle, giving the kinematic variables as:

$$
\begin{aligned}
y_{\text{JB}} &= \frac{\sum_{\text{had}}(E_i - (p_Z)_i)}{2E_e} = \frac{\delta_{\text{had}}}{2E_e} \\
Q^2_{\text{JB}} &= \frac{(\sum_{\text{had}}(p_X)_i)^2 + (\sum_{\text{had}}(p_Y)_i)^2}{1 - y_{\text{JB}}} = \frac{(\sum_{\text{had}}(p_T)_i)^2}{1 - y_{\text{JB}}} \\
x_{\text{JB}} &= \frac{Q^2_{\text{JB}}}{4E_e E_p y_{\text{JB}}}.
\end{aligned}
\tag{2.28}
$$

This method is referred to as the "Jacquet-Blondel method"[25]. It is a good approximation since Eq.2.28 is reduced to Eq.2.26 if no particle is missing into the beampipe hole.

The parton angle can be reconstructed with this idea, from Eq.2.26 and Eq.2.28.

$$
\cos\gamma = \frac{(\sum p_T)^2 - (2E_e y_{\text{JB}})^2}{(\sum p_T)^2 + (2E_e y_{\text{JB}})^2} = \frac{(\sum p_X)^2 + (\sum p_Y)^2 - (\sum(E - p_Z))^2}{(\sum p_X)^2 + (\sum p_Y)^2 + (\sum(E - p_Z))^2}.
\tag{2.29}
$$

Then the kinematic variables obtained from this parton angle and the electron angle are given by

$$
\begin{aligned}
y_{\text{DA}} &= \frac{\sin\theta(1 - \cos\gamma)}{\sin\gamma + \sin\theta - \sin(\theta + \gamma)} \\
Q^2_{\text{DA}} &= 4E_e^2 \frac{\sin\gamma(1 + \cos\theta)}{\sin\gamma + \sin\theta - \sin(\theta + \gamma)} \\
x_{\text{DA}} &= \frac{Q^2_{\text{DA}}}{4E_e E_p y_{\text{DA}}}.
\end{aligned}
\tag{2.30}
$$

These quantities are essentially unaffected by the overall uncertainty of the absolute energy measurement. This method is referred to as the "double angle method."

Each method has different sensitivity in a different kinematic region. Contour curves of the energies and the angles are shown in Fig. 2.2. Comparison of the methods including the detector resolution is discussed in Chapter 6.
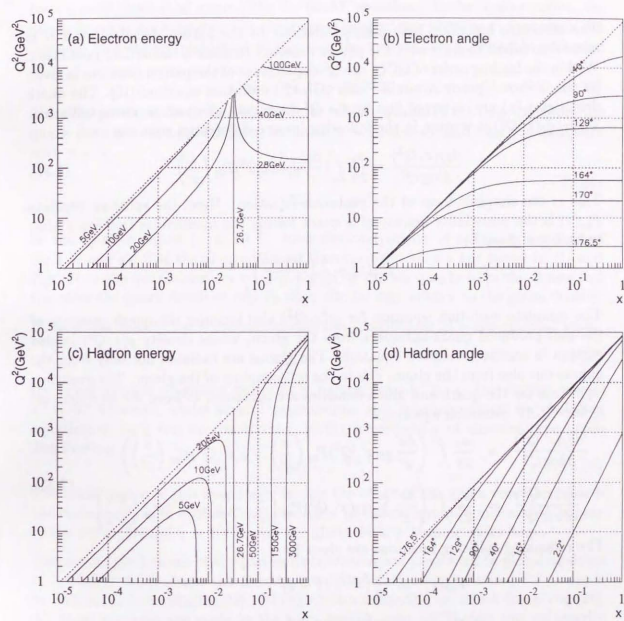
14

Figure 2.2: Contour curves of energies and angles of final state electron and hadron at the initial energies of $E_e = 26.7\,\text{GeV}$ and $E_p = 820\,\text{GeV}$.

15

2.4 Parton density and QCD

The structure functions have simple relations to the parton densities, and it is more convenient to start with the parton densities to make a theoretical prediction. Within the leading order of QCD, the Q^2-dependence of the parton densities is given by the Gribov-Lipatov-Altarelli-Parisi (GLAP) evolution equations[16]. The quark densities $q_f(x)$ are corrected first by the Q^2 dependent effect of the gluon radiation. Then, $q_f(x, Q^2)$ is written in the following integro-differential equation.‡

$$\frac{dq_f(x, Q^2)}{d \log Q^2} = \frac{\alpha_s}{2\pi} \int_x^1 \frac{dx'}{x'} q_f(x', Q^2) P_{qq}\left(\frac{x}{x'}\right). \tag{2.31}$$

This is the simplest form of the evolution equation. Here, the splitting function $P_{qq}(z)$ is the probability density of a quark having the momentum fraction z after radiating a gluon.‡

$$P_{qq}(z) = \frac{4}{3}\left(\frac{1 + z^2}{1 - z}\right)_+ \tag{2.32}$$

The complete evolution equation for $q_f(x, Q^2)$ also includes the quark contents of the pair-produced quark-antiquark from the gluon, whose density $g(x, Q^2)$ is also written in another evolution equation. The gluons are radiated not only from the quarks but also from the gluons due to the self-coupling of the gluon. The evolution equations for the quark and gluon densities are combined to form the complete set of the GLAP evolution equations:

$$\begin{aligned}
\frac{dq_f(x, Q^2)}{d \log Q^2} &= \frac{\alpha_s}{2\pi} \int_x^1 \left(\frac{dx'}{x'} q_f(x', Q^2) P_{qq}\left(\frac{x}{x'}\right) + g(x', Q^2) P_{qg}\left(\frac{x}{x'}\right)\right) \\
\frac{dg(x, Q^2)}{d \log Q^2} &= \frac{\alpha_s}{2\pi} \int_x^1 \left(\frac{dx'}{x'} \sum_f q_f(x', Q^2) P_{gq}\left(\frac{x}{x'}\right) + g(x', Q^2) P_{gg}\left(\frac{x}{x'}\right)\right)
\end{aligned} \tag{2.33}$$

The remaining splitting functions are given by

$$\begin{aligned}
P_{qg}(z) &= \frac{1}{2}\left(z^2 + (1 - z)^2\right) \\
P_{gg}(z) &= 6\left(\frac{1 - z}{z} + \frac{z}{1 - z} + z(1 - z)\right)_+ \\
P_{gq}(z) &= \frac{4}{3}\left(\frac{1 + (1 - z)^2}{z}\right)_+.
\end{aligned} \tag{2.34}$$

---

‡ The "+" symbol in the equation is the so-called "+ prescription" which cancels the infrared divergence at $z \to 1$.

16

On the other hand the x-dependence of the parton distributions cannot be obtained from a solid theoretical ground like the GLAP equations. In the large-x region, the quark densities are suppressed by the number of spectator partons, n, that share the remnant momentum, and based on this idea the x-dependence is roughly estimated by

$$q(x) \overset{x \to 1}{\sim} (1 - x)^{2n-1}. \tag{2.35}$$

Since the proton is dominated by the three valence quarks in the large-x region, the quark densities are approximated by using $n \sim 2$, and similarly for the antiquark with $n \sim 4$:

$$\begin{aligned}
q(x) &\overset{x \to 1}{\sim} (1 - x)^3, \\
\bar{q}(x) &\overset{x \to 1}{\sim} (1 - x)^7.
\end{aligned} \tag{2.36}$$

In the small-x region ($x < 10^{-2}$), from the comparison of splitting functions of Eq.2.32 and Eq.2.34 the gluons become dominant due to the $1/z$ factor in P_{gq} and P_{gg}. Then the quark densities are dominated by the sea quarks from the gluons and therefore the quark densities and F_2 show similar dependence to the gluon density.

If the gluon density has a bremsstrahlung-like distribution of a non-singular type,

$$xg(x) \sim x^0, \tag{2.37}$$

the total number of gluons grows only logarithmically in an integration toward $x \to 0$. However, under several assumptions and approximations, an evolution equation in $\log \frac{1}{x}$ can be constructed, giving a prediction of singular type gluon distribution,

$$xg(x) \sim x^{-0.5}. \tag{2.38}$$

The main reason of this singularity is that the effect of the gluon recombination is not considered. It is expected that the effect of the recombination starts to appear in the region around $x \sim 10^{-4}$, after the gluon density became quite large.

Theoretical predictions of the parton distributions are proceeded in global analyses of available results from the fixed-target DIS or other experiments, for example by Martin-Roberts-Stirling[26], CTEQ Collaboration[27] or Glück-Reya-Vogt[28]. All these analyses are made in the next-leading-order QCD that was necessarily introduced to explain the experimental data. Although they use a similar set of data and similar theoretical tools, there is a large difference between predictions especially in the small-x region attainable with HERA. For example, two different parametrizations of MRS take a following function form for the gluon density at a fixed Q^2,

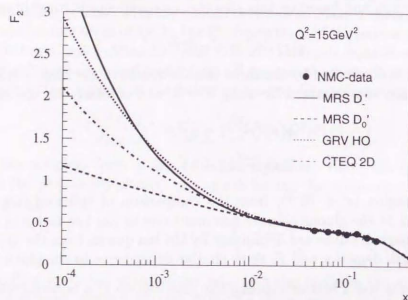$$xg(x) = A_g x^{\delta_g}(1 - x)^{\eta_g}(1 + \gamma_g x)$$

17

Figure 2.3: Various predictions of F_2. Shown data points are taken from the NMC results.

where $\delta_g = 0$ for the non-singular parametrization (D_0') and $\delta_g = -0.5$ for the singular parametrization (D_-'). CTEQ uses a similar function form,

$$xg(x) = A_0 x^{A_1}(1-x)^{A_2}(1 + A_3 x^{A_4})[\log(1+\frac{1}{x})]^{A_5}$$

where $A_1 \sim -0.3$ is obtained by including the previous HERA F_2 results. GRV starts the evolution from a very small $Q^2 \sim 0.3\,\text{GeV}^2$, where they assume that at such low-Q^2, valence-like parton densities can be used down to very small x ($\sim 10^{-4}$), although the theoretical validity is questionable. The resulting rise of the gluon density is effectively comparable to $\sim x^{-0.4}$ parametrization.

In Fig. 2.3 various predictions of F_2 at $Q^2 = 15\,\text{GeV}^2$ are shown together with the fixed-target data of NMC[11]. It is clearly seen that there is a large discrepancy in the HERA region of small-x.

2.5 Other processes at HERA

There is a wide variety of physics processes that are observed or expected in the electron-proton collision at HERA[17–19]. In the framework of the Standard Model, most of the events are classified into the one gauge boson (photon) exchange process of either the DIS with large-Q^2 or the photoproduction with a very small-Q^2 but with large photon energy.

The DIS process is further classified into NC-DIS (Fig. 2.4-(a)) of photon/Z exchange and CC-DIS (Fig. 2.4-(b)) of W exchange. In NC-DIS, the scattered electron is found in the detector; in CC-DIS, the neutrino with a large momentum escapes undetected and the event is identified by the large missing transverse momentum. While the cross section of NC-DIS has the $1/Q^4$ dependence, the CC-DIS cross section is very small if $Q^2 \ll m_W^2$. The HERA energy can however reach the region of $Q^2 \gtrsim m_W^2$ where the NC-DIS and CC-DIS cross sections become comparable.

The photoproduction process has a very large cross section since Q^2 is very small. If the transverse energy of the final state is small, the partonic picture of QCD cannot be applied and the process is inclusively called soft-photoproduction (Fig. 2.4-(c)). If the transverse energy is so large that the sub-process can be handled by QCD, the partons are observed as jets in the detector. The hard process are classified into the direct process and the resolved process. In the direct process the photon directly interacts with the gluon (boson-gluon fusion, Fig. 2.4-(d)) or with the quark (QCD compton) constituent of the proton. In the resolved process the virtual hadronic constituent of the photon interacts with the constituent of the proton (Fig. 2.4-(e), in the case of gluon-gluon interaction).

The event with small-Q^2 and small photon energy is usually undetected by the detector. There are several exceptions, for example the elastic QED compton process (Fig. 2.4-(f)) may have as large an opening angle between the final state photon and electron as to be detected in the detector.

(a) NC DIS

(a) CC DIS

(c) soft photoproduction

(d) direct hard process

(e) resolved hard process

(f) QED compton
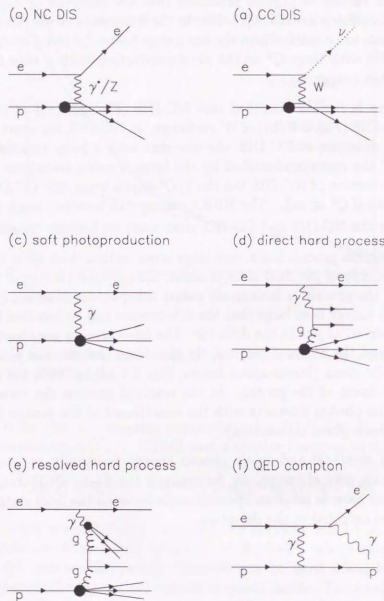
Figure 2.4: Schematical diagrams for various processes at HERA.

Chapter 3

ZEUS experiment at HERA

3.1   HERA electron-proton collider

The first electron-proton collider HERA was constructed at DESY (Deutsches Elektronen Synchrotron) in the western suburb of Hamburg, Germany. HERA was designed to accelerate the electron to 30 GeV and the proton to 820 GeV, giving 314 GeV center-of-mass energy. The layout of the HERA accelerator is shown in Fig. 3.1; the main design parameters are given in Table 3.1. Two separate main ring synchrotrons for the electron beam and for the proton beam have circumferences of 6.3 km and are placed in the same tunnel, most part of which is extended to the outside of the DESY site. The pre-acceleration is done in a complex of the previously available accelerators at DESY with minor modifications. The electron beam is accelerated to 14 GeV in the chain of an electron-linac, DESY II and PETRA II for injection, then to the final 30 GeV energy in the main ring. The proton beam is accelerated to 40 GeV in the chain of an H^--linac, DESY III and PETRA II for injection, then to the final 820 GeV energy in the main ring. Beams are circulated in off-colliding orbits during the acceleration, then are adjusted to the colliding orbits after reaching the final energies. The lifetime of the proton beam is typically longer than 24 hours; the lifetime of the electron beam is typically several hours.

The luminosity of a colliding experiment is proportional to the intensities of the both beams, inverse of the beam sizes at the crossing point and the frequency of the crossing per unit time. Since it takes a long time of 21.1 μs for a particle to travel over the 6.3 km circumference, it is divided into 220 bunches of 28.8 m (96 ns) interval to carry the beam particles, of which 210 are filled with particles to gain the crossing frequency. The design luminosity of HERA is $1.5 \times 10^{31}\,\mathrm{cm}^{-2}\,\mathrm{s}^{-1}$, with
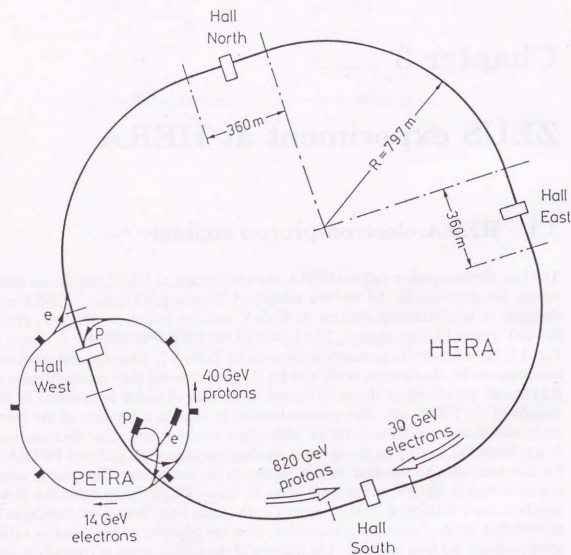
Figure 3.1: HERA electron-proton collider.

	proton ring		electron ring	units
Nominal energy	820		30	GeV
c.m. energy		314		GeV
Q^2_{max}		98400		GeV^2
Luminosity		1.5×10^{31}		cm^{-2}s^{-1}
Polarization time	—		28	min
Number of interaction points		4		
Crossing angle		0		mrad
Free space for experiments		±5.5		m
Circumference		6336		m
Length of straight sections		360		m
Bending radius	588		608	m
Magnetic field	4.65		0.165	T
Energy range	300–820		10–33	GeV
Injection energy	40		14	GeV
Circulating current	160		58	mA
Total number of particles	2.1×10^{13}		0.8×10^{13}	
Number of bunches		200		
Number of bunch buckets		220		
Time between crossings		96		ns
Emittance (ϵ_x/ϵ_y)	0.71/0.71		3.4/0.7	10^{-8}m
Beta function (β_x^*/β_y^*)	10/1.0		2/0.7	m
Beam tune shift (Q_x/Q_y)	0.0026/0.0014		0.023/0.026	
Beam size at crossing σ_x^*	0.27		0.26	mm
Beam size at crossing σ_y^*	0.08		0.07	mm
Beam size at crossing σ_z^*	11		0.8	cm
Energy loss/turn	1.4×10^{-10}		127	MeV
Total RF power	1		13.2	MW
RF frequency	52.033/208.13		499.667	MHz
Filling time	20		15	min

Table 3.1: Design parameters of HERA

$8 \times 10 + 4$ colliding bunches

5×2 e-unpaired bunches   6 p-unpaired bunches
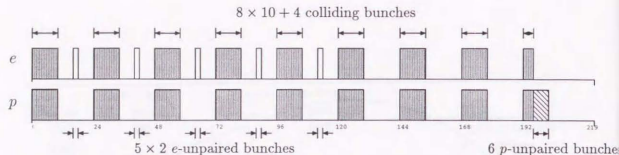
Figure 3.2: Typical bunch structure during the 1993 run period, with 84 colliding bunches, 10 e-unpaired bunches and 6 p-unpaired bunches.

which an integrated luminosity of 200 pb^{-1} is obtained in a stable one year operation.

There are four interaction points, where the both beams are focused to have minimum spatial sizes and to cross at 0° angle, at the centers of four 360 m straight sections. Experimental halls are prepared at the interaction points to measure the collision. Two of them are occupied by multi-purpose detectors ZEUS (South-hall) and H1 (North-hall).

The first luminosity was observed in October 1991 between one-bunch 12 GeV electron and one-bunch 480 GeV proton in a machine-study operation of HERA. In the beginning of 1992 both the ZEUS and the H1 detectors are installed at the interaction points, and in May 1992 the first electron-proton scattering events between 26.7 GeV electron and 820 GeV proton are recorded by both experiments. There have been three major run periods in the first two years, the "1992-summer" run period, the "1992-fall" run period and the "1993" run period. Between these run periods both HERA and the detectors were shutdown for upgrade.

In the two year operation of 1992/1993, the beam energies were fixed to 26.7 GeV electron and to 820 GeV proton. The typical numbers of bunches were 9+1 for electron and 9+1 for proton in 1992 (it means there are 9 colliding bunches, 1 unpaired electron bunch and 1 unpaired proton bunch), and were 84+10 for electron and 84+6 for proton in 1993. The unpaired bunches are recorded by both experiments. The unpaired bunches are especially important in the luminosity measurement in order to subtract the background from interaction between the electron beam and the residual gas in the beampipe (electron beam-gas background). They are also useful to estimate the contamination from the electron beam-gas and the proton beam-gas (interaction of the proton beam with the residual gas) events observed in the main detector. A typical bunch structure used during the 1993 run period is shown in Fig. 3.2.

The ZEUS experiment recorded about 3 nb^{-1}, 30 nb^{-1} and 600 nb^{-1} integrated luminosities respectively in the 1992-summer, 1992-fall and 1993 run periods.

3.2 Overview of the ZEUS detector

ZEUS experiment[21] is one of two multi-purpose large detector experiments at HERA. The central components of the ZEUS detector are the calorimeter, the tracking detectors and the muon detectors in order to measure the particles from the collision at 314 GeV center-of-mass energy. It has a forward-backward asymmetric shape, since the center-of-mass system is strongly boosted toward the proton beam (forward) direction. The forward half has a more elaborate construction: for example the calorimeter is thicker to stop the energetic hadrons and the tracking detector has more layers to identify tracks with high multiplicity.

The ZEUS detector is a hermetic detector except for the unavoidable beampipe hole in the forward and backward beam direction. Most of the detectors are mechanically divided into three parts to cover the forward, central (barrel) and backward (rear) regions with sufficiently overlapping boundaries. Especially the calorimeter has a solid angle coverage of 99.8 % in the forward hemisphere and 99.5 % in the backward hemisphere.

Views of the ZEUS detector are given in Fig. 3.3 (longitudinal cut) and 3.4 (transverse cut at the interaction point). The detector complex consists of, ordering from the interaction point to the outside, a tracking detector complex (VXD, CTD, FDET and RTD in the figures) in a solenoid magnetic field, calorimeters (FCAL, BCAL and RCAL) to measure the energy of particles, and muon detectors (FMUI, FMUON, BMUI, BMUO, RMUI and RMUO) with backing calorimeters (BAC) in the iron return yoke.

The coordinate system of ZEUS is a right-handed orthogonal coordinate: the origin $(0,0,0)$ is at the nominal interaction point, the $+Z$-axis is the proton beam direction, the $+Y$-axis is the up-going direction and the $+X$-axis is the horizontal direction toward the center of the HERA ring. A polar coordinate system (r, θ, ϕ) and a cylindrical coordinate system (R, ϕ, Z) are also used for convenience. The polar angle θ is the angle with respect to the $+Z$ axis and the azimuthal angle ϕ is the angle with respect to the $+X$ axis in the X-Y plane. The radius r and R are the distance from the interaction point and from the beam axis, respectively. The proton going direction is $\theta = 0°$ and the electron going direction is $\theta = 180°$.

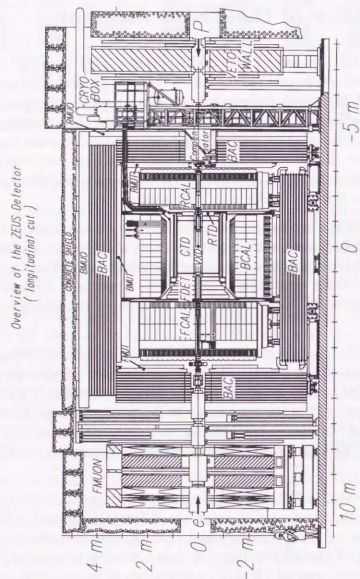Figure 3.3: Side view of the ZEUS detector.
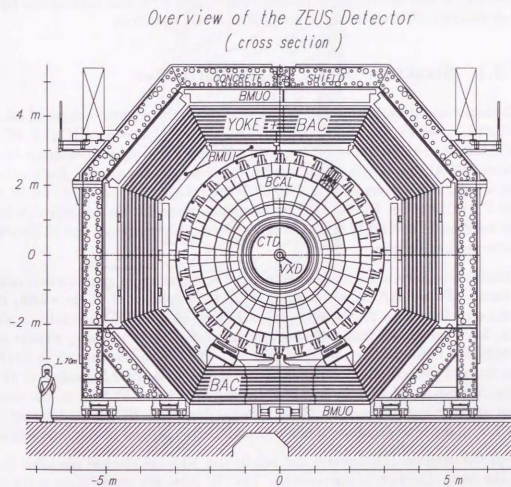
Overview of the ZEUS Detector
(cross section)

Figure 3.4: Cross section of the ZEUS detector at the interaction point.

3.3 Calorimetry

One of the major characteristics of the ZEUS detector is in its main calorimeter (CAL)[22]. By adopting a depleted uranium/scintillator sampling calorimeter, CAL has an equal energy response to electrons (and photons, π^0's) and to hadrons, and thus has a good energy resolution to hadrons. CAL also provides good position and timing resolution and a good electron identification ability. In addition, a silicon-pad detector for hadron-electron separation (HES) and a backing calorimeter (BAC) for leak energy measurement serve as supplementary detectors.

3.3.1 Structure of the main calorimeter

The main calorimeter is divided mechanically into three parts: a forward calorimeter (FCAL), a barrel calorimeter (BCAL) and a rear calorimeter (RCAL). FCAL and RCAL have a similar flat structure, with a $20\,\mathrm{cm} \times 20\,\mathrm{cm}$ square beampipe hole at the center. BCAL has a cylindrical structure around the beam axis. Each calorimeter has a polar angle coverage of $2.2°$ to $39.9°$ for FCAL, $36.7°$ to $129.1°$ for BCAL and $128.1°$ to $176.5°$ for RCAL. CAL is hermetic except for the beampipe holes, with the solid angle coverages of $99.8\,\%$ in the forward hemisphere and of $99.5\,\%$ in the backward hemisphere.

Calorimeters have a modular structure for convenience in construction and maintenance. FCAL and RCAL consists of 23 tall modules of $20\,\mathrm{cm}$ width, that are numbered from 1 to 23 along the X-axis. One of the FCAL modules is shown in Fig. 3.5. The global transverse shape is almost a circle by using shorter modules toward the both ends as shown in Fig. 3.6. The central module 12 is divided into the top and the bottom modules at the beampipe hole. BCAL consists of 32 wedge-shaped modules of $24.5\,\mathrm{cm}$ width at the inner end and $57.5\,\mathrm{cm}$ at the outer end, that are numbered from 1 to 32 along the ϕ direction. BCAL modules are skewed by $2.5°$ in order to avoid the module boundaries to project to the interaction point.

Depleted uranium (DU) plates and scintillator tiles are stacked one after the other in the depth direction of the modules. The DU plate is a single plate of the module-height length. The length of the scintillator tile varies from 5 to 20 cm depending on the place to use. The thickness of the DU-plate is 3.3 mm and that of the scintillator is 2.6 mm, together forming a layer of one radiation length $(1X_0)$ material. In the depth direction, calorimeters are divided into an electromagnetic calorimeter (EMC) to measure shallow and narrow electromagnetic showers and a hadron calorimeter (HAC) to measure deep and wide hadronic showers. EMC is the first 25 layers

28
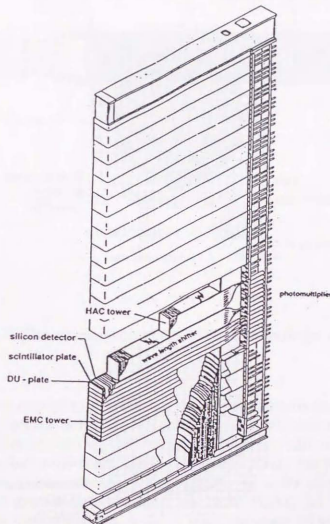
Figure 3.5: FCAL module structure.

29

(a) FCAL segmentation

☒beampipe
▦EMC
☐HAC0

(b) RCAL segmentation

☒beampipe
▤EMC
☐HAC0
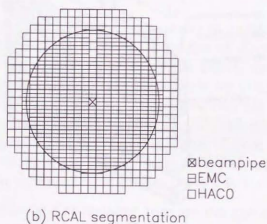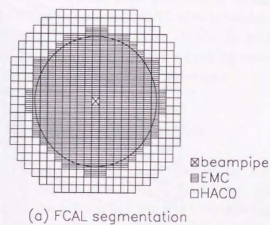
Figure 3.6: Transverse segmentations of FCAL(top) and RCAL(bottom) viewed from the interaction point. Outside the circle is the shadowed area by BCAL looking from the interaction point.
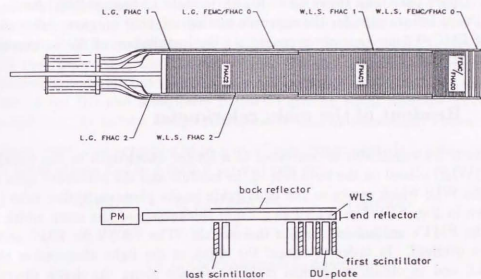
Figure 3.7: The optical readout of one module through the wavelength shifter.

$(25X_0)$, that is deep enough to stop most of the electromagnetic shower development. The segmentation is finer in EMC, with the transverse cell sizes of $5\,\mathrm{cm} \times 20\,\mathrm{cm}$ in FCAL, $4.9\,\mathrm{cm} \times 23\,\mathrm{cm}$–$5.7\,\mathrm{cm} \times 27\,\mathrm{cm}$ in BCAL and $10\,\mathrm{cm} \times 20\,\mathrm{cm}$ in RCAL. BCAL EMC tiles are stacked projectively to the interaction point. For hadrons, the EMC depth corresponds to one interaction length (1λ). In order to stop the hadronic showers, the total depths of EMC+HAC are 7λ in FCAL, 5λ in BCAL and 4λ in RCAL. HAC is further divided in depth into two parts (HAC1 and HAC2) in FCAL/BCAL. The transverse HAC cell sizes are $20\,\mathrm{cm} \times 20\,\mathrm{cm}$ in FCAL/RCAL and $23\,\mathrm{cm} \times 27\,\mathrm{cm}$–$43\,\mathrm{cm}$ in BCAL. Two successive (one in RCAL) HAC cells and four (two in RCAL) EMC cells with a common section are combined to form a tower. In FCAL/RCAL towers are numbered from 1 to 23 along the Y-axis (tower 12 is always assigned at the same height as the beampipe hole), and in BCAL towers are numbered from 1 to 14 along the Z-axis.

In addition, there are following detailed structure of CAL. The outer regions of

FCAL/RCAL surface are shadowed by the edges of BCAL which prevent those regions from serving as the electromagnetic calorimeters, and therefore the front 25 layers, that are segmented into the same size as HAC, 20 cm × 20 cm, are called HAC0. Upper part than tower 15 of RCAL module 12 has no EMC for the space of the liquid-helium pipe for the superconducting solenoid magnet. After the third layer of EMC, 1.5 cm gaps are prepared for the installation of the hadron-electron separator (HES).

3.3.2 Readout of the main calorimeter

Light from the scintillator is converted to a longer wavelength in the wavelength-shifter (WLS) placed on the both side of the module and the converted light travels along the WLS which serves as the light guide to the photomultiplier tube (PMT) as shown in Fig. 3.7. The WLS has a 2 mm thickness and the same width as the cell. The PMT's are located behind the module. The WLS's for EMC and HAC cells are overlaid. In order to cancel the effect of the light attenuation through the WLS and to obtain a uniform energy response along the depth direction, a black pattern is printed on the back reflector of the WLS. The uniformity of the energy response versus the transverse position in a cell is achieved by a printed black pattern on the paper wrapping to correct the light attenuation effect through the scintillator. In addition, in order to avoid the energy leakage through the thin material of the WLS between modules, 2.6 mm thick lead sheets are put between modules in FCAL/RCAL and 0.8 mm thick lead sheets are put on both sides of modules in BCAL.

The PMT signals are individually amplified by shaping amplifiers and temporarily stored in analog pipelines until the trigger decision is given. The pipeline consists of an array of capacitors, which hold the charges integrated over every 96 ns beam crossing interval. If the trigger accepts the event, four successive charge samples including the event bunch are digitized, and the original signal shape is reconstructed from them. The reconstructed shape is then converted into the energy and timing, in which all the calibrations are taken into account.

3.3.3 Resolution and calibration

The ZEUS main calorimeter is characterized by its good hadron energy resolution. A hadron shower usually gives a smaller energy response than an electromagnetic shower, due to particles like neutron, muon or neutrino that have small or little

interaction with material, and due to the thermal energy loss of heavy and slow particles. When correcting this effect for an identified hadron shower, still the unknown fraction of the π_0 component which decays into two photons in the course of the shower development causes a large fluctuation in the energy response. By using depleted uranium (DU) as the absorber material, the loss due to slow neutrons is compensated. When a slow neutron is captured by the nucleus of ^{238}U, it generates multiple fast neutrons in the fission reaction. These neutrons kick the protons in the scintillator material and then recovery of the energy is obtained. By tuning the thickness of the DU and scintillator plates to give an equal response to electrons and to hadrons, the hadron energy resolution becomes substantially better.

The energy resolution is measured in a test beam experiment. It is measured up to 75 GeV for electrons and to 100 GeV for hadrons as:

$$\sigma(E)/E = 18\%/\sqrt{E} \oplus 1\% \qquad \text{for electron}$$
$$\sigma(E)/E = 35\%/\sqrt{E} \oplus 2\% \qquad \text{for hadron} \qquad (3.1)$$

(E in GeV, addition in quadrature.)

The electron/hadron energy response ratio is unity within 3 % for the particle with > 3 GeV momentum. The time resolution is obtained as:

$$\sigma(t) = (0.5 \oplus 1.5/\sqrt{E})\,\text{ns} \qquad (E \text{ in GeV, addition in quadrature}). \qquad (3.2)$$

The energy calibration has been performed in various ways. The modules are calibrated within 1 % precision by cosmic ray muons before the installation into the ZEUS setup. After the installation, the radioactivity of DU provides a good source for the continual calibration of the PMT's. Electronics are independently calibrated by injecting charge pulses. In addition cosmic ray muons and beam halo muons have been used for the further calibration of the gain in situ.

3.3.4 HES

The rear hadron electron separator (HES, or explicitly RHES) consists of silicon detector pads inserted in the RCAL after the front $3X_0$ layers, that is near the shower maximum of the electromagnetic shower.[†] The size of the silicon pad is 3 cm × 3 cm, in such a way that 6×6 of them fit into a single RCAL tower. An

---

[†] RHES is partially equipped in the 1992/1993 run periods. FHES/BHES for FCAL/BCAL are of future update plans.

electromagnetic shower deposits a large amount of energy at RHES, while a hadronic shower is not developed much yet, depositing little energy. Although the isolated DIS electron can be identified with a high efficiency by the calorimeter only, the electron from a semi-leptonic decay of a heavy quark that resides within a jet is difficult to be identified without the help of HES. The better granularity also gives a better position resolution and a better particle separation than the calorimeter.

RHES has the energy resolution to identify a minimum ionizing particle. With RHES alone, the hadron mis-identification rate is 5 % when the electron identification efficiency is 90 %. Combining with the calorimeter electron identification, RHES improves the hadron electron separation by a factor of 5, especially for a low energy electron of 2 GeV. The electron position resolution of RHES is obtained to be 6 mm in average.

3.3.5   Backing calorimeter

The iron return yoke of the solenoid magnetic field, outside of the main calorimeter, is used as the absorber material for the backing calorimeter (BAC) that consists of proportional chambers. When the hadronic shower develops deep in the calorimeter, sometimes the main calorimeter cannot stop all the energies and leak some of them, that can be measured by BAC. Or, BAC can be used as a veto counter for this type of hadrons to retain a good hadronic resolution of the main calorimeter.

There are 7 to 10 layers of chambers, which have a unit cell size of $15\,\text{mm} \times 11\,\text{mm}$. In addition to the wire readout, $50\,\text{cm} \times 50\,\text{cm}$ pad readout provides the position along the wire. The energy resolution of BAC is obtained to be $100\,\%/\sqrt{E}$.

3.4   Inner Tracking Detectors

Trajectories of charged particles before reaching the calorimeter are measured by inner tracking detectors under the solenoid magnetic field of 1.8 T. A central tracking detector (CTD), a forward detector (FDET), a rear tracking detector (RTD) and a vertex detector (VXD) provide the inner tracking of ZEUS, as shown in Fig. 3.8.
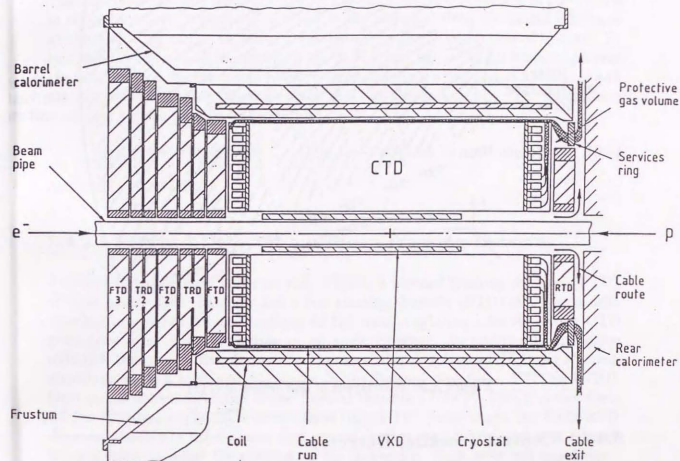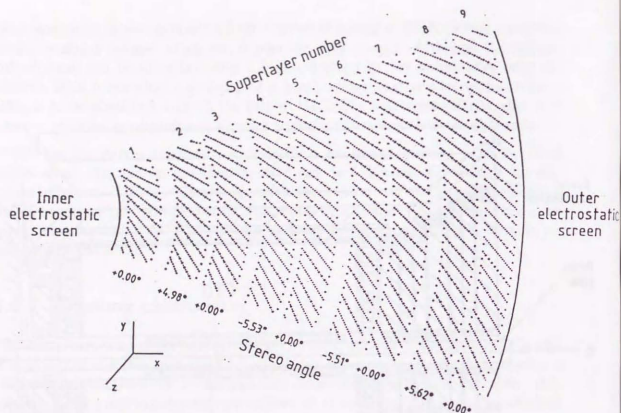

Figure 3.8: Layout of inner tracking detectors.

34

35

Figure 3.9: Wire layout of one octant of CTD.

3.4.1 Central Tracking Detector

The central tracking detector (CTD) is a large cylindrical wire drift chamber[23]. Having dimensions of 241 cm length, 16.2 cm inner radius and 85 cm outer radius, CTD consists of 9 super-layers (SL), each of which has 8 layers of sense wires. Odd number super-layers (SL1,3,5,7,9 ordering from inner) have wires parallel to the beam axis; even number super-layers have skewed wires with stereo angles of about 5° to gain as good a polar angle resolution as the azimuthal angle resolution. The wire configuration of one octant is shown in Fig. 3.9. The polar angle coverages are 11.3°–168.2° at the most inner SL1, 15°–164° at the SL2 to take the minimum advantage of the stereo wires and 36.1°–142.6° at the SL9 for the particle that goes through all the super-layers of CTD.

The electron drift volume is a polygonal cell that consists of 38 wires including 8 sense wires and that is inclined 45° of Lorenz angle to the radial direction to set the electron drift direction tangent to the azimuthal direction. CTD has 576 cells, with 4608 sense wires in total.

The design hit position resolution is 100–120 μm in the R-ϕ plane and is 1.0–1.4 mm in the Z direction. A robust Z-position is also obtained from the timing difference at the both ends of the hit wire (Z-by-timing), with the resolution of < 3 cm. Z-by-timing readout is implemented on all of SL1 and half of SL3,5 wires to provide the seed position for the stereo position reconstruction, a fast signal for trigger and for the position of the small angle track that has hits only in SL1. The momentum resolution for the particle at $\theta = 90°$ is

$$\sigma(p)/p = 0.002p \oplus 0.003 \qquad (p \text{ in GeV, addition in quadrature}) \qquad (3.3)$$

under the 1.8 T field.

3.4.2 Forward Detector and Rear Tracking Detector

Adjacent to the forward and rear end of CTD, a forward tracking detector (FTD) of three planar drift chambers and a rear tracking detector (RTD) of a planar drift chamber are placed for the tracking of the small angle particles for which CTD gives poor polar angle resolution or no angle coverage. In addition, a transition radiation detector (TRD) is installed between the chambers of FTD for electron identification in a high multiplicity jet in the forward direction.[‡] FTD and TRD form an assembled structure of the forward detector (FDET). FDET covers from 7.5° to 28° polar angle; RTD covers from 160° to 170° polar angle. An FTD/RTD chamber consists of three planer drift chambers that are 120° rotated with respect to each other to point the position of the trajectory. Each drift cell has 6 sense wires.

3.4.3 Vertex Detector

A vertex detector (VXD) is placed inside of CTD, especially for the purpose of the decay vertex position measurement of short-lived particles. VXD is a drift chamber of azimuthally divided 120 cells that provides a fine resolution in the R-ϕ plane. Each cell has 12 sense wires that are parallel to the beam axis.

[‡] FTD, RTD and TRD were not read out in 1992/1993 run periods.

3.5 Luminosity Measurement

Luminosity of the ZEUS experiment is measured by counting the rate of the bremsstrahlung process $ep \to e'\gamma p$, which has advantages of:

- precisely given QED cross section,
- sufficiently large interaction rate for continuous online monitoring and for low statistical error,
- clean signal that can be measured with a simple detector and
- well-known background contributions that can be safely estimated.

There is little energy transfer to the proton in the bremsstrahlung process, and thus the sum of the final electron energy E'_e and the photon energy E_γ equals to the electron beam energy E_e.

The cross section for 30 GeV electrons and 820 GeV protons with 14–19 GeV final electron energy range is 15.4 mb, which gives a sufficient count rate for the luminosity of $10^{30}\,\mathrm{cm}^{-2}\,\mathrm{s}^{-1}$. The largest background is from a similar bremsstrahlung process of electrons with residual gas atoms in the beampipe (e-gas background). Although this background cannot be distinguished from the final state, the contribution can be obtained from the counting rate of the unpaired electron bunches weighted by the beam current of bunches, and then can be subtracted. There are no other significant background source to the counting rate.

The luminosity detector (LUMI) is a pair of calorimeters to detect the signals of the electron and the photon of the process. The layout of LUMI is shown in Fig. 3.10. The photon emitted at very little angle is detected by a γ-calorimeter, that is located at 108 m downstream from the interaction point, after traveling straight through the bending magnets of the electron beam. The γ-calorimeter is a lead-scintillator sampling calorimeter that measures the photon energy. In front of the calorimeter, a carbon filter of $1X_0$ to absorb the soft photons from synchrotron radiation and a Čerenkov counter to veto the converted e^+e^- in the carbon filter. The electrons are detected in an e-calorimeter after bent by magnets at a larger angle than the beam. The e-calorimeter, which is a similar lead-scintillator calorimeter to the γ-calorimeter, is located inside of the electron ring at 35 m downstream from the interaction point. The acceptance of the e-calorimeter is energy dependent since the trajectory of the final state electrons varies with the energy and the scattered angle. For example it is better than 70 % in the range of $0.35E_e < E'_e < 0.65E_e$.
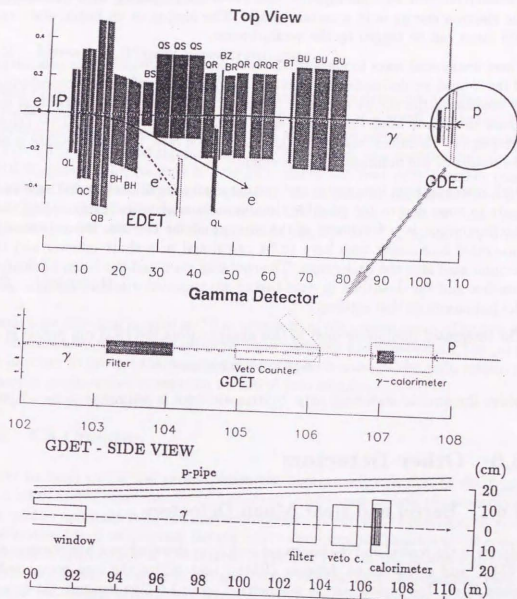

Figure 3.10: Layout of the luminosity detector. QL–QB and BH are the focusing and bending magnets for the electron beam; QS–QR and BS–BU are the focusing and bending magnets for the proton beam.

These calorimeters are also used as tagging detectors of electrons and photons. The scattered electron in a photoproduction event can be tagged by the e-calorimeter if the electron energy is in a certain range. The photon of an initial state radiative DIS event can be tagged by the γ-calorimeter.

There are several ways to measure the luminosity: by counting the coincidence rate of the γ- and e-calorimeter, by counting the single rate of the γ- or e-calorimeter or by measuring the energy spectrum of the γ-calorimeter. A comparison of methods shows there is a large systematic error from the uncertainty in the e-calorimeter acceptance. Therefore, instead of the coincidence rate, the γ single rate is used for the results of the luminosity measurement.

Both instantaneous luminosity and instantaneous e-gas background rate may fluctuate in time due to the possible time variations of both beams. Main reason of the fluctuation is a few hours of the lifetime of the electron beam intensity. The integrated luminosity thus have to be calculated in a short interval and then be accumulated over the time range. The counting rates and the beam intensity for all bunches and the deadtime in data-taking are recorded every 15 seconds to obtain the luminosity of that interval.

The integrated luminosity used in this analysis from the 1993 run period is

$$543.233 \pm 0.036\,\mathrm{nb}^{-1}$$

where the error is statistical only. Systematic error is estimated to be 4 %[30].

3.6   Other Detectors

3.6.1   Barrel and Rear Muon Detectors

Muons in the central and the backward region are detected by a barrel muon detector (BMU) and a rear muon detector (RMU) that utilize the iron return yoke as a muon filter. The return yoke is magnetized up to 1.6 T to measure the momentum of muons. The direction of muons are measured in limited streamer tube (LST) chambers that are placed just inside (BMUI and RMUI) and outside (BMUO and RMUO) of the yoke. Each chamber consists of two double layers of LST's, that are separated by ~ 20 cm for inner and by ~ 40 cm for outer chambers. All LST's are parallel aligned; positions along the LST are read out by external strips attached orthogonally to the LST. By measuring the particle direction at the inner and outer chambers the muon identification and the momentum determination are performed.

By comparing the momentum with that of CTD, muons that do not originate from the interaction point are rejected.

3.6.2   Forward Muon Spectrometer

A forward muon spectrometer (FMUON) offers the muon detection and the momentum measurement in the forward direction. Especially at a small angle, the muon momentum have to be measured by FMUON alone since the momentum resolution by CTD+FTD is degraded significantly. FMUON, which is a tracking detector in a toroidal magnetic field, consists of four LST planes and four drift chamber planes, of which an LST and a drift chamber plane are located inside the forward iron yoke. In addition, two LST walls cover the angle to the BMU edge. FMUON has a polar angle coverage of 5°–30° and momentum resolution of < 30 % up to 100 GeV muons.

3.6.3   Vetowall

Vetowall is an iron wall located at 7.5 m upstream of the proton beam. The iron wall of 87 cm thickness absorbs the off-beam halo particles accompanied by the proton beam in order to protect the main detector. On both sides of the wall, scintillator hodoscopes are arranged to serve as an active veto counter.

3.6.4   C5 Counter

In order to carry out a fast proton beam-gas background rejection at the trigger level, a small scintillation counter (C5 counter) is arranged around the beampipe at 3.15 m proton upstream from the interaction point. Around the beampipe, there are a lot of material such as magnets, flanges and collimators; the location of the counter corresponds to just inside of the nearest collimator (C5) in the proton upstream.* The counter consists of two sets (up and down) of scintillator hodoscopes, each of which has two plastic scintillators covered with lead plates in front of, in between and behind of them. Exploiting its good time resolution (< 1 ns), it is also used for the online monitoring of the beam bunch structure (e.g. timing shift, bunch length). The proton beam is monitored by the proton beam-gas events; the electron beam is

---

* Although C5 originally stands for the fifth collimator, it refers to the C5 counter in the following text.

monitored by the synchrotron radiation signals. Timing shift is recorded for a fine adjustment of the calorimeter timing to the beam crossing.

Chapter 4

Trigger and Offline Filter

4.1 General Requirements

The main task of the trigger and data-acquisition system is to detect the electron-proton collision events and record the detector signals for later physics analyses. The trigger decision has to be given for every 96 ns beam-crossing interval, which corresponds to a rate of 10 MHz. Although the detector signals are available for every beam-crossing, it is impossible to read out and record all of them. For example, the data storage rate is limited to about 5 Hz for a typical data size of 100 kbyte.

Nevertheless, this limit should not affect the event selection of most of physics processes of interest. Large-Q^2 processes or heavy quark production processes have small cross sections that give rates of less than 1 Hz at the nominal luminosity. For moderate Q^2 ($> 10\,\mathrm{GeV}^2$) NC-DIS, the event rate is still about 1 Hz. Inclusive photoproduction process has a very large cross section, which gives a very high rate even after requiring the scattered electron tagging or large transverse energy. Events of this class have to be correctly identified and thinned out to a proper fraction.

The background event rate from other sources than the electron-proton collision may go up to $\mathcal{O}(100\,\mathrm{kHz})$ mainly due to the proton beam-gas interaction. The proton beam-gas interaction is a collision between a beam-proton and a nucleus of the residual gas in the long straight-section of the proton beam-line. The scattered proton and the pieces of the broken nucleus produce a lot of energetic secondary particles by hitting the beampipe and other material around. In order that these secondary particles hit the inside of the main detector, the interaction point have to be upstream of the proton beam. This property is useful to reject the proton

beam-gas events.

The trigger system has to reduce the potential event rate of 100 kHz down to the data storage rate of 5 Hz without losing low-rate events under the beam-crossing rate of 10 MHz. Since it is difficult to gain such a large reduction factor at once, the event rate is reduced gradually by three levels of the trigger system. Fig. 4.1 shows a schematic diagram of the trigger and data acquisition system, which is described in the next section[31].

4.2   Trigger and Data Acquisition System

4.2.1   First Level Trigger

The first level trigger (FLT) is a hardware-based trigger system that makes the trigger decision for every beam-crossing[32, 33]. The trigger rate is designed to be less than 1 kHz, which makes it possible to read out all the detector signal. The decision is given in 46 steps ($4.4\,\mu$s) of synchronized pipeline to the beam-crossing. Meanwhile the detector signals are delayed in analog or digital pipelined buffers.

The first 26 steps are used by the local first level trigger (local-FLT) of each detector components. The detector signals are partially split and digitized by fast electronics. The digitized signals are further processed in each local-FLT, in order to provide the trigger data such as total and transverse energies of CAL, number of tracks in CTD or hit map of BMU. In total there are 700 bits of data from 11 detector components.

The remaining 20 steps are used by the global first level trigger (GFLT) to make the trigger decision. The trigger condition is divided into 64 sub-triggers, each of which can be individually disabled or scaled down to a given fraction. The sub-trigger condition is programmed in three steps of memory lookup table (MLT).

In every step of MLT, the number of trigger data bits is reduced by comparing the data to the energy threshold or by making a logical combination of the data. An MLT is a memory device that can convert any bit-pattern of data into any other pattern of data by reading the bit-patterns written into corresponding memory addresses. GFLT generates the bit-patterns online in order to make it possible to maintain the trigger condition in a simple database of logical expressions. Since values of the energy threshold, combinations of the data from different detector components and veto conditions are programmed in one place, it is easy to flexibly change and keep track of the trigger conditions.
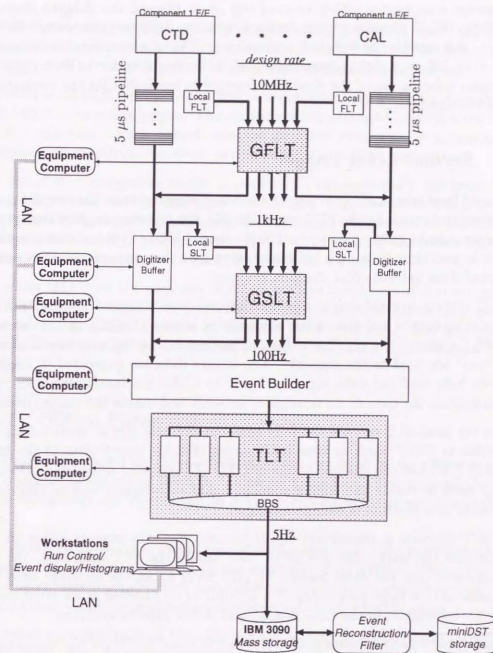

Figure 4.1: ZEUS trigger and data acquisition system. Description is given in text.

The trigger decision, as a logical-or of enabled sub-triggers, is transferred to all the detector components either to read out or to discard the delayed signals in the buffers. GFLT disables trigger decision until the detector components finish to read out, and records the duration as deadtime. The read-out time is designed to be less than $100\,\mu s$, which corresponds to $10\,\%$ deadtime under $1\,kHz$ trigger rate. Continuous information of the deadtime fraction is inevitable for the evaluation of the effective luminosity.

4.2.2 Second Level Trigger

The second level trigger (SLT) is a software-based trigger system that rejects most of the background events in the FLT output[34, 35]. By rejecting most of background, the trigger rate is reduced down to $100\,Hz$ from $1\,kHz$. This reduction makes it possible to gain time to build a combined event data from separately processed and transferred data until the SLT decision is given.

The SLT system is divided into the local second level trigger (local-SLT) of each detector components and the global second level trigger (GSLT), in the same way as the FLT system. The pipeline is formed by inter-connected processors, of which transputers[†] are used as the majority. The trigger data are generated in the local-SLT from fully read out data and transferred to GSLT via transputer links. Then GSLT combines the data in its transputer network and makes the trigger decision.

Because the local-SLT can use the fully read out detector signal, more information is available at GSLT, such as time information of CAL, coordinates of the energy clusters of CAL and the charged tracks of CTD. The parallel processing network of GSLT is used to divide the trigger condition into sub-triggers and to process the trigger-data in a pipeline of each sub-trigger.

The GSLT decision is transferred to all the detector components either to keep or to discard the data. For the event that fulfills the SLT condition, the data are transferred into the event builder (EVB). EVB packs the separate data from components into a large structured data format, to be handled as an event data in the third level trigger, in the data storage and in the physics analyses.

[†] Transputer is a parallel processing CPU produced by Inmos Inc. It has four transputer links (serial data-transfer lines) per CPU that makes it easy to construct a parallel processing network. GFLT also uses transputers for hardware control, MLT programming and data transfer to GSLT.

4.2.3 Third Level Trigger

The third level trigger (TLT) system is a so-called "computer farm" that classifies the events and that reduces the total event rate from $100\,Hz$ to $5\,Hz$. It has to accept $10\,Mbyte$ data per second and make a decision within $0.01\,s$ in average.

The farm of 30 RISC computers[‡], that were commercially available, provides about 1000 MIPS[*] computing power. The computers are arranged into six data branches of five computers. Each branch receives an event from the corresponding EVB interface, and distribute the event to one of the unoccupied computers.

The use of such computers makes it possible to run essentially the same software that are tested and used in the offline environment. The event selection is performed by reconstructing the events, rejecting the remaining background events, classifying the events and making the trigger decision. For each type of the interesting physics process, a filter algorithm is installed for event classification.

The event that does not pass any of filters are discarded even if it is not identified as a background event. The event that satisfies high rate filters only are scaled down to the pre-defined fraction to keep the low trigger rate. The selected events are transferred through the branch bus switch (BBS) to the IBM computer for data storage.

4.2.4 Offline Filter

The events that passed the three-level trigger are processed by the offline reconstruction program before using them in the physics analyses. The tasks of the process are to reconstruct the events and to perform further event selection called *offline filter*.

Prior to reconstructing the event, refined calibration is applied to improve the data by using the information that was not available at run-time. Then, the process performs various reconstruction tasks of noise suppression, cluster search, charged track finding, vertex reconstruction and electron/muon identification.

The event selection task of the offline filter is performed on these reconstructed events. The offline filter can be considered as the fourth level trigger, since physics analyses start from the events that passed the offline filter. In the following sections

---

[‡] Data station server 4D/35S from Silicon Graphics Inc., with R3000 RISC CPU. RISC stands for Reduced Instruction Set Chip.

[*] Million Instruction Per Second.

the offline filter is included in the term "trigger."

The task of the offline filter is the event classification in the same way as in TLT. For each type of the interesting physics process, a filter algorithm with a tighter selection criteria than in TLT is installed into the reconstruction program. Events are marked with corresponding flags if the selection criteria of the filters are satisfied. If the event passes any of the filters, the reconstructed data is stored in a huge disk space for convenient access to the data.

4.3 Trigger for NC-DIS

Selecting an NC-DIS event is equivalent to recognizing the scattered electron in the detector. In general the scattered electron is energetic and isolated from other particles, and therefore it is an easy task to identify the NC-DIS event. However, when the current jet is boosted toward the backward direction (x is small and y is large), the scattered electron can kinematically be less energetic and less isolated. Trigger conditions are divided into three steps. The first step is to pick up the events with large electromagnetic activity in CAL. The second step is to use a kinematic constraint that requires the electron to be inside CAL. The last step is to identify the scattered electron by searching a particular energy deposit pattern in CAL. In parallel, the events that are identified as background are rejected. In Table 4.1 the trigger conditions that are described in this and next sections are summarized.

4.3.1 FLT condition for NC-DIS

The FLT condition for NC-DIS is kept as simple as possible. Basically it only requires some energy in the EMC section of CAL, with which the scattered electron triggers over the whole solid angle except for the very forward region. The energy threshold is optimized in such a way that a higher energy threshold is set toward the forward direction in order to reduce the proton beam-gas background rate. This optimization does not affect the acceptance for NC-DIS since the scattered electron in the forward hemisphere is more energetic than the beam energy.

NC-DIS events are triggered by five sub-triggers that are named REMCth, REMC_E, BEMC_E, EMC_E and CAL_E. The REMCth sub-trigger, which picks up the smallest-Q^2 NC-DIS, requires more than 3.75 GeV of the coarse energy sum over entire RCAL EMC. The region of one ring of towers surrounding the beampipe (8 towers, ±30 cm square), which is called the RCAL *beampipe region*, is excluded from the energy sum

NC-DIS trigger conditions	
FLT	CAL_E(total energy) > 15 GeV
	EMC_E(EMC energy) > 10 GeV
	BEMC_E(BCAL EMC energy) > 3.4 GeV
	REMC_E(RCAL EMC energy) > 2 GeV
	REMCth(coarse RCAL EMC) > 3.75 GeV
TLT	
	$\delta_0 > 20$ GeV
Offline filter	
	$\delta_0 > 25$ GeV and electron finder

Background rejection conditions	
FLT	C5 beamgas-timing
SLT	CAL timing $|t_R| > 8$ ns
	$|t_F| > 8$ ns
	identified as the CAL PMT noise
TLT	CAL beampipe timing $|t_{BP}| > 8$ ns
	CAL timing $|t_R| > 8$ ns
	$|t_F| > 8$ ns
	$|t_F - t_R| > 8$ ns
	$|t_G| > 8$ ns
	identified as the CAL PMT noise
	identified as the cosmic ray muon event
	identified as the halo muon event
Offline filter	
	CAL timing $|t_R| > 6$ ns
	$|t_F| > 8$ ns
	$|t_F - t_R| > 8$ ns
	$|t_G| > 8$ ns
	identified as the cosmic ray muon event

Table 4.1: Trigger conditions for NC DIS. Events are saved if one of the trigger condition and none of the rejection condition are satisfied at each level of trigger.

of the other sub-triggers since it is the most noisy region due to the proton beam-gas background. Other noisy regions, the FCAL *inner region* of three rings of towers surrounding the beampipe (± 70 cm square) and entire RCAL HAC are not used in the energy sum of these sub-triggers, either.

The other sub-triggers cover the remaining solid angle. REMC_E sub-trigger requires more than 2 GeV in RCAL EMC excluding the beampipe region; BEMC_E sub-trigger requires more than 3.4 GeV in BCAL EMC. For the events with the scattered electron in FCAL or around the calorimeter boundaries, EMC_E sub-trigger requires more than 10 GeV in the entire EMC, again excluding the RCAL beampipe region and the FCAL inner region. The events with large-Q^2 are also triggered complementarily with the energetic current jet, by CAL_E sub-trigger which requires more than 15 GeV in CAL except for the noisy regions. The energy threshold values are chosen to have large margins.

With this set of sub-triggers, NC-DIS events are picked up almost perfectly. It is checked with the trigger simulation program on the Monte Carlo events that the FLT efficiency does not affect the overall acceptance. If the events are limited to those of the final event sample (see Chapter 7), the fraction of events that do not pass the FLT condition is less than 0.05 % and all of these events have small-Q^2 ($< 30 \,\mathrm{GeV}^2$). The efficiency for the entire Monte Carlo events of $Q^2 > 7 \,\mathrm{GeV}^2$[§] is 99.4 %. Even if 50 % higher threshold values are used for all sub-triggers in the trigger simulation, the resulting FLT efficiency is still 99.7 % and the lost events are all in the small-Q^2 region.

A typical FLT rate was around 200 Hz with a typically about 10 % deadtime fraction during the 1993 run period, including the other sub-triggers. The effective FLT rate was limited around 200 Hz since the deadtime fraction increased rapidly above this. The FLT rate is highly dependent on the beam condition, that changes the rate of the proton beam-gas background.

4.3.2 Selection with Kinematic Constraint

In the NC-DIS event with the scattered electron in CAL, a useful kinematical constraint is built by using that the momenta of particles ideally escape only through the forward beampipe hole. Considering that the energy and the longitudinal momentum are essentially the same for the escaping particles, the measured difference

---

§ $7 \,\mathrm{GeV}^2$ is the smallest-Q^2 boundary of this F_2 measurement.

$E = E_e + E_p = E_e{}' + E_{rem} + E_{had}$
$p_Z = -E_e + E_p = E_e{}'\cos\theta + E_{rem} + E_{had}\cos\gamma$
$\delta = \Sigma\, E_i(1\text{-}\cos\theta_i) = 2E_e$

$E = E_e + E_p = (E_e{}') + E_{rem} + \Sigma E_i$
$p_Z = -E_e + E_p = (-E_e{}') + E_{rem} + \Sigma E_i\cos\theta_i$
$\delta = \Sigma\, E_i(1\text{-}\cos\theta_i) = 2(E_e - E_e{}') = 2E_\gamma$
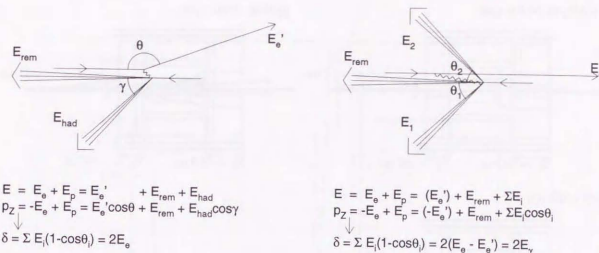
Figure 4.2: A schematic description of the δ constraint. The ideal value of δ for NC-DIS (left) is $2E_e$ while it is $2E_\gamma$ for photoproduction (right) since E_e' of the escaped electron is not measured.

between them is a good quantity. The quantity δ is defined by

$$\delta \equiv \sum_i (E_i - (p_Z)_i) = \sum_i E_i(1 - \cos\theta_i), \qquad (4.1)$$

where the sum is taken over all the measured energies and angles in CAL. Then, as shown in Fig. 4.2, δ becomes twice the electron beam energy ($2E_e = 53.4 \,\mathrm{GeV}$) for NC-DIS, while it becomes twice the energy of the exchanged photon ($2E_\gamma$) for photoproduction.

Since the cross section of the photoproduction process falls down for large E_γ, most of the photoproduction background events are removed by rejecting the events with small δ. The good point of this selection criterion is that it does not require the scattered electron identification, which is usually a more difficult task.

There are a couple of sources that degrades δ of NC-DIS. The major source is the initial state radiation, since the radiated photon from the beam electron escapes into the rear beampipe hole. The missing energy degrades δ unless the photon is detected by the LUMI γ-calorimeter and recovered by adding twice the measured photon energy to δ. The escaping muons and neutrinos or slowed down hadrons are also the sources of degrading δ. The energy resolution and the uncertainty of the event vertex position are the sources that smear the value of δ.

Good timing

electron beam-gas

$t_{C5} \sim +11\,\mathrm{ns}$

$\bar{t}_F = \pm 0\,\mathrm{ns}$ $\bar{t}_R = \pm 0\,\mathrm{ns}$

Beamgas timing

proton beam-gas

$t_{C5} \sim -11\,\mathrm{ns}$

$\bar{t}_F = \pm 0\,\mathrm{ns}$ $\bar{t}_R \sim -10\,\mathrm{ns}$

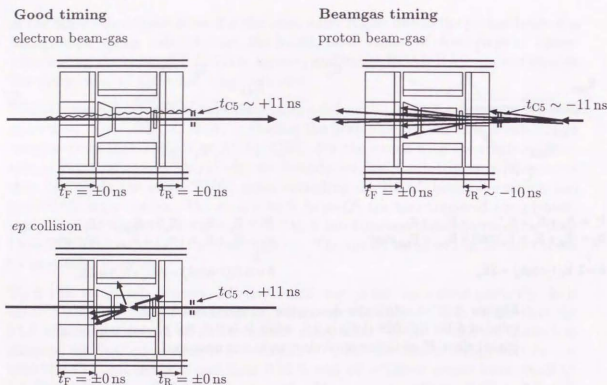*ep* collision

$t_{C5} \sim +11\,\mathrm{ns}$

$\bar{t}_F = \pm 0\,\mathrm{ns}$ $\bar{t}_R = \pm 0\,\mathrm{ns}$

Figure 4.3: Principle of the beam-gas rejection by timing.

In TLT and the offline filter δ is calculated with CAL and LUMI γ-calorimeter, assuming the event vertex at the nominal interaction point. The value is obtained by

$$\delta_0 = \sum_{i \text{ in CAL}} E_i(1 - \cos\theta_i) + 2E_{\mathrm{LUMI}\gamma}, \qquad (4.2)$$

where δ_0 denotes this quantity at the trigger level, E_i and θ_i are the energy and angle of each CAL cell. TLT requires δ_0 to be greater than $20\,\mathrm{GeV}$; the offline filter requires δ_0 to be greater than $25\,\mathrm{GeV}$.

4.3.3 Electron Finding

Even after the selection with δ, a large fraction of the photoproduction background remains in the data. The amount of the photoproduction background is as many as half of the events if $\delta > 25\,\mathrm{GeV}$ is required. In order to remove these photoproduction events, it is necessary to identify the scattered electron. The offline filter makes
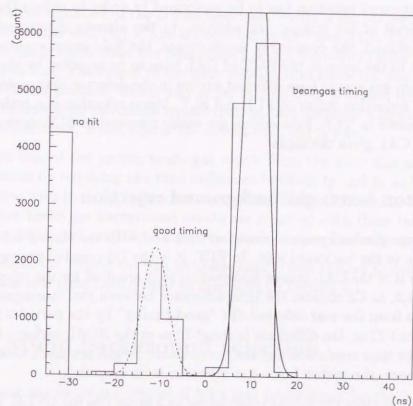
Figure 4.4: C5 timing distribution at FLT (direction of time is reversed).

use of electron finding algorithms, all of which look for a particular energy deposit pattern in CAL.

Since none of the electron finding algorithm is perfect, or at least superset of others, four different algorithms are used to complement each other. The electron energy is required to be more than $4\,\mathrm{GeV}$, considering that a cut at $5\,\mathrm{GeV}$ is finally applied in the standard scattered electron identification. The event is discarded if none of the algorithms find the scattered electron.

4.4 Background Rejection at the Trigger Level

Dedicated background rejection has to be performed in order to reduce the trigger rate at every level of the trigger. In addition to the already mentioned proton beam-gas background, the cosmic-ray muon events, the halo-muon events and the fake events due to the noise in the PMT of CAL have to be removed by the trigger. The proton beam-gas events have different timing in the detector that makes it easy to gain a large reduction factor in FLT and SLT. Muon rejection is a rather heavy task that is applied in TLT. Fake events are easily removed in SLT since only one PMT of entire CAL gives the signal.

4.4.1 Proton beam-gas background rejection

The proton beam-gas background events are removed with the timing information of the detectors in the backward side. In FLT, it is the C5 counter timing; in SLT and later levels it is the CAL timing information that are used for the rejection. As shown in Fig. 4.3, at C5 counter the time difference between the "beamgas-timing" by the particles from the rear side and the "good-timing" by the particles from the front side is about 22 ns; the difference is about 10 ns at the RCAL surface. Provided that the detector time resolution and the beam-bunch length are much smaller than the time difference, the proton beam-gas rejection is an easy task.

The C5 counter provides the timing information in 5 ns unit to the GFLT. The good separation of the "beamgas-timing" and the "good-timing" is shown in Fig. 4.4, in which the large "good-timing" peak is due to the synchrotron radiation of the electron beam. Since most of the proton beam-gas events have particles hitting the C5 counter, vetoing the events with negative timing gives a large reduction factor of 2 to 5 for REMCth sub-trigger. The C5 timing veto is applied for all enabled GFLT sub-triggers. The chance coincidence rate was smaller than 0.1 % even in the worst beam condition case of the 1993 run period.

The CAL timing information is provided for each part of the calorimeter. The RCAL time (t_R) is the averaged time over RCAL, the FCAL time (t_F) is that over FCAL and so on. Time from each PMT is adjusted to zero for the particles from the nominal interaction point. When calculating the average, proper energy cut and weighting are required since the time resolution becomes very poor for small energy PMT signals. The higher the energy cut threshold is, the more reliable the timing information is, in exchange of the smaller chance to obtain the timing. Therefore, timing is calculated with more conservative cut in SLT than in TLT. Another choice

of the timing information is the beampipe time (t_{BP}) that uses only the PMT's in the beampipe region to reduce the number of PMT's included in the timing calculation.

The essential signature of the proton beam-gas events is the earlier RCAL time than zero. The events with $|t_R| > 8$ ns are rejected by SLT and TLT. This time window is not sufficiently tight, since the beam-bunch width convoluted with the resolution is as small as 2 ns. The reason of the wide window is to allow the timing fluctuation of the true beam position, which may differ by 1 ns from provided HERA clock. This shift is recovered by the offline reconstruction, and therefore a tighter cut is applied in the offline filter, which rejects the events with $|t_R| > 6$ ns.

Some fraction of the proton beam-gas events from the later side of the bunch tail are removed by requiring the time difference between t_F and t_R to be around zero. The events with $|t_F - t_R| > 8$ ns are rejected by TLT. As shown in Fig. 4.5, most of the proton beam-gas background events are removed with these two conditions by TLT. An additional condition of $|t_{BP}| > 8$ ns is complementarily applied at TLT.

For NC-DIS, the timing cut can be made much more tighter to completely remove the proton beam-gas background as discussed in Section 7.1.

4.5 Muon background rejection

The cosmic ray muon is a source of high rate background for the large-scale ZEUS detector. The muons hit BMU and deposit energy in CAL. The event rate was about 50 Hz for the FLT condition of the 1993 run period. Therefore it is the second largest background that has to be removed by the trigger.

One simple way to reduce the trigger rate is to put a time window. This is useful for background reduction of all kinds that are not associated with the beam. A reduction factor of about two is gained by FLT just by disabling the trigger for most empty bunches that are not filled by either beam. An additional reduction factor of about six is gained by SLT and TLT by putting the same kind of ±8 ns time window that was used for the proton beam-gas rejection. SLT applies the time window for t_F and t_R; TLT applies it for the global CAL time (t_G) in addition.

For the remaining about 5 Hz of muons, a muon-finding algorithm is applied to look for a certain energy deposit pattern in the CAL cells. A cosmic ray muon leaves an approximately straight line trajectory in four dimensions (t, X, Y, Z) of space-time. A straight line fit in the Y-t plane picks up the candidate of the falling down muon from the sky, and an additional fit in the X-Y-Z space ensures the muon trajectory.
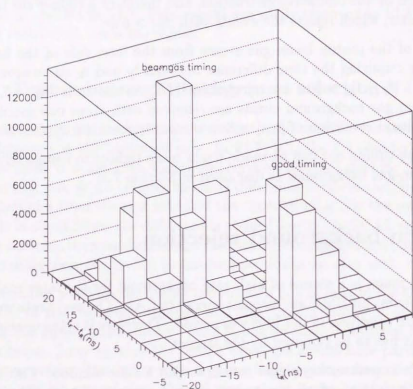
Figure 4.5: RCAL event time versus event time difference between F/RCAL at TLT.

In order not to reject the muons from the beam collision, no CTD track must be associated and all the energy must belong to the muon trajectory. This algorithm is applied by TLT and by the offline filter to reject the cosmic-ray muon events.

Another muon background source is the *halo muon*, which is the decay muon of π or K in the secondary particles of the proton beam halo. The halo muons travel through the detector in parallel to the beam, with a trigger rate of about 1 Hz. Again, a straight line fit in the Z-t plane and the variation in the X-Y plane are examined to identify the halo muons. This algorithm is applied by TLT to reject almost all the halo muon events.

Chapter 5

Monte Carlo Simulation

The measured quantities are filtered in many steps. From the sub-process of interest, the particles may decay before entering the detector, the detector may distort the particle properties when converting into the detector signals and the trigger condition or the additional artificial cuts may bias the acceptance. These effects are usually corrected by using Monte Carlo simulation. Given a model of the sub-process, the event is generated to fulfill the model with the Monte Carlo method. The final state particles are fed into a detector and trigger simulation program, which is tuned to reproduce the response of the real detector. Then, the Monte Carlo events obtained by the detector and trigger simulation program can be compared to the real data. The Monte Carlo events are further processed through the same analysis chain of the event reconstruction and the event selection, in order to make a comparison with the purified real data. The results of the comparisons are used to extract the true quantities of the sub-process.

5.1 Event Generation

The lowest order sub-process of NC-DIS has no theoretical uncertainty except for the structure functions (see Eq.2.11). The input structure function of the event generation can in general be arbitrary, but the structure function is preferable to be close to the true one. In this analysis, the MRS D'_ parametrization, which is close to the previous result of the 1992 fall run period[1], is chosen (see Section 2.4 for the details of this parametrization). The choice is not essential since a different structure function is easily simulated afterwards, by using the known scattered parton flavor

and the ratio of the parton densities of two different structure function sets.

In order to generate realistic NC-DIS Monte Carlo events, higher order corrections to the sub-process have to be taken into account. The electron side is corrected for the QED photon radiation of the initial and final state. The proton side is more complicated since the gluon radiation has a larger coupling constant and the radiated gluons have to be finally neutralized to hadrons. The gluon radiation correction to the inclusive cross section is already absorbed in the structure functions, but the fragmentation of the scattered parton and the proton remnant into multiple hadrons has to be calculated with a model assumption. If the parton has more than a few GeV cut-off momentum, the fragmentation can be treated by a QCD based parton shower model. The final fragmentation and hadronization that happen below the cut-off can only be treated by a phenomenological model. The program used for generating events is a combined program of separate programs for the QED radiative correction, the parton shower and the fragmentation.

The sub-process generation including the radiative correction is performed by HER-ACLES 4.4[36] program, which includes $\mathcal{O}(\alpha)$ corrections of the initial and final state radiation. For the proton side of the sub-process, all the inclusive effects that are included in the parton distribution are automatically imposed, and the other inclusive effects are included as the F_L correction.

The parton shower is performed by the color-dipole model combined with the boson-gluon fusion (CDM+BGF) as implemented in ARIADNE 3.1[37] program. The CDM is a model in which gluons are radiated from two poles of the scattered quark and the remnant di-quark. In this model the boson-gluon fusion type of NC-DIS is not simulated and thus it has to be combined as an additional sub-process. The CDM+BGF model is known to reproduce the hadronic energy flow at HERA energy[38]. Another choice of the parton shower model is the ME+PS as implemented in LEPTO 6.1[39] program, which also reproduces the hadronic energy flow quite well. In this model the matrix elements of the $\mathcal{O}(\alpha_s)$ diagrams are exactly calculated and the higher order corrections are performed in a bremsstrahlung-like gluon emission model. The CDM+BGF or ME+PS parton shower is connected to the fragmentation program of the Lund string model implemented in JETSET 7.3[40] program to obtain the hadron final state.

With this combined program, 300k NC-DIS events with CDM+BGF are generated for the $Q^2 > 4\,\mathrm{GeV}^2$ region. This corresponds to $750\,\mathrm{nb}^{-1}$, or 1.5 times more luminosity than the real data. The small-Q^2 boundary at $4\,\mathrm{GeV}^2$ is chosen due to several reasons; this is below the the acceptance limit except for the very small-x ($< 10^{-4}$) region, the cross section becomes too large for the available computing

power to generate sufficient amount of events at small-Q^2 and the MRS D$'_-$ parton distribution is defined only in $Q^2 > 4\,\text{GeV}^2$. In addition, 200k events with ME+PS are generated for cross-check.

5.2 Detector and Trigger Simulation

The detector simulation is performed by GEANT 3.13[41] program with an accurate modeling of the ZEUS detector[42]. Particles are traced for their decay, energy loss and multiple scattering in the program. The detector signals are obtained from the energy loss in the detector material and are tuned to reproduce the test beam results. It is important to construct an accurate model of the dead material such as the beampipe, the detector frames and the cables. Additional artificial noise signals are added in order to simulate the real detector signal.

FLT and SLT conditions are implemented in hardware or in transputers, and thus it is necessary to prepare separate programs to simulate the trigger decisions[43]. The internal structure of the trigger simulation program is also separated into FLT and SLT, and each of them is further separated into the local-triggers and the global trigger. For example the GFLT simulation is performed in a program that is generated from the same database for the real use of the MLT programming[44]. TLT simulation is performed in a program that is transplanted back to the offline environment in order to be able to use for the trigger simulation[45].

Chapter 6

Kinematics reconstruction

The kinematic variables x, Q^2 that determine the kinematics of NC-DIS are reconstructed by using the double-angle method (Eq.2.30) as the standard method with ZEUS[1, 29]. This is because the scattered electron angle or the hadron angle (Eq.2.29) measured with CAL have better kinematics resolution than other quantities such as the electron energy and the momentum components of the hadron system. What is more crucial is to correctly identify the scattered electron, since otherwise the reconstruction of kinematics is meaningless. In this chapter, the electron identification method and the measurement of various quantities are described, then the performances are studied and comparisons are made between different kinematics reconstruction methods.

6.1 Electron identification

The scattered electron is identified by an algorithm that searches the electromagnetic shower cluster in CAL[46]. The essential quantities used to separate an electromagnetic cluster from hadronic shower clusters are the shower sizes in the depth and transverse directions. Isolation of the cluster is an additional useful requirement for the scattered electron identification.

An electromagnetic shower extends over CAL cells, that have to be combined into a single cluster. Prior to combining cells, all the energetic cells are projected onto a spherical surface, whose center is at the event vertex, for easier treatment of the calorimeter boundaries. All the cell distances are treated in terms of the cone radius in angle space, and thus the algorithm is referred to as the "cone algorithm." Every

energetic EMC cells is regarded as the seed cell of the electromagnetic cluster, if the energy is greater than 1 GeV and it is the highest energy cell within the cone of 250 mrad radius. In other words, cells within the cone are combined into a single cluster around the seed cell. These clusters are the electron candidates to start with.[†]

The parametrization for the electron identification is based on the quantities defined in two cones (inner and outer) for each of EMC, HAC1 and HAC2. The center of the cones is at the center of the seed cell. The inner cone is the region within the radius of 250 mrad for EMC and 300 mrad for HAC1/HAC2; the outer cone is outside the inner cone and within the radius of 400 mrad for EMC and 500 mrad for HAC1/HAC2. With these definitions, the isolated electron deposits most of the energy within the EMC inner cone. On the other hand, the energy deposit in the outer HAC cone is not likely by the electron, and therefore the candidates that have more than 1 % energy fraction in the outer HAC cones are discarded. The energy weighted radius in the EMC inner cone represents the transverse shower size of the cluster and gives a probability to be an electron. The probability is obtained from the distribution of this quantity measured with the electron test beam. If the probability is less than 0.1 %, the candidate is discarded from the list. Similarly, the energy fraction in the EMC outer cone represents the isolation; the energy fractions in the HAC1 and HAC2 inner cones represent the shower depth. The probabilities are calculated in the same way, and then the candidates with less than 0.1 % probabilities are discarded. The energy imbalance between two PMT's of the seed cell, which reflects the horizontal impact position of the electron, is included in the depth probability calculation since the energy leakage into the HAC cells becomes relatively large around the module boundary. The overall probability is calculated as a geometric mean of these four (three for RCAL) probabilities and the candidates are discarded if the probability is less than 3 % (0.3 % for RCAL). The energy sum of the inner and outer cones gives the electron energy.

This algorithm usually finds only one energetic candidates in CAL. In about 5 % of NC-DIS events the second candidate is found and the third candidate is found only in 0.1 % of events. If more than one candidates are found, the highest probability candidate is taken to be the scattered electron.

The performance of the electron identification algorithm is studied in terms of ef-

---

[†] Definition of the EMC cell is slightly altered for electron finding. In the case that the scattered electron hits a HAC0 cell directly or a neighbor cell of HAC0, or in other words if the seed cell is in FCAL or RCAL, the HAC0 cells are treated as the EMC cells. The top five HAC1 cells of the RCAL module 12 are treated as the EMC cells since the EMC cells are missing in front of them due to the cooling pipe of the solenoid.
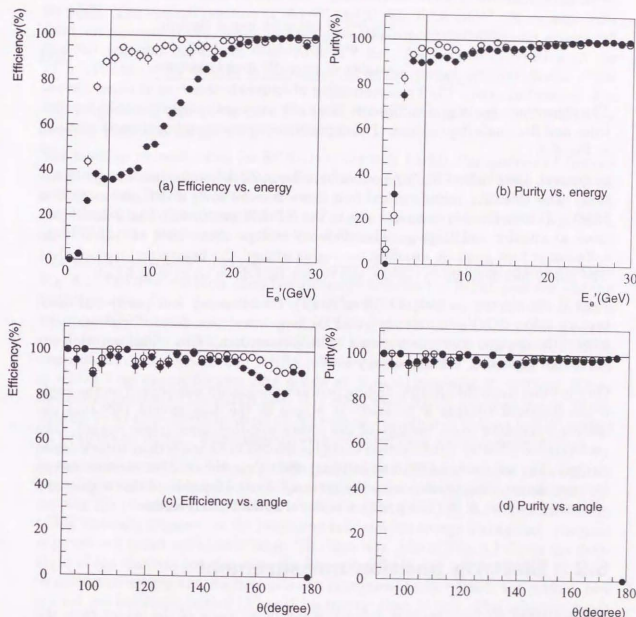
Figure 6.1: Electron finding performance on the Monte Carlo NC-DIS sample: (a), (b) The efficiency and the purity of the NC-DIS electrons of $Q^2 > 7\,\mathrm{GeV}^2$ without (close circle) and with (open circle) an angle cut $\theta < 150°$ as functions of the electron energy. The line indicates the 5 GeV energy cut. (c), (d) The efficiency and the purity of the NC-DIS electrons of $E'_e > 5\,\mathrm{GeV}$ (close circle) and $E'_e > 10\,\mathrm{GeV}$ (open circle) as functions of the scattered electron angle.

ficiency and purity. These quantities are defined by using the Monte Carlo events as:

$$\text{efficiency} = \frac{\text{number of correctly found electron}}{\text{number of true electron}}$$
$$\text{purity} = \frac{\text{number of correctly found electron}}{\text{number of found electron}}.$$

(6.1)

The algorithm should give sufficiently large efficiency and purity for energetic electrons and flat angle dependence. The dependence on the energy and angle is shown in Fig. 6.1.

In general, the electron finding performance becomes worse for less energetic electron. The efficiency (close circles) falls down from $\sim 95\,\%$ at $20\,\text{GeV}$ to $40\,\%$ at $5\,\text{GeV}$. This inefficiency is mainly due to the NC-DIS events with less isolated electrons at small-x and large-y. The efficiency is kept above $80\,\%$ at $5\,\text{GeV}$ if the isolation is kept good by avoiding the region around the beampipe (open circles). The purity less depends on energy, and it only falls down to $85\,\%$ at $5\,\text{GeV}$.

Even if the electron is isolated (open circle), the efficiency and purity fall down rapidly below $5\,\text{GeV}$. In order to avoid the large correction factor for a small efficiency, the electron energy is required to be greater than $5\,\text{GeV}$. This selection cut is referred to as the "electron energy cut."

On the other hand the electron finding performance should not depend on the angle if the scattered electron is isolated. It is seen as the dips around $165°$ that the efficiency becomes worse because of the poorer isolation there (close circles). The performance is better if the electron energy is limited to be more than $10\,\text{GeV}$ (open circles). The rise around $170°$ is an artificial effect since the smallest electron energy becomes larger than $5\,\text{GeV}$ under the given Q^2 limit. Outside of this region, the efficiency is about $95\,\%$. The purity is better than $95\,\%$ everywhere.

6.2 Electron position measurement

The scattered electron angle is defined as the polar angle of the vector from the event vertex to the electron impact point at CAL.[‡]

Practically, the impact point is replaced by the electron position, defined as the electromagnetic shower center in CAL. The electron position is obtained in the 3×3

[‡] The effect of the magnetic field is neglected, since it affects only the azimuthal angle at the lowest order.

cells around the maximum energy cell, separately for vertical and horizontal directions[48]. The vertical position (Y for FCAL/RCAL, Z for BCAL) is reconstructed from the amount of the energy leakage, from the row of the maximum energy cell into the adjacent upper and lower rows of cells. The horizontal position (X for FCAL/RCAL, ϕ for BCAL) is reconstructed as the energy weighted mean of the shower center in each cell, which is obtained from the PMT energy imbalance. The amount of the energy leakage and the PMT energy imbalance are converted to the position quantities by parametrized functions.

The position reconstruction for RCAL is tuned with RHES. Parametrized functions are fitted to the accurate RHES position of the real NC-DIS data. With $3\,\text{cm} \times 3\,\text{cm}$ segmentation, RHES gives $6\,\text{mm}$ electron position resolution, which is much better than that of CAL. The fitting result is self-checked by using the real data. For FCAL and BCAL, the parameters are fitted to the test beam results.

The reconstructed CAL position has good position resolution for RCAL as shown in Fig. 6.2. The first two plots show the difference between the RCAL position and the RHES position for X (a) and for Y (b). The RCAL position resolution combined with the RHES resolution is obtained to be $1.3\,\text{cm}$ for X and $0.9\,\text{cm}$ for Y. The position resolution is stable over RCAL as shown in the last two plots. Position dependence of the RCAL and RHES position difference for X (c) and for Y (d) is within $1\,\text{cm}$ except for two data points at $X \sim -12\,\text{cm}$ and $X \sim 70\,\text{cm}$. These deviations are due to the RHES boundary effect since RHES was read out in RCAL module 11 to 15 ($-30\,\text{cm}$ to $70\,\text{cm}$ in X) with an exception of bottom half of module 12 ($-10\,\text{cm}$ to $10\,\text{cm}$). These regions were excluded from the parameter fitting.

In the region around the beampipe hole, the position reconstruction is more difficult since the amount of energy leakage into the beampipe side cannot be measured. Especially the position reconstruction becomes impossible when the maximum energy cell is vertically adjacent to the beampipe hole and the energy leakage into the next adjacent cell is not sufficiently large. The first two plots of Fig. 6.3 shows the deviation of the electron position near the beampipe for X (a) and for Y (b). In order to avoid this region, the electron position is required to be outside the $\pm 16\,\text{cm}$ box around the beampipe (either $|X|$ or $|Y|$ is greater than $16\,\text{cm}$). This selection cut is referred to as the "box cut" at $16\,\text{cm}$. The box cut is already applied in Fig. 6.2.

The comparison between data and Monte Carlo is shown in Fig. 6.3-(c) in terms of the resolution of the radius ($R = \sqrt{X^2 + Y^2}$). The data position is compared with RHES, while the Monte Carlo position is compared with the generated impact point. The Monte Carlo histogram is smeared with $6\,\text{mm}$ gaussian for the missing contribution from RHES resolution. The comparison of the scattered angle between
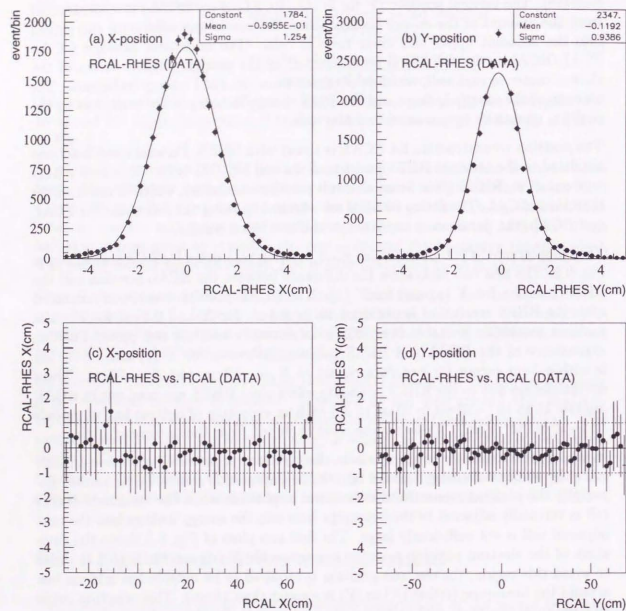
Figure 6.2: Electron position resolution as comparisons with RHES: (a), (b) The overall X- and Y-position differences between RCAL and RHES. (c), (d) The position dependence of the X- and Y-position differences between RCAL and RHES.

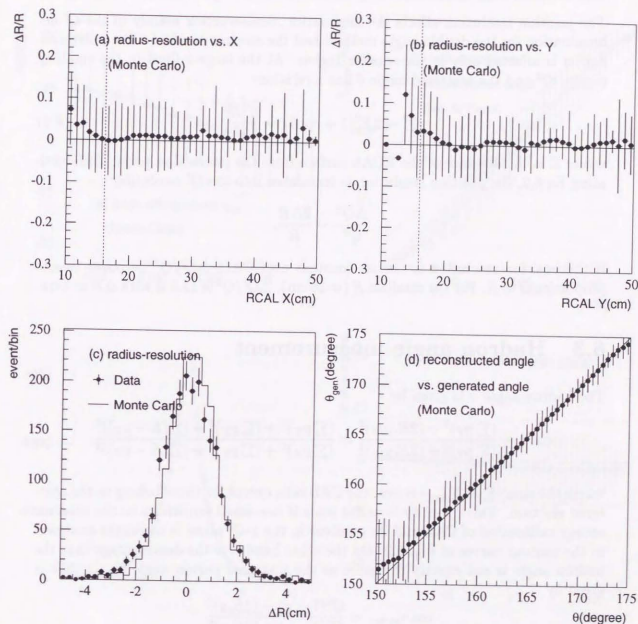**Figure 6.3:** Electron position resolution checks with Monte Carlo: (a), (b) The X- and Y-position dependence of the radius resolution to see the boundary effect at the beampipe hole. (c) The radius resolution of data (obtained with RHES) and Monte Carlo (true resolution). (d) A comparison between the angle from RCAL and the generated electron angle.

that obtained from RCAL and the generated electron angle is shown in Fig. 6.3-(d).

The position resolution affects the kinematics reconstruction mainly in the Q^2 determination for the double-angle method and the electron method. The x determination is affected only in the small-x region. At the large-x limit in the small-Q^2 region, Q^2 and the scattered angle θ has a relation:

$$Q^2 \sim 2E_e^2(1 + \cos\theta) \sim \frac{E_e^2 R^2}{Z^2} \tag{6.2}$$

where Z is the distance of the RCAL surface from the interaction point. Differentiating Eq.6.2, the position resolution is translated into the Q^2 resolution:

$$\frac{\Delta Q^2}{Q^2} \sim \frac{2\Delta R}{R}.$$

If the position resolution is almost constant over CAL, $\Delta Q^2/Q^2$ becomes inverse proportional to R. For the smallest R (= 16 cm), $\Delta Q^2/Q^2$ is 12.5 % with $\Delta R = 1$ cm.

6.3   Hadron angle measurement

The hadron angle γ is given by

$$\cos\gamma = \frac{(\sum p_T)^2 - (2E_e y_{\mathrm{JB}})^2}{(\sum p_T)^2 + (2E_e y_{\mathrm{JB}})^2} = \frac{(\sum p_X)^2 + (\sum p_Y)^2 - (\sum(E - p_Z))^2}{(\sum p_X)^2 + (\sum p_Y)^2 + (\sum(E - p_Z))^2}.$$

where the sum ($\sum \equiv \sum_{\mathrm{had}}$) is over the CAL cells except for those belong to the scattered electron. This quantity is useful since it has small sensitivity to the absolute energy calibration of CAL and its gradient in the x-Q^2 plane is moderate as shown in the contour curves of Fig. 2.2. On the other hand it is the disadvantage that the hadron angle is not exactly the same as the scattered parton angle γ_{parton} that is given by

$$\cos\gamma_{\mathrm{parton}} = \frac{Q^2(1 - y) - (2E_e y)^2}{Q^2(1 - y) + (2E_e y)^2}$$

because of the parton fragmentation and the artificial effect by the uranium noise.

In order to suppress the uranium noise, cells with as small energy as noise are excluded from sum. The threshold is set to 4 r.m.s. of the noise distribution, which corresponds to 60 MeV for EMC, 100 MeV for HAC0 and 110 MeV for HAC1/HAC2 cells. Even after this noise suppression, the hadron angle is affected by the remaining
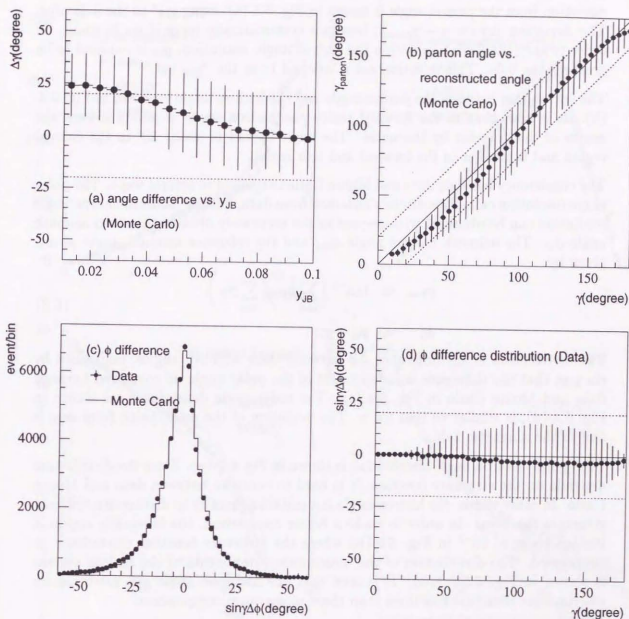
68

Figure 6.4: Hadron angle resolution: (a) The γ resolution as a function of y_{JB}. (b) The correlation between parton angle and the hadron angle. (c) The ϕ resolution as the measure of the comparison between data and Monte Carlo. (d) The polar angle dependence of the ϕ resolution. electron angle.

69

noise if the total hadronic activity is small. The hadronic activity dependence of the deviation from the parton angle is shown in Fig. 6.4-(a), using y_{JB}* as the indicator. The deviation $\Delta\gamma$ ($\equiv \gamma - \gamma_{\text{parton}}$) becomes systematically large if y_{JB} is small. In order to keep the deviation within the hadron angle resolution, y_{JB} is required to be greater than 0.04. This selection cut is referred to as the "y_{JB} cut."

The correlation between the parton angle and the hadron angle is shown in Fig. 6.4-(b). It is seen that in the forward region the hadron angle is pulled toward the center of the detector by the noise. The angle spread is about 20° in the central region and is smaller in the forward and rear region.

The consistency between data and Monte Carlo is checked in several ways. The polar angle resolution cannot be directly obtained from data, but the azimuth hadron angle resolution can be obtained with respect to the accurately obtained electron azimuth angle ϕ_{el}. The azimuth hadron angle ϕ_{had} and the reference azimuth angle ϕ_0 are given by:

$$
\phi_{\text{had}} \equiv \tan^{-1}\left(\sum_{\text{had}} p_Y \Big/ \sum_{\text{had}} p_X\right)
$$

$$
\phi_0 \equiv \phi_{\text{el}} + \pi. \tag{6.3}
$$

The distribution of the difference $\Delta\phi$ between these azimuth angles, multiplied by $\sin\gamma$ so that the difference is independent of the polar angle, is compared between data and Monte Carlo in Fig. 6.4-(c). The polar angle dependence, as shown in Fig. 6.4-(d), is similar to that for γ. The deviation of the mean value from zero is due to the magnetic field.

The (polar) hadron angle distribution is shown in Fig. 6.5-(a). Since the distribution depends on the structure function, it is hard to compare between data and Monte Carlo. In other words, the hadron angle is a suitable quantity to distinguish different structure functions. In order to make a better comparison, the kinematic region is limited to $x > 10^{-3}$ in Fig. 6.5-(b) where the structure function dependence is suppressed. The distribution of the momentum components of the hadron system is shown in Fig. 6.5-(c),(d). It is seen that the hadronic angle can more clearly discriminate structure functions than these momentum components.

---

* y obtained with the Jacquet-Blondel method as in Eq.2.28: $y_{JB} = \sum_{\text{had}}(E_i - (p_Z)_i)/2E_e$.
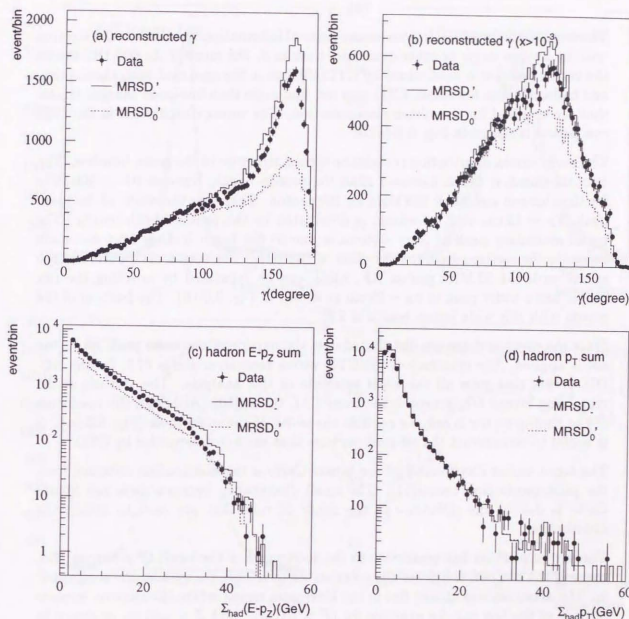
Figure 6.5: Hadron angle distribution: (a),(b) Hadron angle distributions of data and Monte Carlo with two different structure functions MRS D'_ and MRS D'$_0$($x > 10^{-3}$ for (b)). (c) $\sum_{\text{had}}(E - p_Z)$ distributions. (d) $\sum_{\text{had}} p_T$ distributions.

6.4 Event vertex

The event vertex position is a necessary piece of information to calculate the electron and the hadron angle or other quantities such as δ. For most of the NC-DIS events the vertex position is determined by CTD[49], but in the case that both the electron and hadron angles are small, CTD may not find more than one good charged tracks, that are required for the vertex reconstruction. The vertex distribution in the 1993 run period is shown in Fig. 6.6-(a).

The event vertex distribution reveals the spread structure of the beam bunches. The electron bunch is much narrower than the proton bunch, because RF is 500 MHz for the electron and 52 or 208 MHz for the proton. Therefore the width of the main peak, $\sigma_Z \sim 12$ cm at $Z \sim -5$ cm, is dominated by the proton bunch length. The broad secondary peak at $Z \sim +65$ cm is due to the beam leakage from the main bunch to the earlier adjacent RF bucket of 208 MHz. The vertex distribution of the events with the 52 MHz proton RF, which can be separated by selecting the run range, has a wider peak of $\sigma_Z \sim 25$ cm as shown in Fig. 6.6-(b). The fraction of the events with this wide bunch length is 7 %.

Since the event vertices are distributed over the outside of the main peak, no vertex cut is applied. The efficiency of the CTD vertex reconstruction is 97 % for the NC-DIS events that pass all the event selection of this analysis. The vertices of the remaining events are reconstructed from CAL timing[50]. Although the resolution of the timing vertex is only as good as the width of the main peak (Fig. 6.6-(c)), it is useful to reconstruct the off-peak vertices that are not determined by CTD.

The input vertex distribution of the Monte Carlo is the distribution obtained from the photoproduction events[51]. The small discrepancy between data and Monte Carlo is due to the difference in the range of runs that are used to obtain the distribution.

The vertex position has sensitivity to the acceptance of the small-Q^2 electrons. Because of the box cut, the closer the event vertex to RCAL, the smaller the acceptance is. The acceptance is almost flat in the kinematic region where the electron impacts outside of the box cut, for example for $Q^2 > 10 \, \text{GeV}^2$ and $Z > -40$ cm as shown in Fig. 6.6-(d). On the other hand, the vertex position resolution has little sensitivity to the kinematic variables. Since the CTD vertex resolution is less than 1 mm, the error contribution to the angle determination is negligible. Even if the CTD vertex is not found, the timing vertex resolution of 12 cm is only as bad as the electron position resolution for the small angle electrons.
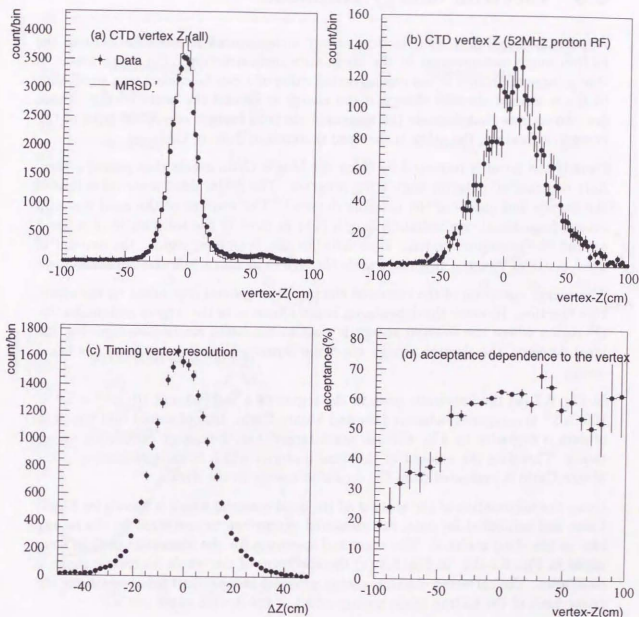

Figure 6.6: Event vertex distribution: (a) CTD event vertex Z position distribution for data and Monte Carlo. (b) CTD event vertex Z position distribution only for data of the 52 MHz proton RF runs. (c) CAL timing vertex resolution as comparison with the CTD vertices. (d) Vertex position dependence of the NC-DIS acceptance, for $Q^2 > 10 \, \text{GeV}^2$.

6.5 Electron energy response

As already mentioned, the electron energy measurement is less reliable than the hadron angle measurement in the kinematics reconstruction. The main reason is that a large migration of the reconstructed value of x can be caused by a small shift in the measured electron energy, if the energy is around the beam energy. There are two sources that degrade the measured electron energy: one is the error of the energy calibration, the other is the dead material in front of CAL.

Usually the latter is recovered by using the Monte Carlo events that passed a carefully constructed detector simulation program. The major dead material is that of the frames and cables of the tracking detector. The amount of the dead material ranges from about one radiation length (1λ) in most of the solid angle to a few λ around the beampipe region. Especially for the beampipe region, the amount of dead material that the electron travels through depends on the vertex position.

The energy spectrum of the scattered electron is in general dependent on the structure function. However the dependence is not apparent in the large-x and moderate-Q^2 region where the electron energy is near to the beam electron energy. For the ideal detector, the electron energy spectrum forms a kinematic peaks at the beam energy.

In Fig. 6.7-(a) the kinematic peak in the region of $x > 0.003$ and $10\,\mathrm{GeV}^2 < Q^2 < 100\,\mathrm{GeV}^2$ is compared between data and Monte-Carlo. It is observed that the peak of data is degraded by 4 %, which is much larger than the energy calibration uncertainty. Therefore the amount of the dead material which is underestimated in the Monte-Carlo is evaluated from the degraded energy in the data.

Using the information of the amount of the dead material which is known for Monte Carlo and estimated for data, the measured energy can be corrected for the energy loss by the dead material. The corrected spectrum for the kinematic peak is compared in Fig. 6.7-(b). In Fig. 6.7-(c) the spectrum of the whole kinematic range is compared. The corrected electron energy provides independent information for the cross-check of the hadron angle measurement of the double-angle method.

6.6 Resolution for the kinematic variables

The reconstructed kinematic variables inherit the errors of the measured quantities. The errors of the kinematic variables differ among reconstruction methods, since
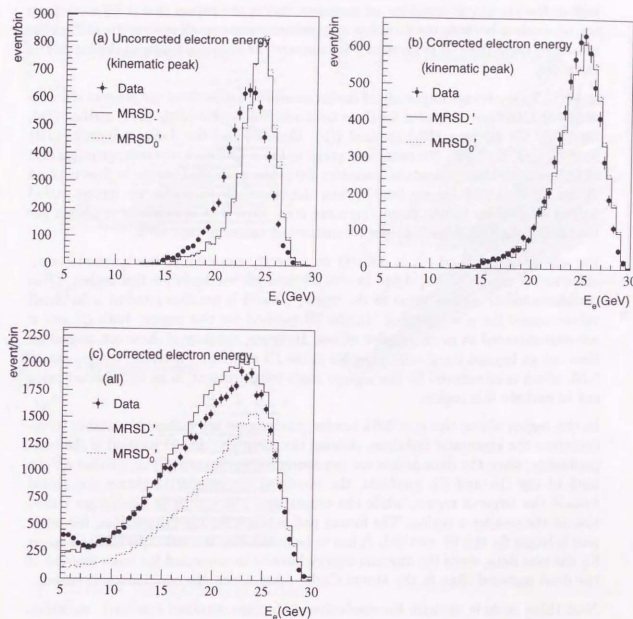
Figure 6.7: Electron energy spectrum: (a),(b) Uncorrected and corrected electron energy distributions at the kinematic peak for data and Monte Carlo with two different structure functions, MRS D$_-$ and MRS D$_0'$. (c) Electron energy spectrum for the whole kinematic range.

both the used quantities and the derivation formulae are different. In some kinematic region, the kinematic variables are reconstructed in the region that is far away from the true values because the formulae may enhance some small systematic shift in the measured quantities. It is necessary to compare the errors in terms of the kinematic variables.

In Fig. 6.8 the average migration of the kinematic variables from the generated values of Monte Carlo are compared for three methods: the double-angle (DA) method ((a), Eq.2.30), the electron (EL) method ((b), Eq.2.25) and the Jacquet-Blondel (JB) method ((c), Eq.2.28). For each data point in the x-Q^2 plane, the average migration of the reconstructed kinematic variables from the generated values is drawn as an arrow. If the arrow has no length, then the kinematic variables are reconstructed correctly; if many arrows point the same area, then it is impossible to obtain the true kinematic variables from the reconstructed values in that area.

For any of the methods, it is difficult to correctly reconstruct the kinematic variables in the region of $y < 0.04$. In the DA and EL methods for this region, Q^2 is reconstructed at a close value to the true Q^2, but x is reconstructed at a far small value around the $y = 0.04$ line. In the JB method for this region, both Q^2 and x are reconstructed at much smaller values. However, the flow of the event migration does not go beyond the $y = 0.04$ border in the JB method. Therefore, the y_{JB} cut at 0.04, which is introduced for the hadron angle measurement, is an effective selection cut to exclude this region.

In the region above the $y = 0.04$ border, the arrows are sufficiently stable to reconstruct the kinematic variables. Among the methods, the JB method is the least preferable, since the data points are reconstructed systematically at smaller Q^2. In both of the DA and EL methods, the events in the smallest-x corner are pulled toward the larger-x region, while the events near the $y = 0.04$ border are pulled toward the smaller-x region. The former pull is larger for the DA method; the latter pull is larger for the EL method. It has to be noted that the latter pull is even larger for the real data, since the electron energy have to be corrected for more amount of the dead material than in the Monte Carlo, upon which the comparison is based.

Next thing to do is to check the resolution of the reconstructed kinematic variables. The main purpose to check the resolution is to find suitable bin sizes for x and Q^2. The x and Q^2 resolution as functions of x and Q^2 is shown in Fig. 6.9 for the DA method and in Fig. 6.10 for the EL method. The error bars show the resolution of the kinematic variables. In general, the resolution of Q^2 is much better than that of x. The reconstructed x of the DA method has smaller spread and larger x dependent deviation of the mean value than that of the EL method. In the DA method, there
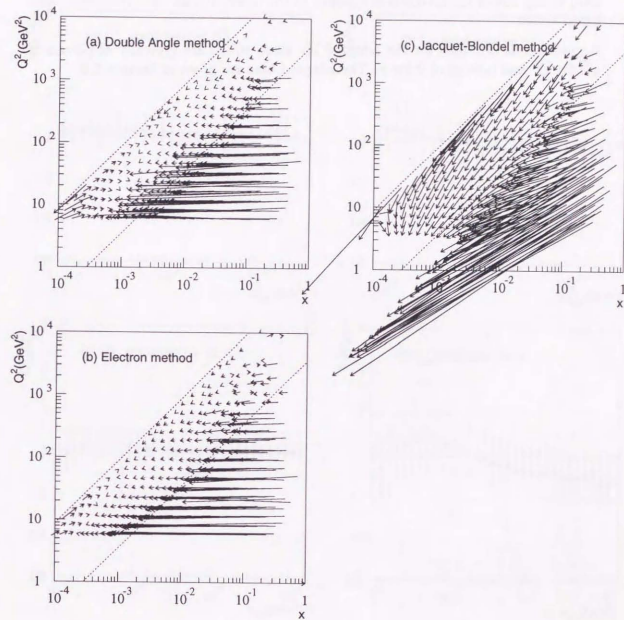
Figure 6.8: Event migrations on the x-Q^2 plane of (a) the DA method, (b) the EL method and (c) the JB method.

is a small deviation of Q^2 at small-x, which is not observed in the EL method. It is hard to say one of the methods is superior to the other, at least on the Monte Carlo based study.

A guideline is obtained for the adopted bin sizes, which are typically of powers of $\sqrt{2}$ for Q^2 and powers of 2 for x. The adopted bins are given in Section 7.6.
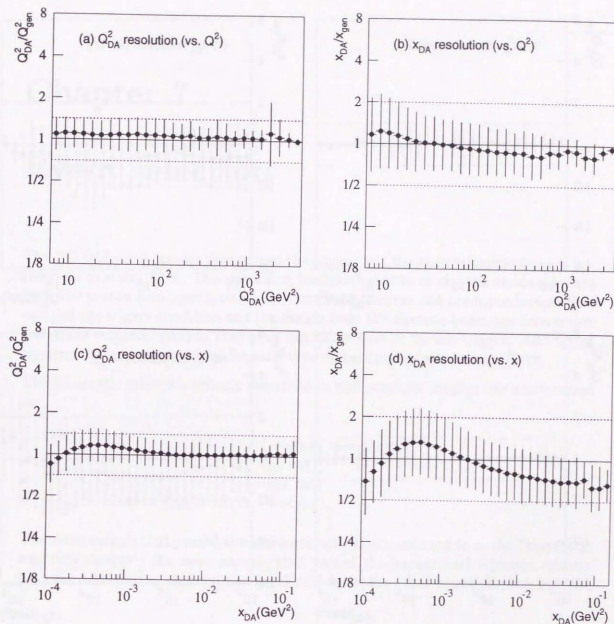
Figure 6.9: x-Q^2 resolution for the DA method: (a) Q^2-dependence of the Q^2 resolution. (b) Q^2-dependence of the x resolution. (c) x-dependence of the Q^2 resolution. (d) x-dependence of the x resolution.
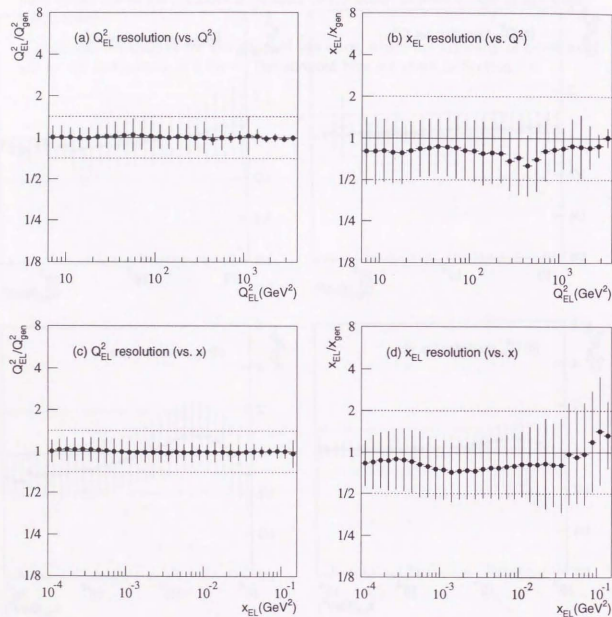
Figure 6.10: x-Q^2 resolution for the EL method: (a) Q^2-dependence of the Q^2 resolution. (b) Q^2-dependence of the x resolution. (c) x-dependence of the Q^2 resolution. (d) x-dependence of the x resolution.

Chapter 7

Event selection

The NC-DIS event sample that passed the trigger and the kinematic selections is purified up to about 85 %. The remaining background sources are, the residual events from the proton beam-gas interaction, cosmic ray muons and photoproduction that escaped the trigger condition and the events from the electron beam-gas interaction and QED-compton process that were not taken care of by the trigger. Additional rejection criteria are required for each type of background.

The kinematic selection criteria described in the previous chapter are summarized as:

- $E'_e > 5 \, \text{GeV}$ (electron energy cut)
- $y_{\text{el}} < 0.95$ (y_{el} cut)
- $y_{\text{JB}} > 0.04$ (y_{JB} cut)
- $|X_{\text{el}}| > 16 \, \text{cm}$ or $|Y_{\text{el}}| > 16 \, \text{cm}$ (box cut).

The event sample that passed the kinematic selection is referred to as the "kinematic selection sample"; the event sample that passed the background rejection criteria that are described in this chapter is referred to as the "final selection sample."

7.1 Proton beam-gas rejection

The proton beam-gas background shares only 0.5 % of the kinematic selection sample after the CAL timing cut of the trigger. The remaining background is still reduced further by tighter CAL timing cut, because NC-DIS with the scattered electron in

Figure 7.1: A close look at the CAL timing: (a) Log-scaled contour of the distribution of t_R versus $t_F - t_R$. (b) Projection of (a) to t_R. (c) Various components of the t_R distribution, A (dashed line) is for the module center (within ± 8 cm from the center) and a small energy in HAC (< 2 GeV), B (dotted line) is for the module center and with a large energy in HAC (≥ 2 GeV) and C (dotted-dashed line) is (d) Horizontal position dependence of t_R.
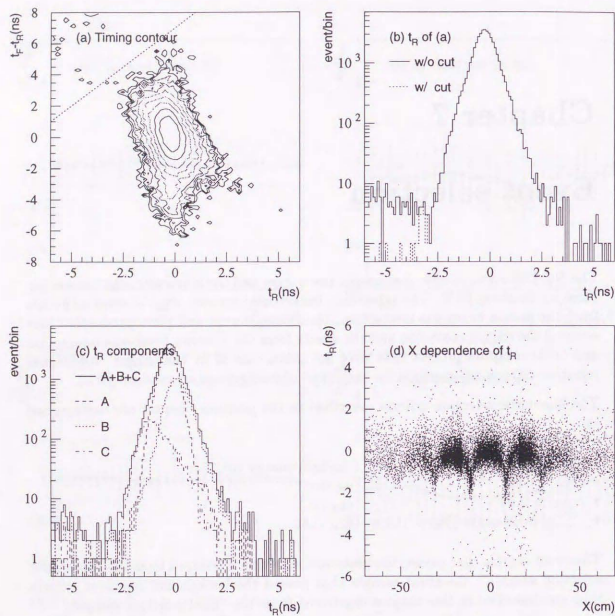
RCAL provides a better timing resolution than the events without the electron in RCAL.

Fig. 7.1-(a) shows log-scaled contour curves on the timing distribution of t_R (RCAL timing) versus $t_F - t_R$ (FCAL/RCAL time difference). The main peak is centered at origin, with a longer shape in the vertical direction. This vertical spread is due to the FCAL time spread, namely toward the down side due to the proton beam leakage into the 1 RF earlier bucket. The spread toward the down-right side is due to the RCAL time spread. The spread of the main peak is sufficiently contained within the timing cut of the trigger indicated by the edge of the plot. It is also seen that the events from the background peak is mostly removed except for some events in the up-left corner. The remaining events above the line are removed by requiring the condition,

$$(t_F - t_R) - t_R < 7\,\text{ns}.$$

The amount of the excluded events is clearly seen in the projection to t_R of Fig. 7.1-(b). Before this cut (solid line) the background tail in the earlier t_R side is seen; after this cut the tail disappears.

If the energy deposit in FCAL is not sufficiently large to measure t_F, the proton beam-gas background has to be removed only by t_R. Fig. 7.1-(c) shows the t_R distribution, whose shape is closely understood to be a superposition of narrower ($\sigma \sim 0.5$ ns) distributions of different components. This is because the timing is dominated by the energetic scattered electron in RCAL. The later component (B) is due to the HAC contribution that gives a later time; the earlier component (C) is due to the shower particles penetrating into the WLS directly if the electron position is near the module boundary. The correlation of the earlier time and the module boundary is clear in Fig. 7.1-(d). Therefore, if the electron is found in RCAL, a tighter RCAL timing cut,

$$-3\,\text{ns} < t_R < 4\,\text{ns}$$

is applied to reject the proton beam-gas background.

The remaining background contribution in the final selection sample can be estimated with the unpaired proton bunch. The only one event found in the smallest Q^2 region means that the proton beam-gas background is negligible in the final event sample.
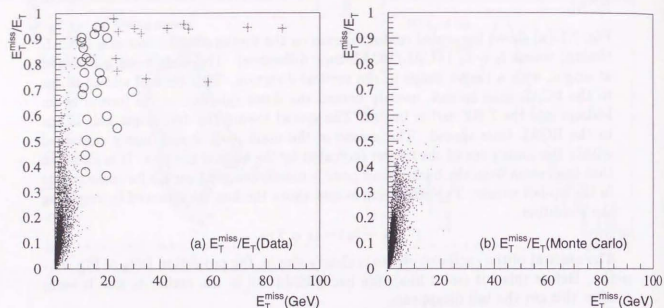
Figure 7.2: Distribution of $\not{E}_T$ versus $\not{E}_T/E_T$ for the cosmic ray muon rejection. Crosses and circles are the muons removed by the selection (1) and (2) respectively. Data is shown in (a) and Monte Carlo is shown in (b).

7.2 Muon rejection

A typical cosmic ray muon event that is not rejected by the muon finding algorithm has a large energy deposit in EMC that is mis-identified as the scattered electron. In such a case, most of the energy is concentrated around the fake electron, and a small amount of energy is found in the other side of CAL in azimuth angle. Therefore, this class of events are identified by large missing transverse energy ($\not{E}_T$) with almost equally large transverse energy (E_T). These quantities are defined by:

$$E_T = \sum_i E_i \sin\theta_i$$

$$\not{E}_T = \sum_i \sqrt{\left(\sum_i E_i \sin\theta_i \cos\phi_i\right)^2 + \left(\sum_i E_i \sin\theta_i \sin\phi_i\right)^2},$$
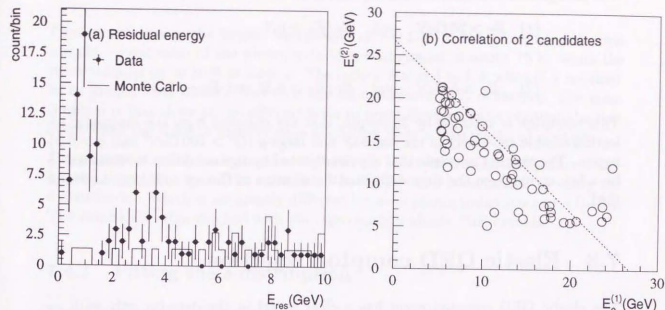
Figure 7.3: QED-compton event rejection: (a) Residual energy distribution. The peak at zero in data is from QED-compton, which is not seen in Monte Carlo. (b) Energy correlation of two electron candidates. The energy sum is around the beam energy.

where the sum is over the CAL cells. For NC-DIS, $\not{E}_T$ is always small since the transverse momentum is balanced.

The distribution of $\not{E}_T$ versus $\not{E}_T/E_T$ is shown in Fig. 7.2 for data and NC-DIS Monte Carlo. In the data plot (a), a band of NC-DIS events with small $\not{E}_T$, a band of clear cosmic ray muon candidates with $\not{E}_T/E_T$ close to unity and large $\not{E}_T$ and intermediate events are seen. Clear candidates indicated by crosses are easily removed. Intermediate candidates indicated by circles are further required to have little energy deposit in the beampipe region of CAL (E_{bp}), since the possibility of a muon to go through the beampipe region is small.

The background selection criteria are chosen to be

$$(1) \quad \not{E}_T > 20\,\text{GeV} \quad \text{and} \quad \not{E}_T/E_T > 0.7$$

or

$$(2) \quad \not{E}_T > 5\,\text{GeV} \quad \text{and} \quad \not{E}_T/E_T > 0.35 \text{ and } E_{\text{bp}} < 1\,\text{GeV}.$$

This condition is satisfied by 38 events, that are removed from the kinematic selection sample especially in the large-Q^2 and large-y ($Q^2 > 100\,\text{GeV}^2$ and $y > 0.5$) region. The number of events that are not rejected by this condition is estimated to be a few events from the time difference distribution of the up and down halves of CAL.

7.3 Elastic QED compton rejection

The elastic QED compton event has a clear signal in the detector only with an electron and a photon. If either the electron or the photon is detected by CAL, it is efficiently found by the electron identification algorithm. The event is not rejected by any of the succeeding event selection criteria if the other is assumed to be the hadron system.

However, the electron identification algorithm usually labels the other as the second candidate of the scattered electron. Then, the QED compton events are identified by two electron candidates with no other energy. The distribution of the residual energy (E_{res}) is shown in Fig. 7.3-(a) for the events with two electron candidates with more than 5 GeV energy.

The events that satisfy the criteria:

$$E_e^{(1)} > 5\,\text{GeV}$$
$$E_e^{(2)} > 5\,\text{GeV}$$
$$E_{\text{res}} \equiv E_{\text{CAL}} - E_e^{(1)} - E_e^{(2)} < 1.5\,\text{GeV}$$

are classified as QED compton events and are removed from the kinematic selection sample. The fraction of the QED-compton background is as small as 0.1, but it is enhanced up to 1 % at large-Q^2 and large-y ($Q^2 > 100\,\text{GeV}^2$ and $y > 0.5$). The energy sum of the two electron candidates of the QED-compton event corresponds to the initial beam energy, as shown in Fig. 7.3-(b).

7.4 Photoproduction background

Photoproduction is the largest background of NC-DIS in the kinematic selection sample. Total ratio of the photoproduction background is about 15 %, while the ratio becomes up to 30 % at large-y. The ratio is lowered to 5 % when δ is required to be greater than 32 GeV, and then the ratio becomes 10 % at large-y. The main problem is that there are no efficient ways to reject the particular photoproduction event when the electron identification algorithm finds a fake scattered electron.

The photoproduction background contribution is subtracted statistically after dividing the events into bins. The amount of the background is estimated by using the δ distribution, which is apparently different between photoproduction and NC-DIS. The results are cross-checked with photoproduction Monte Carlo events.

7.4.1 Fitting the δ distribution

The photoproduction background events that have small δ are easily discriminated from NC-DIS. For an NC-DIS event, δ scarcely go below 32 GeV and cannot go above 60 GeV even if the detector resolution is taken into account, except for the case of the initial state radiation. Therefore, δ is required to be within a range of

$$32\,\text{GeV} < \delta < 60\,\text{GeV}$$

in the final event selection (It is referred to as the "δ cut"). The photoproduction distribution still has a long overlapping tail into the NC-DIS region.

The background contribution has to be estimated for each bin of x-Q^2. The δ distribution is fitted to a phenomenological function $N(\delta)$, which is a superposition of the NC-DIS and photoproduction distribution. The NC-DIS distribution N_{DIS} is modeled by an asymmetric gaussian function with a constant offset for the initial state radiation events; the photoproduction tail N_{PHP} is modeled by the right side

---

† $\delta \equiv \sum (E_i - (p_Z)_i)$ (sum is over all the CAL cells) as defined in Section 4.3.2.

of a gaussian function:

$$N(\delta) = N_{\text{DIS}}(\delta) + N_{\text{PHP}}(\delta)$$

$$N_{\text{DIS}}(\delta) = \begin{cases} A \exp\left(-\dfrac{(\delta - \delta_0)^2}{2\sigma_1^2}\right) & \text{if } \delta > \delta_0 \\[2ex] A\left[f + (1-f)\exp\left(-\dfrac{(\delta - \delta_0)^2}{2\sigma_2^2}\right)\right] & \text{if } \delta < \delta_0 \end{cases} \tag{7.1}$$

$$N_{\text{PHP}}(\delta) = B \exp\left[-\dfrac{(\delta - \delta_{\text{PHP}})^2}{2\sigma_{\text{PHP}}^2}\right].$$

The widths of the asymmetric gaussian σ_1, σ_2 and the fraction of the constant offset f are obtained with NC-DIS Monte Carlo with a same function form N_{MC}:

$$N_{\text{MC}}(\delta) = \begin{cases} A' \exp\left(-\dfrac{(\delta - \delta_0')^2}{2\sigma_1'^2}\right) & \text{if } \delta > \delta_0' \\[2ex] A'\left[f' + (1-f')\exp\left(-\dfrac{(\delta - \delta_0')^2}{2\sigma_2'^2}\right)\right] & \text{if } \delta < \delta_0'. \end{cases} \tag{7.2}$$

Since the widths σ_1' and σ_2' are slightly narrower in Monte Carlo due to the incompletely simulated electron energy resolution, a factor g ($\gtrsim 1$) is multiplied for the fitting parameters: $\sigma_1 = g\sigma_1'$, $\sigma_2 = g\sigma_2'$. To conserve the area of the constant offset, f' is also multiplied by g: $f = gf'$. Then, A, B, δ_0, δ_{PHP}, σ_{PHP} and g are the free parameters of the fitting.

In Fig. 7.4 all the fitting results are shown for the bins in which F_2 are obtained.[‡] In each distribution the large peak around 45 to 50 GeV (degraded from ideal $2E_e$ due to the detector effect) is the NC-DIS peak and the tail from the left end at 25 GeV is the photoproduction contribution. In the same row of Q^2 the photoproduction background is largest in the largest-y (smallest-x) bin and rapidly diminishes in the small-y bins. The fraction of the photoproduction background does not decrease in the large-Q^2 bins.

The fitting is performed with MINUIT[55] program. The estimated number of the background events is given by integrating Eq.7.1 from 32 GeV to 60 GeV with the obtained fit parameters. Covariant error matrix of the fit parameters is propagated to the integration to give the error of the background. The obtained number of the photoproduction events is 2312 ± 171 in total, or $\sim 20\%$ in the largest bin but typically less than 10 % in the other bins.

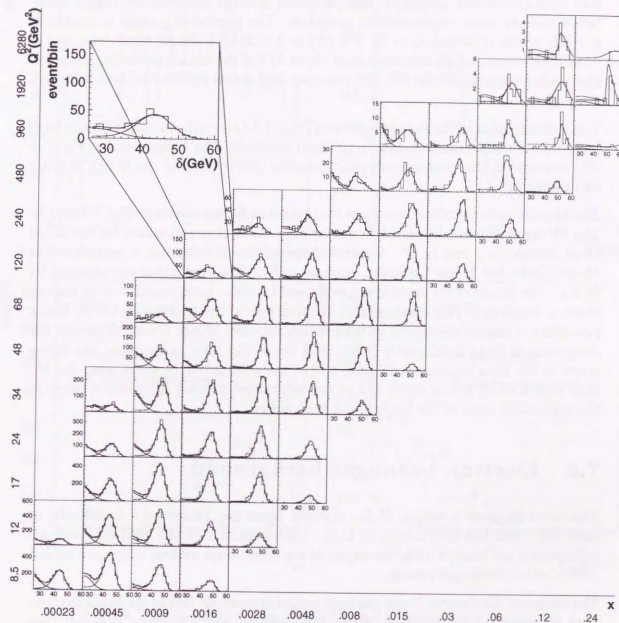[‡] These bins are defined in Section 8.3.

Figure 7.4: Bin-by-bin fitting results of the δ distribution.

7.4.2 Photoproduction Monte Carlo

The photoproduction Monte Carlo events are generated with PYTHIA[40] minimum bias photoproduction generator, and processed through the detector/trigger simulation and the event reconstruction programs. The generated y-range is limited to $y > 0.6$, which corresponds to $E_\gamma > 0.6E_e$ or $\delta > 32$ GeV for an ideal detector. In total 150k events, which corresponds to about $1/3$ of the data luminosity, are generated. After applying all the NC-DIS selection, 389 events remains in the $\delta > 32$ GeV range.

The y distribution of the remaining events (Fig. 7.5-(a)) confirms that only the large y photoproduction events remain in the final selection. The δ distribution (Fig. 7.5-(b)) shows that the phenomenological gaussian distribution of the fitting is not a bad choice.

The Monte Carlo distribution is compared with the fitting results in Fig. 7.5-(c),(d). The fitting results are obtained by performing the fitting procedure for the sliced event sample in y and in Q^2. General shape of the distribution is reproduced in Monte Carlo, but Monte Carlo can generate only $2/3$ of events that are obtained by fitting. The excess of the event is not explained by other background sources such as electron beam-gas. This disagreement is either due to the uncertainty of the fitting procedure or due to the model of the photoproduction Monte Carlo. Although the disagreement looks significantly larger than the fitting error in the plots, the fitting errors in the final bins are as large as $2/3$ of the subtraction in some bins. For the bins with a small fitting error, $1/3$ of the subtracted number of events is taken as the systematic error of the background subtraction.

7.5 Electron beam-gas background

The event-by-event rejection of the electron beam-gas background is difficult, at least only with the information of CAL. Characteristics of the electron beam-gas background are studied with the unpaired electron bunch events, which are almost pure electron beam-gas events.

The source of the electron beam-gas background is small-Q^2 DIS of the beam electron with the residual gas nucleus. When the scattered electron angle is larger than necessary to impact outside the box cut, the trigger and selection efficiency is as large as that of normal NC-DIS. The fragments of the broken-up nucleus either hit RCAL or escape through the rear beampipe hole.

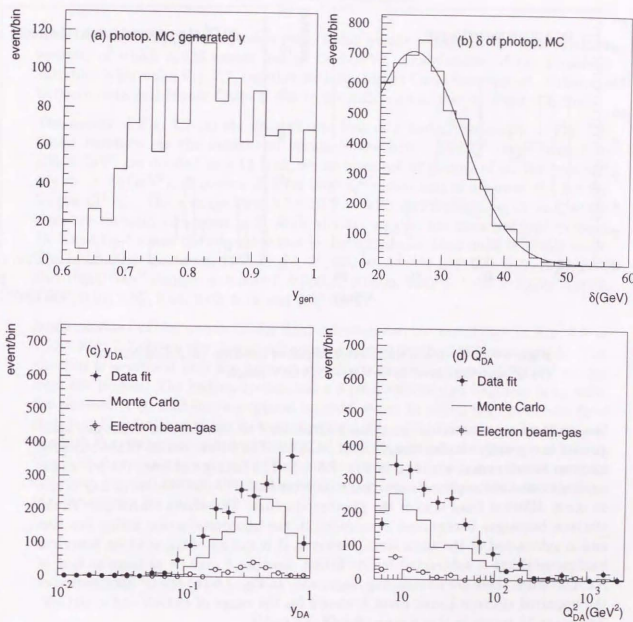**Figure 7.5:** Photoproduction Monte Carlo: (a) Generated y distribution. (b) Reconstructed δ distribution. (c) Comparison of reconstructed y_{DA} with the fitting result. (d) Comparison of reconstructed Q^2_{DA} with the fitting result.
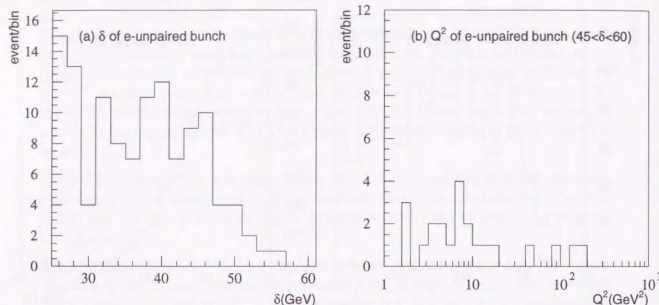
Figure 7.6: Events in the electron unpaired bunches: (a) δ distribution. (b) Q^2 distribution of 45 GeV $< \delta <$ 60 GeV range.

Due to large amount of the escaping fragments, δ of the electron beam-gas background is generally smaller than that of NC-DIS. The δ distribution of the unpaired electron bunch events is shown in Fig. 7.6-(a). The falling tail from the left end is similar to that of the photoproduction δ distribution. The distribution of x-Q^2 is not so much different from that of the photoproduction. Therefore, a large part of the electron beam-gas background is included in the photoproduction fitting function and is subtracted at the same time. However, it is not all of the electron beam-gas background that is subtracted by the fitting, because δ may be as large as that of NC-DIS when there are no escaping fragments. In Fig. 7.6-(b) the Q^2 distribution of the unpaired electron bunch event is shown for the range of 45 GeV $< \delta <$ 60 GeV. There are 21 events in this δ range for $Q^2 > 7$ GeV^2.

The electron beam-gas background rate is presumably proportional to the electron beam intensity. In the 1993 run period the integrated intensity of the unpaired electron bunches is about $1/7.5$ of the colliding bunches. Possible number of events that may not be subtracted by the fitting is estimated to be less than 1 % which is much smaller than the fitting error.

7.6 Final selection event sample

After all the background rejection cuts, 45062 events remain in the final selection sample, of which 41436 events has $Q^2 > 7$ GeV^2. Distribution of the kinematic variables is shown in Fig. 7.7, together with the Monte Carlo distribution. Difference between data and Monte Carlo is due to the difference of the structure function.

The events of Fig. 7.7-(a) are divided into bins of x and Q^2 as shown in Fig. 7.8. Given numbers are the number of events in the bins. The Q^2 range from 5 to 10000 GeV^2 are divided into 14 bins, whose sizes are of powers of $\sqrt{2}$ for small-Q^2 region (< 80 GeV^2), of powers of 2 for large-Q^2 region and of a power of 4 for the largest-Q^2 bin. The x range from 0.7×10^{-4} to 0.32 are divided into 13 bins, whose sizes are typically of powers of 2, while slightly smaller bin sizes are used between 10^{-2} and 10^{-3} where the migration in x is slightly smaller than outside of this range. The bin boundaries are at 5, 7, 10, 14, 20, 28, 40, 56, 80, 160, 320, 640, 1280, 2560 and 10000 GeV^2 for Q^2; at 0.00007, 0.00015, 0.0003, 0.0006, 0.0012, 0.002, 0.0036, 0.006, 0.01, 0.02, 0.04, 0.08, 0.16 and 0.32 for x.

Some pictures of the events in the final selection sample are shown in Fig. 7.9 to 7.12. Fig. 7.9 shows the largest-Q^2 event observed in the 1993 run period. The electron is scattered into the forward direction, acquiring nearly 200 GeV energy from the proton. The hadron system has a 2-jet structure and balances in p_T with the electron. Fig. 7.10 shows a typical large-Q^2 event, in which the electron-hadron system is boosted toward the forward direction. Fig. 7.11 shows a smaller-Q^2 event, in which the electron is scattered into RCAL and the current jet is going into FCAL. Fig. 7.12 shows an example of the very small-x event, in which the electron-hadron system is boosted toward the backward direction and therefore both the electron and the current jet go into RCAL.

(a) Q^2_{DA} vs. x_{DA} (Data)

(b) Q^2_{DA} distribution
+ Data
— MRSD'
···· MRSD$_0$'

(c) x_{DA} distribution
+ Data
— MRSD'
···· MRSD$_0$'

(d) y_{DA} distribution
+ Data
— MRSD'
···· MRSD$_0$'
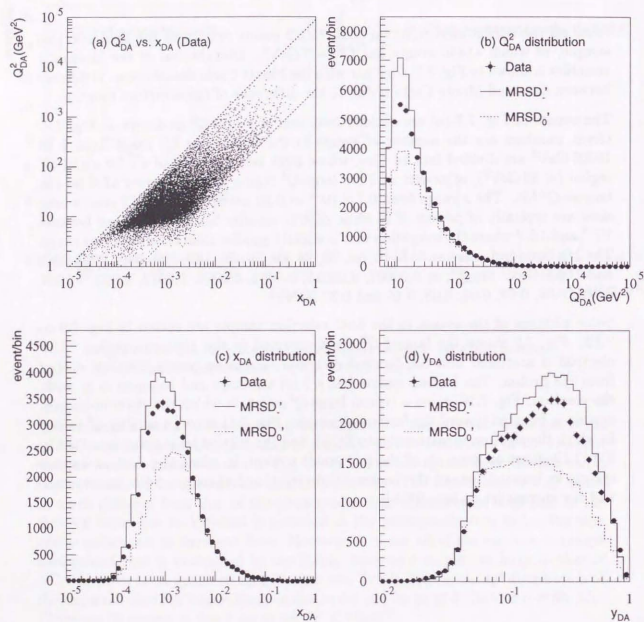
Figure 7.7: Distributions of the kinematic variables: (a) Events in the x-Q^2 plane. (b) the Q^2 distribution, (c) the x distribution and (d) the y distribution.

94
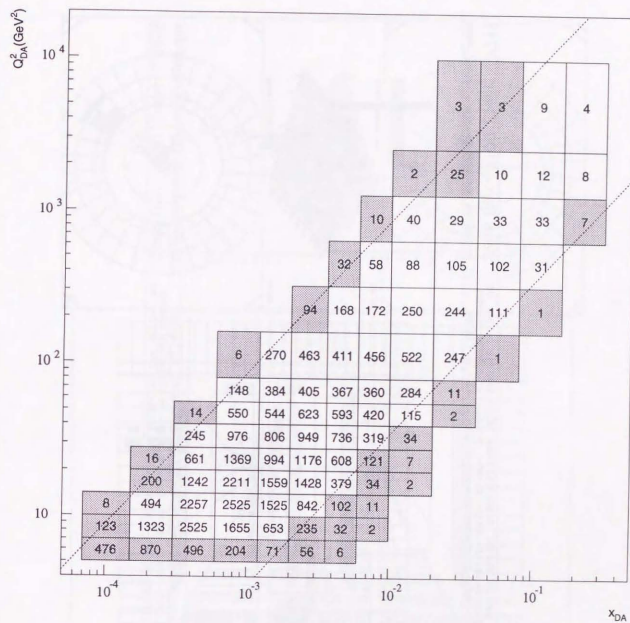
Figure 7.8: The bin division for the F_2 extraction and the number of events in the final event sample after the background subtraction in each bin. Lines indicates the kinematic limit of $y = 1$ (upper) and the selection criteria of $y = 0.04$ (lower). Hatched bins are not used in the F_2 extraction as chosen in Section 8.3.

95
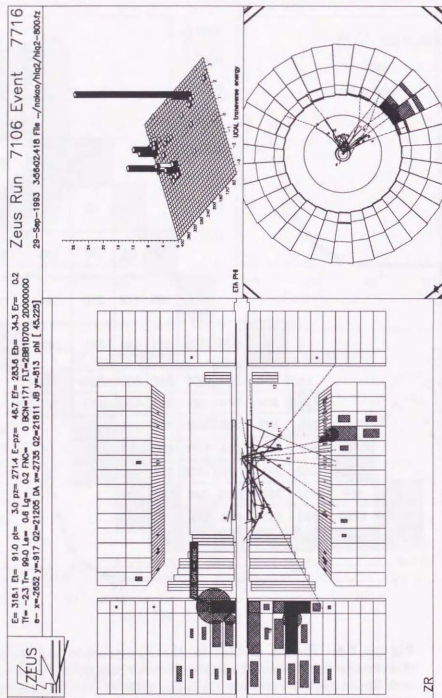
Figure 7.9: The largest-Q^2 event with the scattered electron in FCAL. $Q^2 = 21000\,\mathrm{GeV}^2$, $x = 0.27$ are reconstructed.
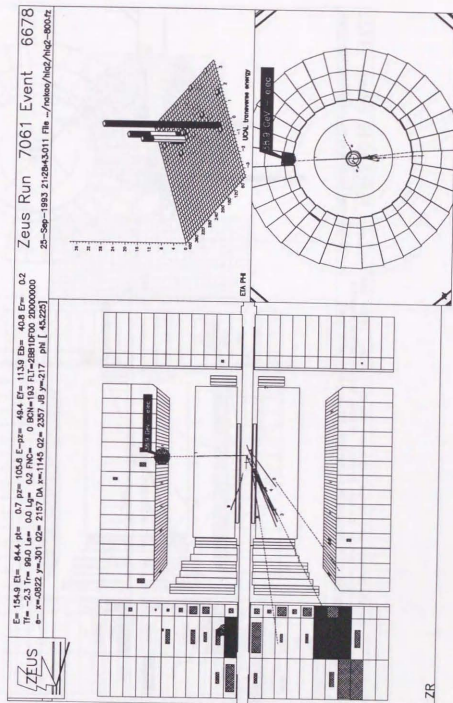
Figure 7.10: An event in the second largest Q^2 bin with the scattered electron in BCAL. $Q^2 = 2300\,\mathrm{GeV}^2$, $x = 0.11$ are reconstructed.
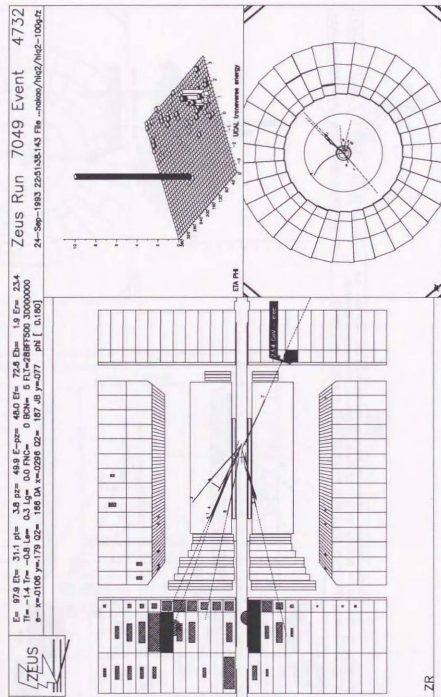
Figure 7.11: A clean NC DIS event with the scattered electron in RCAL, having reconstructed $Q^2 = 190 \, \text{GeV}^2$, $x = 0.03$.
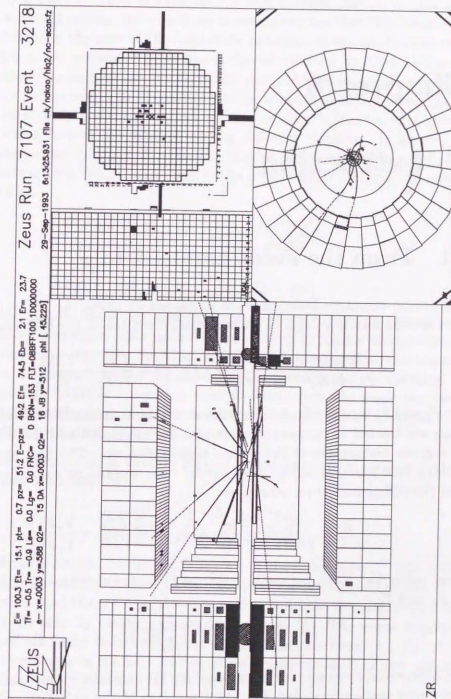
Figure 7.12: An event with both the electron and the current jet in RCAL, having reconstructed $Q^2 = 16 \, \text{GeV}^2$, $x = 0.0003$.

Chapter 8

F_2 extraction

8.1 From the event numbers to F_2

The proton structure function F_2 is extracted by using the $ep \to eX$ differential cross section formula (Eq.2.11), which can be written in the following form:

$$\frac{d\sigma_{\mathrm{NC}}(e^-p)}{dx\, dQ^2} = \frac{2\pi\alpha^2 Y_+}{xQ^4} \cdot F_2 \cdot \left\{ 1 - \frac{y^2 F_L}{Y_+ F_2} + \frac{Y_- x F_3}{Y_+ F_2} \right\}. \tag{8.1}$$

The F_L and F_3 terms in Eq.8.1 are estimated to be small for NC-DIS at HERA. These terms are treated as correction terms that are calculated with Eq.2.20 and Eq.2.12 for a given assumption of the parton distribution set. The first approximation of the structure function before these corrections, denoted as $\tilde{F}_2$, is directly obtained from the differential cross section as

$$\tilde{F}_2 \equiv \frac{xQ^4}{2\pi\alpha^2 Y_+} \frac{d\sigma_{\mathrm{NC}}}{dx\, dQ^2} = F_2 \left\{ 1 - \frac{y^2 F_L}{Y_+ F_2} + \frac{Y_- F_3}{Y_+ F_2} \right\}. \tag{8.2}$$

Then, using the calculated ratio of F_2^{MC} to $\tilde{F}_2^{\mathrm{MC}}$, the structure function is corrected for F_L and F_3,

$$F_2 = \tilde{F}_2 \cdot \left(\frac{F_2^{\mathrm{MC}}}{\tilde{F}_2^{\mathrm{MC}}} \right). \tag{8.3}$$

The differential cross section is corrected for the radiative events, since Eq.8.1 is the Born cross section formula. The main problem of the radiative correction is that the reconstructed values of x and Q^2 may differ from the true values at the hadron

vertex. In the case of the initial state radiation event, the radiated photon degrades the beam electron energy. Then neither the electron method nor the double angle method gives a correct answer, because these methods assume that the beam energy is fixed. It is better in the case of the final state radiation event, since most of the radiated photon is not separated from the scattered electron by CAL. When the photon is radiated in a large angle, it affects not only the electron measurement but also the hadron measurement in which the photon is counted as a hadron. In this case the Jacquet-Blondel method also gives a wrong answer. It is noted that different radiative correction factors are required among different methods. In general, the differential cross section of x, Q^2 is related to that of reconstructed x_{rec}, Q_{rec}^2 by a radiative correction term Δr_{rec}. In the case of the double angle method, the relation is written down as

$$\frac{d\sigma(x_{\mathrm{DA}}, Q_{\mathrm{DA}}^2)}{dx_{\mathrm{DA}}\, dQ_{\mathrm{DA}}^2} = (1 + \Delta r_{\mathrm{DA}}) \frac{d\sigma(x, Q^2)}{dx\, dQ^2}$$

or

$$\tilde{F}_2(x_{\mathrm{DA}}, Q_{\mathrm{DA}}^2) = (1 + \Delta r_{\mathrm{DA}}) \tilde{F}_2(x, Q^2).$$

Despite that the photon radiation probability can be calculated accurately with QED, the radiative correction term cannot be calculated explicitly unless the x-Q^2 distribution, hence the structure function, is known. It means that the radiative correction term of Monte Carlo is obtained for the given structure function. In other words the true radiative correction term is obtained at the same time when the structure function that reproduce the measured cross section is extracted by an iterative unfolding procedure.

The differential cross section is directly related to the number of measured events M in a small area of $\Delta x \Delta Q^2$ by

$$\frac{d\sigma(x, Q^2)}{dx\, dQ^2} = \frac{1}{\epsilon \mathcal{L}} \cdot \frac{M(x, Q^2)}{\Delta x \Delta Q^2}$$

where the coefficients are the overall efficiency ϵ and the luminosity $\mathcal{L}$. The overall efficiency is the product of the electron identification efficiency, the acceptance of the kinematic selections and the number of events variation due to the migrating events out of and into the area by taking reconstructed x and Q^2. The event migration causes the overall efficiency to be dependent on the structure function. The structure function dependence is resolved by the same procedure used in the radiative correction.

These three steps have to be applied reversely from the last one to the first to obtain F_2 from M. Since the last two steps are technically equivalent, they are performed

in a single unfolding procedure at the same time. When the Monte Carlo structure function equals to the true structure function, quantities at each step equal between data and Monte Carlo. This is written in the relation:

$$
\begin{aligned}
\frac{F_2^{\text{data}}}{F_2^{\text{MC}}} &= \frac{\tilde{F}_2^{\text{data}}}{\tilde{F}_2^{\text{MC}}} = \frac{d\sigma^{\text{data}}(x, Q^2)/dx\, dQ^2}{d\sigma^{\text{MC}}(x, Q^2)/dx\, dQ^2} \\
&= \frac{d\sigma^{\text{data}}(x_{\text{DA}}, Q_{\text{DA}}^2)/dx_{\text{DA}}\, dQ_{\text{DA}}^2}{d\sigma^{\text{MC}}(x_{\text{DA}}, Q_{\text{DA}}^2)/dx_{\text{DA}}\, dQ_{\text{DA}}^2} = \frac{M^{\text{data}}(x_{\text{DA}}, Q_{\text{DA}}^2)}{M^{\text{MC}}(x_{\text{DA}}, Q_{\text{DA}}^2)} = 1
\end{aligned}
\tag{8.4}
$$

Therefore to find a Monte Carlo structure function that gives the same measured event distribution as data is equivalent to find the true structure function. Then the Monte Carlo structure function is the unfolded structure function from data.

8.2   Unfolding procedure

The purpose of the unfolding procedure is to extract the true number of events N_i corrected for the detector effect and the radiation from the measured number of events M_i in each bin i ($i = 1 \ldots n$) of x-Q^2. The reverse of this is simulated with Monte Carlo, in which the number of measured events $M_i^{(0)}$ is obtained from the given initial distribution of the number of generated events $N_i^{(0)}$. If the measured numbers coincide between data and Monte Carlo ($M_i = M_i^{(0)}$ for all i), then $N_i^{(0)}$ equals to the true distribution N_i. Even if not, the measured distribution helps to obtain a closer Monte Carlo distribution to N_i. Ideally, the Monte Carlo distribution converges to the true distribution by iterating this step[58, 59].

The method to obtain the closer distribution uses the *initial probability* of the event. The probability P_{ij} for a generated event in bin i to be found in bin j is obtained with Monte Carlo. This probability does not depend on the structure function except for the small effect due to the gradient inside a bin, and therefore it is common for data and Monte Carlo:

$$
\begin{aligned}
M_j &= \sum_i P_{ij} N_i, \\
M_j^{(k)} &= \sum_i P_{ij} N_i^{(k)} \quad (k = 0, 1, \ldots).
\end{aligned}
\tag{8.5}
$$

The reverse of this, the initial probability Q_{ji} for an event found in bin j to originate in bin i is given by

$$
Q_{ji} = \frac{P_{ij} N_i}{\sum_l P_{lj} N_l},
\tag{8.6}
$$

which depends on the structure function because of N_i. From the nature of the probabilities, relations:

$$
\sum_i Q_{ji} = 1, \quad 0 \le \epsilon_i \equiv \sum_j P_{ij} \le 1
$$

are satisfied. These relations mean that the reconstructed events must originate in one of the bins, but the generated events may not be found in any of the bins. The efficiency ϵ_i is the probability of an event to be found in one of the bins.

Using Q_{ji}, the reverse of Eq.8.5 is given by

$$
N_i = \frac{1}{\epsilon_i} \sum_j Q_{ji} M_j,
\tag{8.7}
$$

with which the true event distribution N_i is obtained, provided true Q_{ij} is known. Although Q_{ji} is structure function dependent, it is weak dependence because the largest Q_{ji} is the correctly generated probability Q_{jj} which does not depend on the structure function. Therefore Q_{ij} calculated with Monte Carlo,

$$
Q_{ji}^{(k)} = \frac{P_{ij} N_i^{(k)}}{\sum_l P_{lj} N_l^{(k)}} \quad (k = 0, 1, \ldots)
\tag{8.8}
$$

is a good guess and the resulting

$$
N_i^{(k+1)} = \frac{1}{\epsilon_i} \sum_j Q_{ji}^{(k)} M_j \quad (k = 0, 1, \ldots).
\tag{8.9}
$$

has a closer distribution to true N_i. New $M_j^{(k+1)}$ is then calculated from $N_i^{(k+1)}$ with Eq.8.5 and it is compared with M_j to check the conversion.

In practice, M_j includes the statistical fluctuation, which is also get unfolded. Even if the fluctuation is small, the unfolded fluctuation can be large since it is amplified by the $1/\epsilon_i$ factor in the worst case. When this procedure is simply iterated, this amplifying factor is accumulated, and then the resulting distribution is heavily oscillated. The oscillation is avoided by limiting the bins to where $1/\epsilon$ is not large and by smoothing the distribution before each iteration step.

The smoothing is performed by fitting the ratio of the number of events after to before unfolding. The fitting is done separately for the x distribution and the Q^2 distribution. Since the ratio should not be rapidly changing and the number of data points are small (eight at maximum), the ratios are fitted robustly with a quadratic

function if there are more than three data points. Otherwise the ratios are fitted with a linear function. The results are used for the next step of the iteration.

With this unfolding procedure, the distribution converges quickly. The conversion is monitored by checking χ^2/n, which is defined by

$$\frac{\chi^2}{n} = \frac{1}{n}\sum_{j}^{n}\frac{(M_j^{(k)} - M_j)^2}{\left[(\Delta M_j^{(k)})^2 + (\Delta M_j)^2\right]}. \tag{8.10}$$

After iterating twice or three times, χ^2/n becomes stable with the value around unity. The number of iteration steps is chosen to be three.

8.3 Bin selection criteria

Bins for which the values of F_2 are extracted are chosen from the bins in Fig. 7.8. If there are events in the bins outside the kinematic acceptance, those events are mostly migrated from the other bins. The border of the kinematic acceptance is at $y = 1$ of the kinematic limit, at $y = 0.04$ of the y_B cut and around $Q^2 = 7$ of the box cut. Since the borders are not parallel to the bin boundaries, there are ambiguous bins that may or may not be able to be used.

The criteria of the bin selection are given by two parameters, the purity p_i and the correction factor c_i, that are defined by

$$\begin{aligned}
p_i &\equiv \frac{\text{number of correctly found events in bin } i}{\text{number of found events in bin } i} = Q_{ii}, \\
c_i &\equiv \frac{\text{true number of events in bin } i}{\text{number of found events in bin } i} = \frac{N_i}{M_i}.
\end{aligned} \tag{8.11}$$

In order to guarantee that the number of events in the bin represents the true number of events in the bin, the bins that satisfy

$$\begin{aligned}
p_i &> 0.2 \\
0.5 &< c_i < 4
\end{aligned} \tag{8.12}$$

are chosen. In addition, at large-Q^2 ($Q^2 > 100\,\text{GeV}^2$) the smallest x bins of each Q^2 are excluded from the choice since the background fitting becomes rather difficult due to the limited statistics.

With these criteria, the bins outside the kinematic acceptance are excluded. Finally 62 bins are chosen and are shown in Fig. 7.8 as the unhatched bins.

Chapter 9

Results

9.1 Extracted results of the structure function F_2

Following the procedure of Chapter 8, the values of the structure function F_2 are extracted for 62 data points from $Q^2 = 8.5\,\text{GeV}^2$, $x = 2.3 \times 10^{-4}$ up to $Q^2 = 6280\,\text{GeV}^2$, $x = 0.24$. The results of F_2 are given in Table 9.1. In the table, each data point is represented by the central value of the x, Q^2 bin. Given statistical error is propagated from the error of the number of events including the fitting error of the subtracted background and the statistical error of Monte Carlo, used in the unfolding procedure. Systematic error is obtained as described in the next section. In Table 9.2 given are the numbers of events and the subtracted background, the purities and the correction factors that are used in the bin selection criteria and the F_L and F_3 correction factors. The fraction of the subtracted background is up to 20 %; the error of the subtraction is up to 10 %. The purities are typically about one third in the small-Q^2 bins and go up to unity in the large-Q^2 bins. The correction factors are typically around unity with exceptions around the kinematic boundaries. The F_L correction becomes as large as 17 % in the small-x and large-y bin. The F_3 correction becomes up to 11 %, but they are only recognizable in the very large Q^2 bins where the statistical errors are also large.

The x-dependence of F_2 at fixed values of Q^2 is visualized in Fig. 9.1. The results are shown as the closed circles with the statistical error bars (inner) and the total error bars (outer). It is clearly seen that F_2 increases in the small x region below $x = 10^{-2}$. Given curves are theoretical predictions of F_2 that are discussed in the next chapter.

The Q^2-dependence of F_2 at fixed values of x is similarly visualized in Fig. 9.2. It is seen that F_2 rapidly increases along with $\log Q^2$ at small x. The slope of the increase becomes less steeper as x becomes larger, and it becomes almost flat at the largest three x bins. This behavior corresponds to the standard QCD (GLAP) evolution of F_2.

9.2 Systematic error estimation

The systematic error of this analysis is caused by the uncertainty of the following categories:

1. electron identification efficiency

2. measured electron angle

3. measured hadron angle

4. kinematic acceptance around boundaries

5. background subtraction

6. stability of the unfolding procedure

7. F_L and F_3 correction

8. absolute value of the luminosity.

If the systematic error for each category is obtained and the error is propagated independently of the other errors, the systematic error of the final results is easily obtained. However, for most of the categories neither the error is uniquely determined nor the propagation is independent of the other errors. Alternatively, some conditions that are relevant to the category are slightly altered and the deviation in the unfolded result from the final result is taken as the systematic error. Because the analysis should be insensitive to such small changes in the choice of the conditions, the change in the final result is nothing but due to the systematic error. In the above list, the errors for the first six categories are not independent of each other in the kinematics reconstruction and the unfolding procedure. The systematic errors for these categories are estimated by repeating the unfolding under different conditions. The errors for the last two categories are obtained independently of the other errors since the systematic errors are linearly propagated to the final results.

Q^2 [GeV^2]	x	y	Q^2-range [GeV^2]	x-range	Measured $F_2 \pm$ stat. $\pm$ sys. $\pm$ theo.
8.5	.00023	0.422	7–10	.00015–.0003	$1.290 \pm 0.066 \pm 0.205 \pm 0.018$
8.5	.00045	0.216	7–10	.0003–.0006	$1.046 \pm 0.040 \pm 0.127 \pm 0.003$
8.5	.0009	0.108	7–10	.0006–.0012	$0.807 \pm 0.028 \pm 0.094 \pm 0.000$
8.5	.0016	0.061	7–10	.0012–.002	$0.651 \pm 0.027 \pm 0.059 \pm 0.000$
12	.00023	0.596	10–14	.00015–.0003	$1.461 \pm 0.086 \pm 0.182 \pm 0.038$
12	.00045	0.304	10–14	.0003–.0006	$1.187 \pm 0.048 \pm 0.157 \pm 0.005$
12	.0009	0.152	10–14	.0006–.0012	$0.942 \pm 0.031 \pm 0.118 \pm 0.001$
12	.0016	0.086	10–14	.0012–.002	$0.781 \pm 0.029 \pm 0.094 \pm 0.000$
12	.0028	0.049	10–14	.002–.0036	$0.652 \pm 0.026 \pm 0.055 \pm 0.000$
17	.00045	0.431	14–20	.0003–.0006	$1.327 \pm 0.068 \pm 0.140 \pm 0.010$
17	.0009	0.216	14–20	.0006–.0012	$1.067 \pm 0.041 \pm 0.138 \pm 0.001$
17	.0016	0.121	14–20	.0012–.002	$0.874 \pm 0.033 \pm 0.094 \pm 0.000$
17	.0028	0.069	14–20	.002–.0036	$0.723 \pm 0.028 \pm 0.087 \pm 0.000$
17	.0048	0.040	14–20	.0036–.006	$0.615 \pm 0.029 \pm 0.051 \pm 0.000$
24	.00045	0.609	20–28	.0003–.0006	$1.602 \pm 0.134 \pm 0.201 \pm 0.023$
24	.0009	0.304	20–28	.0006–.0012	$1.247 \pm 0.063 \pm 0.173 \pm 0.003$
24	.0016	0.171	20–28	.0012–.002	$1.001 \pm 0.047 \pm 0.113 \pm 0.001$
24	.0028	0.098	20–28	.002–.0036	$0.837 \pm 0.037 \pm 0.084 \pm 0.000$
24	.0048	0.057	20–28	.0036–.006	$0.680 \pm 0.035 \pm 0.049 \pm 0.000$
34	.00045	0.863	28–40	.0003–.0006	$1.894 \pm 0.225 \pm 0.263 \pm 0.036$
34	.0009	0.431	28–40	.0006–.0012	$1.451 \pm 0.122 \pm 0.152 \pm 0.007$
34	.0016	0.243	28–40	.0012–.002	$1.166 \pm 0.066 \pm 0.098 \pm 0.001$
34	.0028	0.139	28–40	.002–.0036	$0.956 \pm 0.047 \pm 0.080 \pm 0.000$
34	.0048	0.081	28–40	.0036–.006	$0.814 \pm 0.043 \pm 0.074 \pm 0.000$
34	.008	0.049	28–40	.006–.01	$0.689 \pm 0.043 \pm 0.035 \pm 0.000$
48	.0009	0.609	40–56	.0006–.0012	$1.584 \pm 0.171 \pm 0.188 \pm 0.015$
48	.0016	0.343	40–56	.0012–.002	$1.307 \pm 0.090 \pm 0.126 \pm 0.002$
48	.0028	0.196	40–56	.002–.0036	$1.089 \pm 0.065 \pm 0.069 \pm 0.001$
48	.0048	0.114	40–56	.0036–.006	$0.959 \pm 0.060 \pm 0.067 \pm 0.000$
48	.008	0.069	40–56	.006–.01	$0.759 \pm 0.052 \pm 0.050 \pm 0.000$
48	.015	0.037	40–56	.01–.02	$0.597 \pm 0.056 \pm 0.037 \pm 0.000$

Table 9.1: Results of $F_2(x, Q^2)$.

Q^2 [GeV^2]	x	Events in bin	subtracted background	purity	corr. factor	F_L-corr. [%]	F_3-corr. [%]
8.5	.00023	1396	134 ± 94	0.318	2.358	5.97	0.00
8.5	.00045	2665	174 ± 41	0.309	1.499	1.12	0.00
8.5	.0009	1686	46 ± 12	0.330	1.961	0.24	0.00
8.5	.0016	653	0 ± 0	0.303	2.942	0.06	0.00
12	.00023	558	88 ± 13	0.250	3.497	13.11	0.00
12	.00045	2398	165 ± 15	0.331	1.126	2.28	0.00
12	.0009	2571	102 ± 14	0.389	0.960	0.46	0.00
12	.0016	1555	47 ± 20	0.364	1.066	0.12	0.00
12	.0028	842	0 ± 0	0.414	1.903	0.04	0.00
17	.00045	1375	132 ± 17	0.366	1.426	4.88	0.00
17	.0009	2265	119 ± 15	0.417	0.889	0.92	0.00
17	.0016	1577	63 ± 21	0.403	0.863	0.23	0.00
17	.0028	1435	23 ± 16	0.427	0.911	0.07	0.00
17	.0048	380	2 ± 7	0.345	2.642	0.02	0.00
24	.00045	735	97 ± 13	0.322	1.868	11.06	0.00
24	.0009	1469	100 ± 13	0.446	0.984	1.94	0.00
24	.0016	1048	64 ± 19	0.437	0.918	0.45	0.00
24	.0028	1176	18 ± 14	0.466	0.852	0.14	0.00
24	.0048	614	11 ± 9	0.457	1.129	0.04	0.00
34	.00045	337	91 ± 26	0.212	2.336	17.74	0.01
34	.0009	1099	123 ± 87	0.430	1.059	4.31	0.01
34	.0016	831	25 ± 7	0.435	0.926	0.94	0.00
34	.0028	967	18 ± 12	0.520	0.841	0.27	0.00
34	.0048	736	0 ± 0	0.434	0.865	0.08	0.00
34	.008	319	0 ± 0	0.384	1.628	0.03	0.00
48	.0009	642	92 ± 36	0.421	1.184	9.65	0.01
48	.0016	556	12 ± 3	0.460	0.951	1.99	0.01
48	.0028	633	10 ± 6	0.558	0.912	0.55	0.01
48	.0048	593	0 ± 0	0.513	0.832	0.15	0.01
48	.008	420	0 ± 0	0.468	0.879	0.05	0.01
48	.015	115	0 ± 18	0.550	3.699	0.01	0.01

Table 9.2: Statistics of the bins.

108

Q^2 [GeV^2]	x	y	Q^2-range [GeV^2]	x-range	Measured $F_2 \pm$stat.$\pm$sys.$\pm$theo.
68	.0009	0.863	56–80	.0006–.0012	$1.667 \pm 0.275 \pm 0.261 \pm 0.022$
68	.0016	0.485	56–80	.0012–.002	$1.346 \pm 0.128 \pm 0.162 \pm 0.005$
68	.0028	0.277	56–80	.002–.0036	$1.132 \pm 0.085 \pm 0.104 \pm 0.001$
68	.0048	0.162	56–80	.0036–.006	$0.937 \pm 0.071 \pm 0.047 \pm 0.000$
68	.008	0.097	56–80	.006–.01	$0.799 \pm 0.062 \pm 0.086 \pm 0.000$
68	.015	0.052	56–80	.01–.02	$0.606 \pm 0.047 \pm 0.047 \pm 0.000$
120	.0016	0.856	80–160	.0012–.002	$1.668 \pm 0.203 \pm 0.223 \pm 0.016$
120	.0028	0.489	80–160	.002–.0036	$1.250 \pm 0.114 \pm 0.120 \pm 0.004$
120	.0048	0.285	80–160	.0036–.006	$1.046 \pm 0.099 \pm 0.092 \pm 0.001$
120	.008	0.171	80–160	.006–.01	$0.930 \pm 0.070 \pm 0.041 \pm 0.000$
120	.015	0.091	80–160	.01–.02	$0.686 \pm 0.044 \pm 0.055 \pm 0.000$
120	.03	0.046	80–160	.02–.04	$0.568 \pm 0.044 \pm 0.078 \pm 0.000$
240	.0048	0.571	160–320	.0036–.006	$1.162 \pm 0.172 \pm 0.171 \pm 0.004$
240	.008	0.343	160–320	.006–.01	$0.823 \pm 0.091 \pm 0.086 \pm 0.001$
240	.015	0.183	160–320	.01–.02	$0.737 \pm 0.069 \pm 0.060 \pm 0.000$
240	.03	0.091	160–320	.02–.04	$0.593 \pm 0.060 \pm 0.069 \pm 0.000$
240	.06	0.046	160–320	.04–.08	$0.473 \pm 0.051 \pm 0.048 \pm 0.000$
480	.008	0.685	320–640	.006–.01	$0.916 \pm 0.184 \pm 0.193 \pm 0.004$
480	.015	0.365	320–640	.01–.02	$0.705 \pm 0.104 \pm 0.066 \pm 0.001$
480	.03	0.183	320–640	.02–.04	$0.627 \pm 0.090 \pm 0.047 \pm 0.000$
480	.06	0.091	320–640	.04–.08	$0.546 \pm 0.081 \pm 0.097 \pm 0.000$
480	.12	0.046	320–640	.08–.16	$0.363 \pm 0.077 \pm 0.048 \pm 0.000$
960	.015	0.731	640–1280	.01–.02	$0.809 \pm 0.182 \pm 0.531 \pm 0.004$
960	.03	0.365	640–1280	.02–.04	$0.414 \pm 0.096 \pm 0.102 \pm 0.001$
960	.06	0.183	640–1280	.04–.08	$0.411 \pm 0.096 \pm 0.107 \pm 0.000$
960	.12	0.091	640–1280	.08–.16	$0.356 \pm 0.091 \pm 0.058 \pm 0.000$
1920	.06	0.365	1280–2560	.04–.08	$0.436 \pm 0.313 \pm 0.151 \pm 0.001$
1920	.12	0.183	1280–2560	.08–.16	$0.436 \pm 0.233 \pm 0.139 \pm 0.000$
1920	.24	0.091	1280–2560	.16–.32	$0.246 \pm 0.116 \pm 0.065 \pm 0.000$
6280	.12	0.598	2560–10000	.08–.16	$0.509 \pm 0.269 \pm 0.235 \pm 0.002$
6280	.24	0.299	2560–10000	.16–.32	$0.203 \pm 0.113 \pm 0.068 \pm 0.000$

Table 9.1: Results of $F_2(x, Q^2)$ (continued).

109

Q^2 [GeV^2]	x	Events in bin	subtracted background	purity	corr. factor	F_L-corr. [%]	F_3-corr. [%]
68	.0009	186	38 ± 41	0.275	1.549	15.01	0.02
68	.0016	428	54 ± 18	0.458	0.906	4.36	0.02
68	.0028	422	17 ± 6	0.553	0.932	1.14	0.02
68	.0048	367	0 ± 0	0.551	0.865	0.31	0.01
68	.008	360	0 ± 0	0.463	0.788	0.10	0.01
68	.015	284	0 ± 0	0.485	1.064	0.03	0.01
120	.0016	289	28 ± 22	0.438	1.239	11.30	0.04
120	.0028	499	36 ± 18	0.575	0.891	3.65	0.04
120	.0048	437	26 ± 29	0.668	0.966	0.91	0.04
120	.008	456	0 ± 0	0.588	0.803	0.27	0.03
120	.015	522	0 ± 0	0.575	0.843	0.07	0.03
120	.03	247	0 ± 0	0.478	1.615	0.01	0.02
240	.0048	193	25 ± 12	0.603	0.887	4.27	0.15
240	.008	174	5 ± 3	0.664	0.838	1.15	0.13
240	.015	250	0 ± 0	0.694	0.867	0.27	0.11
240	.03	244	0 ± 0	0.517	0.700	0.05	0.09
240	.06	113	2 ± 0	0.533	1.468	0.01	0.07
480	.008	65	8 ± 4	0.665	1.061	5.12	0.50
480	.015	88	0 ± 0	0.779	0.958	1.19	0.44
480	.03	107	2 ± 0	0.684	0.920	0.20	0.35
480	.06	102	0 ± 0	0.577	0.905	0.03	0.26
480	.12	34	3 ± 8	0.484	1.330	0.01	0.18
960	.015	42	2 ± 1	0.860	1.160	4.55	1.52
960	.03	29	0 ± 0	0.755	0.840	0.86	1.35
960	.06	33	0 ± 0	0.681	0.961	0.13	1.01
960	.12	33	0 ± 0	0.452	0.678	0.02	0.71
1920	.06	13	4 ± 7	0.883	1.325	0.56	3.67
1920	.12	14	2 ± 0	0.449	0.770	0.08	2.56
1920	.24	10	2 ± 0	0.460	1.197	0.01	1.63
6280	.12	11	2 ± 0	0.716	0.818	0.51	11.46
6280	.24	4	0 ± 0	0.793	1.245	0.08	8.24

Table 9.2: Statistics of the bins (continued).
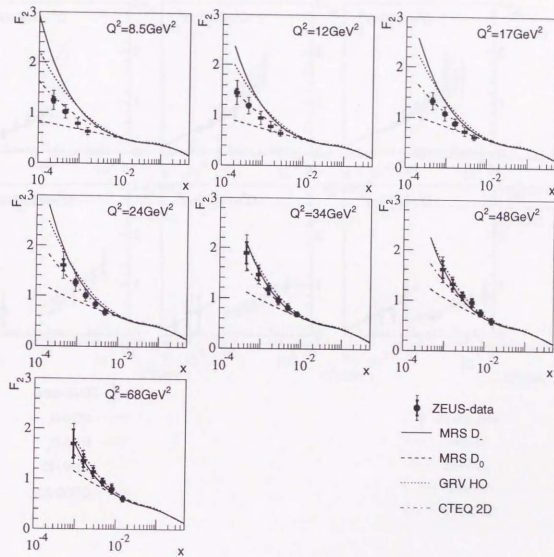
Figure 9.1: Results of $F_2(x, Q^2)$ as functions of x at $Q^2 = 8.5\,\mathrm{GeV}^2$, $12\,\mathrm{GeV}^2$, $17\,\mathrm{GeV}^2$, $24\,\mathrm{GeV}^2$ $Q^2 = 34\,\mathrm{GeV}^2$, $48\,\mathrm{GeV}^2$ and $68\,\mathrm{GeV}^2$.
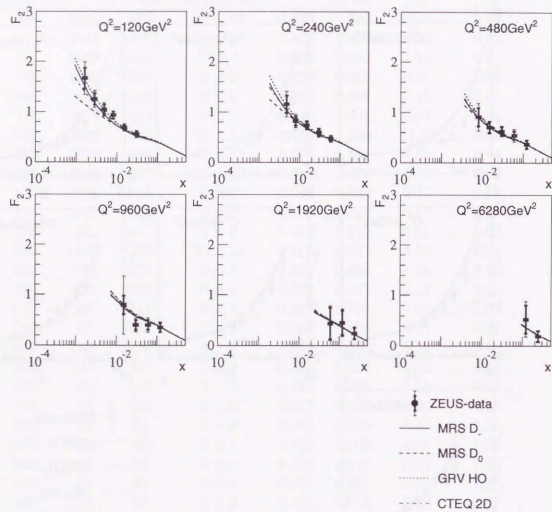
Figure 9.1: Results of $F_2(x, Q^2)$ as functions of x at $Q^2 = 120\,\text{GeV}^2$, $240\,\text{GeV}^2$, $480\,\text{GeV}^2$, $960\,\text{GeV}^2$, $1920\,\text{GeV}^2$ and $6280\,\text{GeV}^2$ (continued).
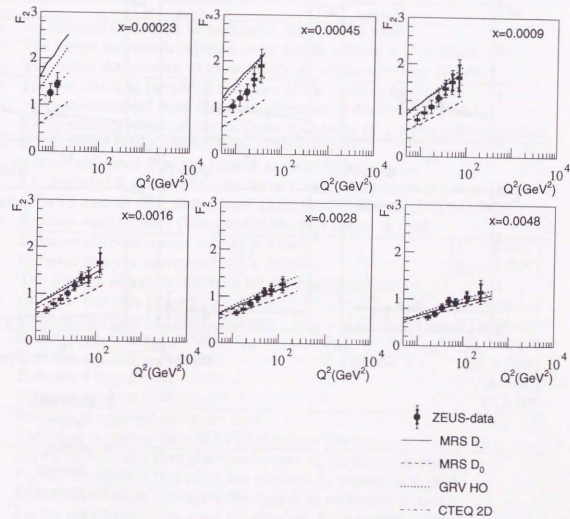

Figure 9.2: Results of $F_2(x, Q^2)$ as functions of Q^2 at $x = 0.00023$, 0.00045, 0.0009, 0.0016, 0.0028 and 0.0048.
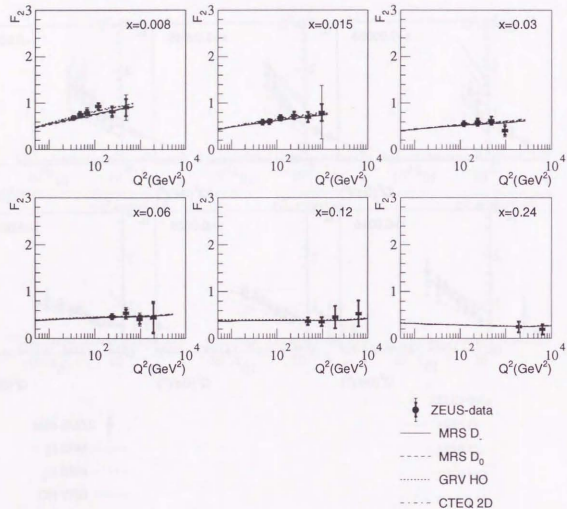
Figure 9.2: Results of $F_2(x, Q^2)$ as functions of Q^2 at $x = 0.008, 0.015, 0.03, 0.06, 0.12$ and 0.24 (continued).

1a	An alternative electron identification algorithm is used.
1b	The vertex position is required to be within $-35\,\mathrm{cm} < Z < 25\,\mathrm{cm}$.
1c	The vertex distribution of Monte Carlo is weighted to that of data.
2a	1 mm is added to the radial direction of the electron position.
2b	1 mm is subtracted from the radial direction of the electron position.
2c	The electron position of Monte Carlo is smeared by a 5 mm-width gaussian.
3a	$0.5°$ is added to the hadron angle of Monte Carlo.
3b	$0.5°$ is subtracted from the hadron angle of Monte Carlo.
3c	5 % degraded δ_{had} is used to reconstruct the hadron angle of Monte Carlo.
3d	ME+PS hadron final state Monte Carlo is used instead of CDM+BGF.
3e	Electron method with the corrected electron energy is used.

4a	Different electron energy cut: $E'_e > 6\,\mathrm{GeV}$	$(E'_e > 5\,\mathrm{GeV})$
4b	Different electron energy cut: $E'_e > 7\,\mathrm{GeV}$	$(E'_e > 5\,\mathrm{GeV})$
4c	The electron energy is corrected for the dead material.	
4d	Different box cut: $|X|$ or $|Y| > 18\,\mathrm{cm}$	$(|X|$ or $|Y| > 16\,\mathrm{cm})$
4e	Different box cut: $|X|$ or $|Y| > 20\,\mathrm{cm}$	$(|X|$ or $|Y| > 16\,\mathrm{cm})$
4f	Different y_{JB} cut: $y_{\mathrm{JB}} > 0.05$	$(y_{\mathrm{JB}} > 0.04)$
4g	Different y_{JB} cut: $y_{\mathrm{JB}} > 0.06$	$(y_{\mathrm{JB}} > 0.04)$
4h	Different δ cut: $\delta > 33$	$(\delta > 32)$
4i	Different δ cut: $\delta > 35$	$(\delta > 32)$

6a	Iteration is repeated one more time.
6b	Unfolding is started from MRS D'_0 structure function.
7a	Parton distribution that gives the largest F_L correction is used.
7b	Parton distribution that gives the smallest F_L correction is used.
7c	Parton distribution that gives the largest F_3 correction is used.
7d	Parton distribution that gives the smallest F_3 correction is used.

Table 9.3: Changed conditions for the systematic error estimation. The original conditions of items 4a to 4i are given in the parenthesis.

The conditions that are changed for the systematic error estimation are summarized in Table 9.3.

Categories from 1 to 4 are relevant to the reliability of the Monte Carlo simulation, with which the acceptance and the resolution effects of the measured data are corrected. The error due to the electron identification (category 1) is evaluated by changing the conditions of items from 1a to 1c in the table. Item 1a is to check the electron identification algorithm. With items 1b and 1c, the effect of the dead material is tested since the amount of the dead material that the electron goes through depends on the vertex position. The error due to the measured electron position (category 2) is evaluated by changing the conditions of items from 2a to 2c. In items 2a and 2b, the electron position of Monte Carlo is artificially shifted by a small amount to test the sensitivity to such a bias. Item 2c is to test the influence of the position resolution. The error due to the measured hadron angle (category 3) is evaluated by changing the conditions from 3a to 3e. In items 3a and 3b, the hadron angle Monte Carlo is also artificially shifted by a small amount to test the sensitivity to such a bias. In item 3c, similar sensitivity is tested by changing $\phi_{\rm had}$. In item 3d, ME+PS hadron final state Monte Carlo is used instead of CDM+BGF, to check the sensitivity of the results to a certain final state simulation. In item 3e, the kinematic variables are reconstructed with the electron method after correcting for the electron energy. This is an independent test of the double angle method, hence of the hadronic angle measurement. The error due to the kinematic acceptance (category 4) is evaluated by changing the conditions of items from 4a to 4i. The electron energy cut affects the bins around the boundary at $y = 1$. The box cut affects the bins of smallest Q^2. The y_{JB} cut affects the bins around the boundary at $y = 0.04$. The δ cut affects the bins near the $y = 1$ boundary, where the background subtraction is the largest.

Categories 5 and 6 are relevant to the method to extract the true number of events from the measured number of events. The error due to the background subtraction (category 5) is estimated by propagating the covariant error matrix of the fitting parameters. When the fitting error is smaller than one third of the subtracted background, one third of the background is taken as the systematic error. This error is already included in the statistical error since it is required in the unfolding procedure. The error due to the unfolding procedure (category 6) is estimated by iterating one more time (6a) and by starting from a completely different Monte Carlo structure function (6b). Stability of the background subtraction and the unfolding procedure is also tested by performing these procedures under various conditions in order to check many items listed above.

Categories 7 and 8 are independent of the other errors, since the corrections and the normalization to the luminosity are relevant to the number of events obtained by the unfolding procedure. The error due to the F_L and F_3 corrections (item 7) are estimated by calculating the corrections with various parton distribution sets, MRS D$_0'$ CTEQ 2D and GRV HO. The largest deviation from the correction by the MRS D$_-'$ parton distribution is taken as the error. The error due to the absolute luminosity (item 8) is estimated to be 4 %, which acts on the overall normalization of the results.

The systematic errors are visualized in Fig. 9.3 to Fig. 9.5. In the figures, the systematic error of each item in each bin is shown as the deviation of open circles from the central line in each box. The values of F_2 are obtained under the altered condition, and the deviation from the final result is normalized by the value of the final result. The height of each box indicates ± 30 % deviation, and the dotted lines indicate ± 10 % deviation. The associated error bar is the normalized statistical error of the result under the altered condition. In Fig. 9.3 the deviation by the items from 1a to 3e are shown from left to right. Similarly in Fig. 9.4 those from 4a to 4i are shown and in Fig. 9.5 those from 6a to 7d are shown.

It is seen in the figures that most of the deviations stay within the 10 % lines. When the bin selection criteria is not satisfied by changing the condition, the error is not obtained.

For each categories from 1 to 4 and 6, the maximum deviation among the items is taken as the systematic error for the category. For each bin, the error ratio of categories from 1 to 4, 6 and 7 are obtained as $\Delta_{\rm elec}^{(i)}$, $\Delta_{\rm epos}^{(i)}$, $\Delta_{\rm had}^{(i)}$, $\Delta_{\rm cut}^{(i)}$, $\Delta_{\rm unf}^{(i)}$ and $\Delta_{\rm theo}^{(i)}$ respectively (i stands for the bin). The luminosity error ratio $\Delta_{\rm lumi}$ is constant. The first five errors and the statistical error $\Delta_{\rm stat}^{(i)}$ are treated as independent each other, and they are added in quadrature. The last two errors are treated as normalization error and added linearly. The total error ratio is given by

$$\Delta_{\rm sys}^{(i)} = \sqrt{(\Delta_{\rm elec}^{(i)})^2 + (\Delta_{\rm epos}^{(i)})^2 + (\Delta_{\rm had}^{(i)})^2 + (\Delta_{\rm cut}^{(i)})^2 + (\Delta_{\rm unf}^{(i)})^2}$$
$$\Delta_{\rm total}^{(i)} = \sqrt{(\Delta_{\rm stat}^{(i)})^2 + (\Delta_{\rm sys}^{(i)})^2} + \Delta_{\rm theo}^{(i)} + \Delta_{\rm lumi}.$$

The total error given in Fig. 9.1 and 9.2 does not include the luminosity error. In Table 9.1, $\Delta_{\rm sys}^{(i)}$ and $\Delta_{\rm theo}^{(i)}$ are given separately. The values of the error components are tabulated in Table 9.4.
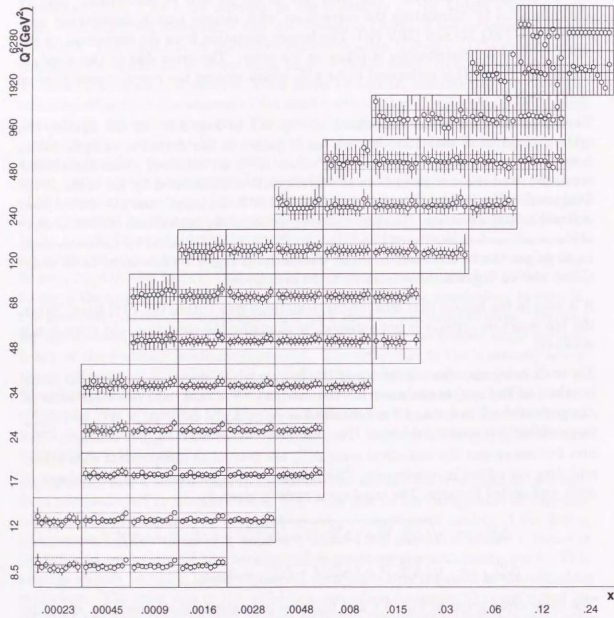
Figure 9.3: Systematic error checks of the Monte Carlo simulation. Variation of the results under conditions of items 1a to 1c, 2a to 2c and 3a to 3e of Table 9.3 are shown from left to right as described in text.
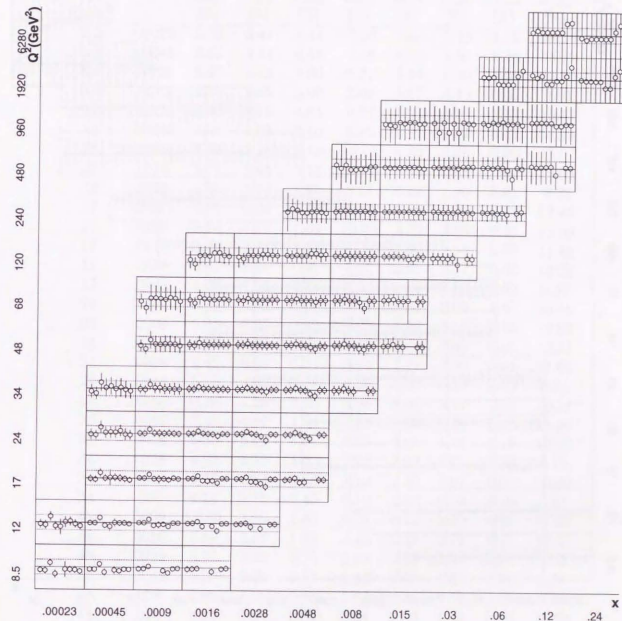
Figure 9.4: Systematic error checks of the kinematic cut stabilities. Variation of the results under conditions of items 4a to 4i of Table 9.3 from left to right as described in text.
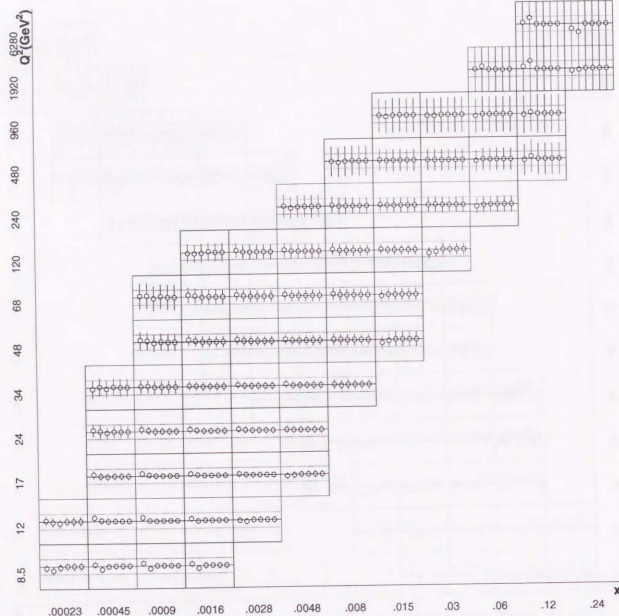
Figure 9.5: Other systematic error checks of the unfolding procedure and the theoretical errors. Variation of the results under conditions of items 6a, 6b and 7a to 7d of Table 9.3 from left to right as described in text.

Q^2 [GeV^2]	x	Δ_{stat} [%]	Δ_{elec} [%]	Δ_{epos} [%]	Δ_{had} [%]	Δ_{cut} [%]	Δ_{unf} [%]	Δ_{theo} [%]	Δ_{total} [%]
8.5	.00023	5.12	3.41	7.21	7.98	9.38	6.05	1.42	18.10
8.5	.00045	3.82	3.44	4.59	6.98	6.60	4.83	0.25	13.02
8.5	.0009	3.47	3.72	2.60	6.57	6.94	5.00	0.05	12.25
8.5	.0016	4.15	4.45	2.00	3.69	5.07	4.40	0.01	9.99
12	.00023	5.89	5.13	4.04	6.57	8.21	1.56	2.57	16.37
12	.00045	4.04	3.03	2.36	9.52	6.91	4.67	0.41	14.24
12	.0009	3.29	3.18	1.49	10.08	4.99	4.36	0.08	13.07
12	.0016	3.71	2.43	1.15	5.76	9.99	2.36	0.02	12.65
12	.0028	3.99	1.53	1.69	4.45	6.44	1.90	0.01	9.28
17	.00045	5.12	3.24	1.66	6.10	7.46	2.19	0.72	12.43
17	.0009	3.84	4.12	1.69	10.22	5.62	3.23	0.13	13.59
17	.0016	3.78	3.78	1.49	8.01	5.49	2.36	0.03	11.46
17	.0028	3.87	3.46	0.97	5.53	9.96	1.12	0.01	12.62
17	.0048	4.72	1.95	0.81	6.67	3.90	2.26	0.00	9.56
24	.00045	8.36	4.62	1.00	7.49	8.61	2.09	1.41	16.48
24	.0009	5.05	3.93	1.76	11.31	6.09	3.05	0.24	15.02
24	.0016	4.70	3.80	1.70	9.39	4.00	2.60	0.05	12.31
24	.0028	4.42	2.99	1.31	5.14	7.77	2.00	0.01	11.01
24	.0048	5.15	1.62	1.18	4.85	5.00	0.59	0.00	8.91
34	.00045	11.88	7.29	1.90	8.08	8.08	2.27	1.91	20.17
34	.0009	8.41	4.62	1.24	7.24	5.72	1.34	0.46	13.89
34	.0016	5.66	3.09	1.37	6.95	3.00	1.36	0.10	10.23
34	.0028	4.92	2.51	1.05	7.22	2.72	1.62	0.03	9.71
34	.0048	5.28	2.33	0.86	3.19	7.86	1.97	0.01	10.50
34	.008	6.24	2.76	1.45	3.19	2.32	0.93	0.00	8.07
48	.0009	10.80	3.09	1.83	9.03	6.12	2.91	0.97	17.00
48	.0016	6.89	2.37	1.22	8.42	2.68	2.71	0.18	12.01
48	.0028	5.97	2.30	0.73	5.14	1.74	2.07	0.05	8.72
48	.0048	6.26	2.29	0.83	4.48	4.59	1.49	0.01	9.42
48	.008	6.85	3.16	0.92	3.69	4.35	0.80	0.00	9.54
48	.015	9.38	1.84	2.35	1.84	2.68	4.45	0.00	11.28

Table 9.4: Error components of the bins in percentage. Δ_{lumi} is not included in Δ_{total}.

Q^2 [GeV^2]	x	Δ_{stat} [%]	Δ_{elec} [%]	Δ_{epos} [%]	Δ_{had} [%]	Δ_{cut} [%]	Δ_{unf} [%]	Δ_{theo} [%]	Δ_{total} [%]
68	.0009	16.50	3.78	2.82	8.94	11.64	2.92	1.34	24.10
68	.0016	9.51	3.12	0.52	10.03	4.90	3.16	0.39	15.72
68	.0028	7.51	6.10	1.68	5.92	2.12	2.29	0.10	11.98
68	.0048	7.58	2.88	1.07	2.99	2.03	1.72	0.02	9.12
68	.008	7.76	2.00	1.25	2.63	10.01	1.51	0.01	13.25
68	.015	7.76	1.16	1.65	6.77	2.48	1.82	0.00	10.93
120	.0016	12.17	2.64	0.42	5.04	11.99	1.48	0.93	19.00
120	.0028	9.12	3.52	0.80	7.36	4.56	2.01	0.30	13.54
120	.0048	9.46	4.11	0.38	6.88	3.15	1.86	0.08	13.02
120	.008	7.53	3.01	1.40	1.94	0.97	1.96	0.03	8.76
120	.015	6.41	2.48	0.87	6.71	3.35	1.18	0.00	10.28
120	.03	7.75	4.05	3.17	4.93	10.21	5.62	0.00	15.70
240	.0048	14.80	10.76	2.58	9.04	3.01	1.70	0.34	21.20
240	.008	11.06	2.92	0.97	9.96	0.61	0.88	0.10	15.34
240	.015	9.36	2.04	0.68	7.73	0.68	0.99	0.04	12.43
240	.03	10.12	1.52	1.18	11.47	1.18	0.70	0.01	15.48
240	.06	10.78	4.65	1.69	8.25	2.11	2.62	0.01	14.84
480	.008	20.09	4.80	4.37	19.54	4.15	1.91	0.42	29.55
480	.015	14.75	3.69	0.28	8.37	1.84	0.71	0.14	17.61
480	.03	14.35	4.94	0.96	5.42	0.96	0.00	0.06	16.24
480	.06	14.84	2.75	1.28	8.42	15.20	1.69	0.02	23.13
480	.12	21.21	4.13	1.65	7.44	9.09	3.84	0.01	24.96
960	.015	22.50	21.51	3.09	61.68	4.94	1.86	0.51	69.87
960	.03	23.19	5.31	14.01	14.25	13.53	1.41	0.23	34.15
960	.06	23.36	3.89	3.89	25.30	2.43	2.20	0.09	35.12
960	.12	25.56	3.65	2.81	14.33	5.90	2.26	0.02	30.35
1920	.06	71.79	13.76	3.90	29.13	11.24	4.15	0.32	80.01
1920	.12	53.44	14.68	1.61	19.72	16.97	11.32	0.08	62.36
1920	.24	47.15	8.54	6.10	20.73	12.20	3.28	0.03	54.09
6280	.12	52.85	23.38	11.39	33.40	15.91	9.10	0.33	70.48
6280	.24	55.67	12.81	4.93	23.65	13.79	13.26	0.15	65.05

Table 9.4: Error components of the bins in percentage (continued).

Chapter 10

Discussion

The obtained results of the proton structure function F_2 are updating the previously published results of ZEUS[1] and H1[2]. The higher statistics than used in the previous results make it possible to reduce the errors, to extend the kinematic range and to adopt finer bin sizes. With the new results, the x- and Q^2-dependence of F_2 is studied in detail. The previous results are confirmed to agree with the new results.

The new results are also compatible with the results of the fixed target experiments prior to HERA. The results are compared with the theoretical predictions, that agree each other at large x. Because these predictions are tuned to agree with the fixed target results at large x, to compare with the predictions is equivalent to compare with the extrapolation of the fixed target results.

On the other hand, at small x there has been no standard way to extrapolate the proton structure function from the fixed target region. As mentioned in Section 2.4, this is because there are large ambiguities in the models of the gluon density, namely how or whether the gluon density increases at small x. Therefore, it is the best way to compare the x-dependence of the results with those of the predictions that are introduced in Section 2.4.

In Fig. 9.1 shown in the curves are the theoretically predicted F_2 from the parton distributions of MRS D'_(solid line), MRS D$_0'$(dashed line), CTEQ 2D(dot-dashed line) and GRV HO(dotted line). Here, the results are not parametrized directly to any function, but general interpretation can be obtained by comparing with these curves. At small x the parton density is dominated by that of gluon due to the $1/x$ factor in the split functions for gluon production. Although the rise of gluon

density does not directly appear in F_2, these gluons generate more sea quarks that contribute to the rise of F_2. This means by comparing the rise of F_2 one can get an indirect information of the rise of the gluon density. The predictions are classified by how fast it assumes the gluon density increases, in the form of $xg(x) \propto x^{-\lambda}$, where λ gives the speed of increase and it ranges from 0 of MRS D_0', ~ 0.3 of CTEQ, ~ 0.4 of GRV to 0.5 of MRS D_-' at a fixed $Q^2 \sim 4\,\mathrm{GeV}^2$. Among the curves of the predictions, the closest one to the data points is that of CTEQ. The main reason of the agreement is because this parton distribution includes the previous HERA results in the global fitting of the parton distribution. Especially at $Q^2 = 8.5\,\mathrm{GeV}^2$, $12\,\mathrm{GeV}^2$ and $17\,\mathrm{GeV}^2$, neither the steeply rising curves of MRS D_-' and GRV nor the gently rising curve of MRS D_0' agrees with the data points. However, CTEQ 2D is not the best parton distribution at $Q^2 = 34\,\mathrm{GeV}^2$, $48\,\mathrm{GeV}^2$ and $68\,\mathrm{GeV}^2$. The data points rises as steeply as the curve of MRS D_-' or GRV. The results of F_2 are characterized by the increase at small x, and the gentle slope of the MRS D_0' curve cannot explain data at small x. The rise of gluon density, as seen through the rise of F_2 at small x, follows the parametrization with λ between 0.3 and 0.5. The results then give an interest to the things like, what is the precise value of the exponent or whether it is valid to express the increase in the exponent of x. In any case, the gluon density has to stop increasing at some small x, before the number of gluon times the parton size $(1/Q^2)$ exceeds the geometrical cross section of the proton.

Above $Q^2 = 240\,\mathrm{GeV}^2$, all curves agree with the data points, and hence the parton distribution cannot be discriminated by the data points. The first measurement of F_2 at very high Q^2 above $1000\,\mathrm{GeV}^2$ shows no deviation from the predictions of the Standard Model within the large errors due to the limited statistics.

The Q^2-dependence of the F_2 results is similarly compared with the predictions in Fig. 9.2. The Q^2-dependence is modeled by the standard GLAP evolution of the parton density in all the predictions, and hence the main reason of the difference between predictions is the starting point of the evolution. The discrepancy between curves is largest at $x = 0.00023$, then the discrepancy becomes small as x becomes large and the discrepancy becomes almost insignificant above $x = 0.0048$. The consequence of the observed x-dependence is also seen in the Q^2-dependence plots. The data points lie on the CTEQ curve at small Q^2 and on the MRS D_-'/GRV curves at moderate Q^2 above $30\,\mathrm{GeV}^2$. Therefore, the Q^2-dependence at small x does not agree with any of the predictions. The results of F_2 show steeper evolution than predicted.

Then, what is the reason of the steeper evolution? For example, there is an idea that F_2 is suppressed at small-x by the gluon recombination[60,61]. If the gluon density increases at small-x, then at some point the gluons start to recombine in order to suppress the increase. This effect is observed from the exchanged boson as the screening of the gluons. Even if the gluons are still free at small-x and large-Q^2, it may not be the same at small-Q^2. The exchanged boson can resolve large number of partons at large-Q^2 but at small-Q^2 some fraction of them are hidden behind other partons. Since the parton density only increases with $\log Q^2$ while the spatial resolution of the exchanged boson decreases with $1/\sqrt{Q^2}$, the qualitative behavior does not disagree with this view. For the other explanation, the region looking at is around 10 to $100\,\mathrm{GeV}^2$ in Q^2, where the charm density starts to contribute to the structure function. The charm mass cannot be straightforwardly related to some Q^2 value, but the value of Q^2 can be an indication of the threshold value of the charm production. The required energy for the charm pair production is about $3\,\mathrm{GeV}$, and hence $Q^2 \gtrsim 10\,\mathrm{GeV}^2$ is at least required. The dominant charm production process at small-x is the boson gluon fusion; the intrinsic charm inside the proton is only available at large-x.

Since the gluon density is rising at small x, it is unavoidable that at some small x value the partons start recombination. Whether the effect can be seen at HERA or not, is an especially interesting topic for any of the QCD applications, because if so, one can set a boundary between the region where the (next-to-)leading log approximation is safe and the region where the recombination effect has to be taken into account. Such effect can be seen as the deviation from the standard Q^2 evolution, although it would be difficult to quantitatively demonstrate the effect. Furthermore, F_2 is not the exclusive source that can be used for the description of the proton structure. The gluon density can be extracted from several different processes, for example from jet rate, J/ψ production or F_L measurement in addition to that from the shape of F_2. It is also important for the detailed study of the Q^2 evolution to extract the charm structure function independently by measuring the charmed meson in the final state. The study of the proton structure in the new region just has started toward a new description of the proton.

Chapter 11

Conclusion

New measurement of the proton structure function F_2 is presented in this thesis. The results of F_2 are obtained from $543 \, \mathrm{nb}^{-1}$ of data collected with the ZEUS detector at HERA during the 1993 run period. The measurement extends over a wide kinematic region from $8.5 \, \mathrm{GeV}^2$ to $6280 \, \mathrm{GeV}^2$ in Q^2 and from 2.3×10^{-4} to 0.24 in x. The results consistently improves the previous F_2 results of HERA[1, 2] with the smaller errors, the finer binning and the extension of the kinematic range.

The NC-DIS event selection is performed mainly with the calorimeter. After the electron identification, kinematic selection and background rejection, 45062 events are collected in the NC-DIS event sample. Kinematic variables x and Q^2 are obtained from the electron angle and the hadron angle with the double angle method. Events are divided into 12 bins in x and 13 bins in Q^2. Among the bins, 62 bins are selected according to the resolution of the kinematic variable reconstruction and the statistics of data. The F_2 results are extracted from the number of events in the bins by an unfolding procedure, which corrects for the detector resolution, the kinematic acceptance and the radiative events.

The obtained results are tabulated in Table 9.1 and are visualized in Fig. 9.1, 9.2. In the small x region, F_2 increases steeply along with the decrease of x. The results are compared with several available predictions that are based on different assumptions of the gluon density at small x. None of them succeeds to completely explain data, mainly due to the discrepancy in the Q^2 evolution at small x. The data shows faster evolution than predicted in the range of $10 \, \mathrm{GeV}^2$ to $100 \, \mathrm{GeV}^2$ especially when x is less than 0.003. The rise of F_2 at small x is interpreted as the increase of the gluon density, and the comparison with the predictions shows the gluon density is parametrized by $xg(x) \sim x^{-\lambda}$ with a value of λ between 0.3 and 0.5.

References

[1] ZEUS Collaboration: M. Derrick et al., Phys. Lett. B316 (1993) 412.

[2] H1 Collaboration: I. Abt et al., Nucl. Phys. B407 (1993) 515.

[3] R. P. Feynman, *Photon-Hadron Interactions*, (1972) Benjamin.

[4] F. Halzen and A. D. Martin, *Quarks and Leptons: A Introductory Course in Modern Particle Physics*, (1984) John Wiley & Sons.

[5] R. G. Roberts, *The structure of the proton*, (1990) Cambridge University Press.

[6] E. D. Bloom et al., Phys. Rev. Lett. 23 (1969) 930.
    M. Breidenbach et al., Phys. Rev. Lett. 23 (1969) 935.

[7] R. P. Feynman, Phys. Rev. Lett. 23 (1969) 1415.

[8] D. J. Fox et al., Phys. Rev. Lett. 33 (1974) 1504.
    Y. Watanabe et al., Phys. Rev. Lett. 35 (1975) 898.
    C. Chang et al., Phys. Rev. Lett. 35 (1975) 901.

[9] BCDMS collaboration: A. C. Benvenuti et al., Phys. Lett. B223 (1989) 485.
    BCDMS collaboration: A. C. Benvenuti et al., Phys. Lett. B223 (1989) 490.

[10] The European Muon Collaboration: J. J. Aubert et al., Nucl. Phys. B259 (1985) 189.

[11] New Muon collaboration: P. Amaudruz et al., Phys. Lett. B295 (1992) 159.

[12] G. Ingelman et al., Proc. of the HERA workshop vol. 1 (1988) 3.

[13] C. G. Callan and D. J. Gross, Phys. Rev. Lett. 22 (1969) 156.

[14] J. Sánchez Guillén et al., Nucl. Phys. B353 (1991) 337.

[15] L. W. Whitlow et al., Phys. Lett. B250 (1991) 193.

[16] V. N. Gribov and L. N. Lipatov, Sov. Journ. Nucl. Phys. 15, (1972) 438 and 675.
G. Altarelli and G. Parisi, Nucl. Phys. 126 (1977) 297.

[17] Proc. of the HERA workshop, Hamburg, October 12–14, 1987, vol. 1, 2, ed. by R. D. Peccei, DESY (1988) 231.

[18] Proc. of Workshop on Physics at HERA, Hamburg, October 29–30, 1991, vol 1, 2, 3., ed. by W. Buchmüler and G. Ingelman, DESY, (1992), 1294.

[19] G. Wolf, *First Results from HERA*, DESY 92-190 (1992).

[20] HERA, A Proposal for a large Electron-Proton Colliding Beam Facility at DESY, DESY HERA 81/10.
G. Wolf, HERA: Physics, machine and experiments, DESY 86/89.

[21] ZEUS, a Detector for HERA, Letter of Intent, DESY (1985).
The ZEUS Detector, Technical Proposal, DESY (1986).
The ZEUS Detector, Status Report 1987, DESY (1987).
The ZEUS Detector, Status Report 1989, DESY (1989).

[22] US-ZEUS collaboration: J. Repond et al., *Design and construction of the ZEUS Barrel calorimeter*, ANL-HEP-CP-90-123 (1990).
ZEUS calorimeter group: A. Andresen et al., Nucl. Instr. and Meth. A309 (1991) 101.
ZEUS barrel calorimeter group: A. Bernstein et al., Nucl. Instr. and Meth. A336 (1993) 23.

[23] ZEUS-UK collaboration: C. B. Brooks et al., Nucl. Instr. and Meth. A283 (1989) 477.

[24] D. Bandyopadhyay, *MUTRIG: A Third Level Trigger Muon Finder*, ZEUS-Note 93-013.

[25] F. Jacquet and A. Blondel, Proceedings of the study of an *ep* facility for Europe, DESY 79/48 (1979) 391, U. Amaldi ed.

[26] A. D. Martin, R. G. Roberts and W. J. Stirling, Phys. Lett. B306 (1993) 145.

[27] CTEQ Collaboration: J. Botts et al., Phys. Lett. B304 (1993) 159.

[28] M. Glück, E. Reya and A. Vogt, Phys. Lett. B306 (1993) 391.

[29] ZEUS Collaboration: M. Derrick et al., Phys. Lett. B303 (1993) 183.

[30] M. Zachara, private communication.

[31] W. Smith et al, *The ZEUS trigger system*, ZEUS-Note 89-084 (1989).

[32] H. Boterenbrood et al, *The ZEUS First and Second Level Trigger*, NIKHEF-H-01-1993B (1993) 3.

[33] M. Nakao, *Development of Online Software for ZEUS Global First Level Trigger*, Master thesis, Tokyo University (1991).

[34] H. Uijterwaal, *The Global Second Level Trigger for ZEUS*, PhD thesis, Universiteit van Amsterdam (1992).

[35] H. van der Lugt, *The Data-Acquisition and Second Level Trigger System for the ZEUS Calorimeter*, PhD thesis, Universiteit van Amsterdam (1993).

[36] HERACLES 4.1: A. Kwiatkowski, H. Spiesberger and H.-J. Möhring, Proc. of Workshop on Physics at HERA vol 3., DESY (1992), 1294.

[37] ARIADNE 3.1: L. Lönnblad, Comput Phys. Commun. 71 (1992) 15.

[38] ZEUS Collaboration: M. Derrick et al., Z. Phys. C59 (1993) 231.
H1 Collaboration: I. Abt et al., Phys. Lett. B298 (1993) 469.
H1 Collaboration: I. Abt et al., *Energy Flow and Charged Particle Spectra in Deep Inelastic Scattering at HERA*, DESY 94-033 (1994).

[39] LEPTO 6.1: G. Ingelman, Proc. of Workshop on Physics at HERA vol 3., DESY (1992), 1366.

[40] PYTHIA 5.6/JETSET 7.3: T. Sjöstrand, CERN-TH. 6488/92 (1992)

[41] GEANT 3.13: R. Brun et al., CERN DD/EE/84-1 (1987).

[42] MOZART: Zeus detector simulation program.

[43] ZGANA: R. Woudenberg (Editor) et al. (1993)

[44] Y. Yamazaki, *ZEUS shodan trigger no offline kaiseki* (*Offline analysis of the ZEUS first level Trigger*, in Japanese), Master thesis, Tokyo University (1993).

[45] TLTZGANA: Trigger simulation program for ZEUS TLT.

[46] EEXOTIC: A. Caldwell, an electron finding routine included in the ZEUS PHANTOM library.

[47] ELEC5: J. Repond, an electron finding routine included in the ZEUS PHANTOM library.

[48] ELECPO-M: T. Doeker, A. Frey, M. Nakao, an electron position reconstruction routine included in the ZEUS PHANTOM library.

[49] VCTRAK: D. Bandyopadhyay et al, ZEUS-Note 93-122.

[50] CALTVTX: I. Gialas, a calorimeter vertex reconstruction routine included in the ZEUS PHANTOM library.

[51] P. Kaziewicz and M. Lancaster, *The Tracking Vertex Distribution of the ZEUS 1993 Data*, ZEUS-Note 93-127.

[52] A. Caldwell et al., *An Electron Energy Correction Method: A Preliminary Implementation and Its Effect on the F2 Measurement*, ZEUS-Note 94-051.

[53] A. M. Cooper-Sarkar et al, RAL-87-112 (1987), Proc. of the HERA workshop vol. 1 (1987) 231.

[54] J. Sánchez Guillén et al, Nucl. Phys. B353 (1991) 337.

[55] MINUIT: Reference manual, Cern Program Library Long Writeup D506 (1992).

[56] J. Bartels and J. Feltesse, Proc. of Workshop on Physics at HERA vol 1., DESY, (1992), 131.

[57] A. D. Martin, R. G. Roberts and W. J. Stirling, Phys. Rev. D47 (1993) 46.

[58] V. Blobel, Proceedings of the 1984 School of Computing, CERN 85-09 (1985) 88.

[59] G. D'Agostini, *A Multidimension Unfolding Method Based on the Bayes Theorem*, ZEUS-Note 93-127.

[60] L. V. Gribov, E. M. Levin and M. G. Ryskin, Phys. Rep. 100 (1983) 1.

[61] J. Kwiecinski, A. D. Martin, R. G. Roberts and W. J. Stirling, Phys. Rev. D42 (1990) 3645.

Acknowledgements

Group.

And, ZEUS experiment has been and is carried out by more than 400 physicists from 12 countries, whose names only fit into several pages of papers. I'd like to thank all the members participating the ZEUS collaboration.

Last but not least, I'd like thank my parents who have grown me, and eventually let me work in the high energy physics field, with a lot of patient support physically and mentally.